UNIVERSITY OF CALIFORNIA,

IRVINE

Shrink-Induced Wrinkled Structures for Enhanced Fluorescence Sensing

DISSERTATION

submitted in partial satisfaction of the requirements
for the degree of

DOCTOR OF PHILOSOPHY

in Chemical and Biochemical Engineering

by

Himanshu Sharma

Dissertation Committee:

Associate Professor Michelle Khine, Chair

Professor Enrico Gratton

Professor Vasan Venugopalan

2014

DEDICATION

To my mom and dad,

Aparna & Ramesh Sharma

TABLE OF CONTENTS

LIST OF FIGURES Page

LIST OF TABLES

ACKNOWLEDGMENTS

I am deeply grateful to my advisor, Dr. Michelle Khine, for her guidance and mentorship over the past four years through every step of the rigors of my research. She has been one of the most approachable advisors that any graduate student could have and despite all the things she has been involved in, she has always dedicated time for her students. I am indeed indebted to her for being a constant source of inspiration, challenging me, giving me the freedom to do my own experiments, and constantly pushing me to become a better scientist. Without her never-ending support, patience, encouragement, enthusiasm, and passion for science, this work would not have been possible.

Thanks also to my defense committee members, Dr. Enrico Gratton and Dr. Vasan Venugopalan for their remarkable foresight with my project and for fruitful discussions. I am grateful to Dr. Gratton for his expertise, support, and thoughtful suggestions to move this research forward. Thanks to my other qualifying exam committee members, Drs. Ali Mohraz and Bill Cooper who provided insightful suggestions during my advancement exam.

I have been very fortunate to work with an amazing team during my Ph.D. I would like to thank all my collaborators, Drs. Michelle Digman, Regina Ragan and Robert Corn, Nick Sharac, Jennifer Wood, and Nico Seefeld. Thank you Dr. Digman for training me on the confocal microscope and teaching me all the important things I needed to know for my project. I am grateful to Nick Sharac and Jennifer Wood for their help with the nanosphere lithography and DNA project, respectively. Thanks to the current and former Khine lab members, Dr. Dharmakeerthi Nawarthana, Dr. Aaron Chen, Sophia Lin, Jolie McClane, Jonathan Pegan, Eugene Lee, Nicole Mendoza, Roger Tu, David Dyer, Valerie Lew, Diep Nguyen, Shreshta

Jayadev, and the rest for their support and fostering a fun lab environment. Thanks also to the current and former members of the Gratton lab for their support and encouragement. To the former undergraduate students, Natasha Felsigner, Avina Gupta, Bakr Teebi, Sam Manoucheri, and Pratika Sah, who all took a chance to work with me and were patient while we worked on these research projects, I greatly appreciate it. Thanks to the ChEMS and BME staff for always being so helpful with equipment training, purchase orders, payroll forms, and always leaving extra food for me in the kitchen.

I would like to also thank my former mentors, Drs. Andrew Putnam, Gerald Fuller, Oscar Abilez, Ramana Pidaparti, Jayakumar Rajadas, Nancy Da Silva, Szu-Wen Wang, Cyrus Ghajar, and Gary Koenig, who inspired me to continue on to pursue my Ph.D.

I would like to extend my gratitude to the amazing friends that I have made during my time at UCI and especially thank them for making my time at UCI enjoyable. Above all, my loving parents who have given me everything I needed to pursue my goals, understanding and supporting my decisions, and constantly loving me every day.

This work was supported by the National Institute of Health (NIH) through the DP2 NIH Director's New Innovator Award (1 DP2 OD007283-01).

Curriculum Vitae

Himanshu Sharma

Education

Doctor of Philosophy- Chemical and Biochemical Engineering **2014**

University of California, Irvine

Masters of Science- Chemical and Biochemical Engineering **2008**

University of California, Irvine

Bachelors of Science-Chemical & Biological Engineering **2007**

University of Wisconsin, Madison

Journal Publications

1. Sharma, H et. al. *Shrink-Induced Silica Multi-Scale Structures for Enhanced Fluorescence from DNA Microarrays*, under review by Langmuir.
2. Sharma, H et. al, *Enhanced Emisson of Fluorophores on Shrink-Induced Wrinkled Composite Structures*, Optical Materials Express, 4, March 20, 2014.
3. With Lin et. al, *Shrink-Induced Silica Structures for Far-field Fluorescence Enhancements,* Advanced Optical Materials, 103, June 21, 2013.
4. With Nawarathna et. al, *Shrink-Induced Microfluidic Sorting using Integrated Magnetic Traps*, Applied Physics Letters, 102, Feb 13, 2013.
5. With Freschauf et. al., *Shrink-Induced Super hydrophobic and Antibacterial Surfaces in Consumer Plastics*, PLOS One, August 20, 2012.
6. With Chen et. al., *Shrink-Film Configurable Multi-scale Wrinkles for Functional Alignment of Human Embryonic Stem Cells and their Cardiac Derivatives*, Advanced Materials, Nov 8, 2011.
7. Sharma, H et. al., *Tunable Plasmonic Nanostructures for Enhanced Sensing*, Technologies for Future Micro-Nano Manufacturing Conference, Napa, CA, Aug 8, 2011.
8. With Chen et. al., *Think Big Then Shrink: Low Cost, Ultra-rapid Tunable Nanowrinkles from Shape Memory Polymers*, Bionanotechnology: Global Prospects II, 2011.
9. Sharma, H et. al., *Unconventional Low-Cost Fabrication and Patterning Techniques for Point of Care Diagnostics,* Annals of Biomedical Engineering, Nov 16, 2010.
10. With Huang et. al., *A matrix micropatterning platform for cell localization and stem cell fate determination*, Acta Biomaterialia, July 1, 2010.
11. With Pidaparti et. al., *Degradation Experiments and Analysis of Corrosion Damage*, International Journal of Damage Mechanics, February 16, 2009.

Conference Abstracts

1. Sharma, H. Shrink-Induced Wrinkled Composite Structures for Enhanced Fluorescence Sensing. Presented at AGS Symposium. Irvine, CA. April 2014
2. Sharac, N. and Sharma, H. et. al., Tunable Nanobead Arrays for Controlling Propagation of Light. Presented at SPIE conference. San Diego, CA., July 2013.
3. Sharma, H. et al., Gold *Nanostructures for Enhanced Fluorescence Detection. Presented at Biomedical Engineering Society*. Atlanta, GA., October 2012.
4. Sharma, H. et al., *Fluorescence Enhancement with Gold Nanostructures Generated on a Thermoplastic*. Presented at UC Bioengineering Symposium. Berkeley, CA., June 2012.
5. Sharma, H. et al., *Fabrication of Tunable Gold Plasmonic Nanostructures for Enhanced Sensing*. Presented at Technologies for Future Micro-Nano Manufacturing. Napa Valley, CA., August 2011.
6. Sharma, H. et al., *Fabrication of Tunable Gold Plasmonic Nanostructures for Enhanced Sensing*. Presented at Micro/Nanofluidics Conference. Irvine, CA., March 2010.

ABSTRACT OF THE DISSERTATION

Shrink-Induced Wrinkled Structures

For Enhanced Fluorescence Sensing

By

Himanshu Sharma

Doctor of Philosophy in Chemical and Biochemical Engineering

University of California, Irvine, 2014

Professor Michelle Khine, Chair

One of the greatest challenges in global health is to develop inexpensive technologies that are highly sensitive, rapid in readout, and selective for particular agents. Fluorescence is widely used in diagnostics due to its sensitivity and specificity, but an ongoing challenge is to detect and quantify low concentration of target biomolecules and specifically by amplifying the fluorescence signal. Efforts to enhance the fluorescence signal relative to the background have been employed using nanoscale metallic structures and reflective surfaces. These studies have shown that by manipulating the interaction of light with these types of structures, enhancements in the fluorescence signal can be achieved.

Motivated by the need for earlier, better detection of infectious diseases, in this dissertation, commodity shrink wrap film is used as a platform and combined with top-down and bottom-up approaches for two underlying intentions: to create scalable methods for synthesis of tunable structures, and to provide an inexpensive, sensitive fluorescence biosensor. We present a simple approach to pattern metal films onto the shrink wrap film and leverage the stiffness mismatch during the shrinkage to create nano to microscale metallic structures. The use of these

metallic structures is demonstrated by depositing fluorescently labeled molecules on top and studying the characteristic properties of the fluorophore's interaction (intensity, emission spectra, and lifetime) with the structures. We demonstrate that our metallic structures can enhance the fluorescence signal relative to a planar surface by more than 1000 fold and show that the fluorescence lifetime is shortened to the point of the detection limit of the system. We also present methods to self-assemble colloidal particles onto the shrink wrap film and etch the particles to various sizes and leverage the shrinkage of the shrink wrap to control the gaps between the etched particles. Finally, we present a manufacturable and scalable method for fabrication of multi-scale wrinkled silica (SiO_2) structures on shrink-wrap film for far-field fluorescence signal enhancements in DNA fluorescence microarrays. Our SiO_2 structured substrate has an improved detection sensitivity (280 pM) relative to planar glass slide (11 nM) and an improvement of 30-45 times in the signal to noise ratio (SNR). The techniques presented in this dissertation to make these low-cost structures are simple but yield significant enhancements in the fluorescence signal. Development of such tools open up the potential to bring a rapid, portable, sensitive, diagnostic device that could potentially aid in detection of diseases at an earlier stage of infection.

Chapter 1 Introduction

1.1 Motivation

Infectious diseases such as diarrheal disease, malaria, and HIV/AIDS remain the second leading cause of global deaths after cardiovascular diseases [1, 2]. Each year, approximately 16 percent of the deaths that occur in the world are related to infectious diseases[3]. A report by the Child Health Epidemiology Reference Group (CHERG) organization indicates that more than two-thirds of the nine million children deaths that occurred each year were related to infectious diseases[4]. Another report by the World Health Organization (WHO) in 2011 estimated that four of the ten leading causes of death were related to infectious diseases [5]. However, in some poor countries where the health care infrastructure is weak, five of the ten leading causes of death were related to infectious agents. An estimated 95 % of such deaths were due to lack of adequate treatment or improper diagnosis due to the difficulties in accessing proper health care infrastructure[6]. One of the shocking truths is that most infectious diseases are treatable and can be prevented from rampantly spreading if detected early in their progression. However, in developing countries, proper medical clinics are scarce and people may have to travel hundreds of miles and then wait in queues to get tested. Further, in some of these clinics, only one person may be available to provide a proper diagnosis. Thus, one of the key barriers to improving the management and surveillance of infectious diseases is the lack of rapid and effective diagnosis to direct treatment decisions at the patient's bedside or at the point of care (POC). The WHO has established guidelines to develop diagnostic tools that fit the ASSURED (affordable, sensitive, specific, user-friendly, rapid, and robust, equipment-free, and deliverable to end users) criteria[7].

An ideal POC technology has the potential to monitor infectious diseases in resource-limited settings and provide a way to rapidly detect and prevent the spread of the disease. The tests can be administered at the patient's bedside or even by the patient himself/herself, offering not only convenience but a significantly faster diagnosis than conventional lab-based testing. Reducing the diagnosis time from days to minutes enables better patient management decisions that may lead to improved prognosis, short wait lines in medical clinics, and reduced overall health care cost. In particular, the potential of rapid, quantitative, and sensitive diagnosis has resulted in many innovative lab on chip (LOC) technologies for POC applications. Perhaps the most compelling application of such technologies is in the early and accurate detection of infectious agents in developing countries[8]. In such cases the technologies must be inexpensive, robust, scalable, simple to use, easily adaptable to detecting various infectious agents while, sturdy under harsh and resource limited environments [9]. Likewise, accurate diagnosis of the disease at an early stage of infection, these assays must be quantitative and sensitive [10, 11].

Over the past three decades, there has been significant interest in the development of biosensors suitable for POC diagnostics [12]. A biosensor is an analytical device that consists of a biological receptor and a transducer to provide quantitative or semi-quantitative analytical information[13]. The receptor is a biological recognition element that has the ability to directly interact with an analyte, whereas the signal transducer converts such interactions into a measurable signal by detecting a change in the electrochemical, optical, or physiochemical properties [14-16]. A biosensor that primarily looks at the interactions of antibodies to antigen by immunoassays is known as an immunosensor. Immunoassays are the preferable method for detection of various analytes such as proteins associated with the disease located in bodily fluids

such as blood, urine, and saliva[17]. An immunoassay looks at the interaction of antigens, which are large protein molecules found on the surfaces of viruses and infected cells, to antibodies which are produced as an immune response to the antigen. Most antibodies have a strong specificity and high binding constant to antigens [18].

Optical detection and imaging strategies that rely on using absorbance, fluorescence, chemiluminescence, and surface plasmon resonance have been utilized for development of immunoassays for POC [19-24]. For most blood protein analysis, the current gold standard for detection is based on the enzyme linked immunosorbent assay (ELISA). In traditional ELISA methods, colorimetric, electrochemical or fluorescent readout signals have been utilized to look at the visual binding of protein to specific recognition molecule [25-29]. A colorimetric assay looks at how much light is absorbed by a reagent and typically uses a chromogenic substrate to visualize the amount of reagent present in the sample. Some colorimetric techniques utilize the optical properties of gold (Au) nanoparticles that are coated with capture antibodies to visualize the presence of analyte in samples. As the antigen binds to the coated Au nanoparticle, the Au nanoparticle complex binds to a detection antibody and the Au nanoparticles aggregate as they bind to each other. If the binding of the antigen to the Au nanoparticle coated antibody does not occur, the color of the solution remains red. If binding does occur, then the color of the solution turns to blue. The sensitivity of colorimetric assays is low requiring an abundant amount of proteins in order for the assay to be effective[30]. Electrochemical biosensors couple a biological recognition element to an electrode transducer which converts the biological recognition element into a measurable electrical signal [31]. For these type of biosensors, it is important that the enzymatic product is electroactive so that it is easy to measure through voltammetric or amperometric techniques. Electrochemical biosensors have played an important role in

simplifying the testing for home devices such as self-testing glucose strips, and screen-printed enzyme electrodes. Relative to other techniques, optical techniques have the advantage of high sensitivity, quantitative output, multiplex capabilities, and compatibility with bench-top assays. An attractive advantage of using a fluorescence probe is that when light is shined on the fluorescence intensity is bright and the fluorescence signal is dependent on the number of biomarkers present. Although the sensitivity of a fluorescent based assay is higher than a colorimetric assay, the fluorescence intensity is still low due to the low amount of biomarkers present during the early stages of infection. Thus, one of the main challenges of the optical methods is to enhance the sensitivity in order to be able to perform early detection of protein.

In the past two decades, fluorescence based imaging has become a valuable tool in research and biomedical diagnostics and has played a major role in the progress of biology, disease diagnosis, and life sciences [32, 33]. This is due to the increased usage of fluorescent proteins, probes, and dyes which have enabled non-invasive studies of gene expression, protein-protein interactions, protein function, and a large number of cellular processes[34, 35]. The methodology of using fluorescently tagged proteins as biomarkers in particular has been an attractive approach in molecular imaging due to their inherent sensitivity and molecular specificity [36, 37]. Extrinsic fluorophores such as small organic fluorophores have been suitable for attaching to biomolecules such as peptides, proteins, and oligonucleotides because they are relatively small, minimizing the steric hindrance that can interfere with biomolecule function. This also increases the possibility of several fluorophores getting attached to single molecule, thus enhancing the fluorescence signal [38]. Furthermore, the commercial availability of functionalized dyes combined with established labeling protocols to proteins have dramatically increased its usage for fluorescent methods. Near infrared (NIR) fluorescent probes have also

emerged as versatile labeling tool due to their large absorption cross sections and fluorescence quantum yields which dramatically increases the image contrast[39]. The use of organic fluorophores such as rhodamines, cyanines, and oxazines suffers from photobleaching, low quantum yields, spectral overlaps, and changes in the excitation/emission profiles due to local molecular environment changes such as pH, H_2O, O_2, and interacting ions[40, 41]. Furthermore, the organic fluorophores are prone to photobleaching since they are not as photostable under ambient conditions [42, 43]. Another common challenge in molecular imaging is to increase the signal to noise ratio (SNR) to achieve a detectable signal for the biomarkers.

There are several approaches to enhance the spectral properties of organic fluorophores. These include (1) replacing single molecule labels with high brightness dye-doped silica particles and (2) using nanostructured metallic surfaces to enhance the fluorescence intensity by localized surface plasmon (LSPR) effects [44]. In the past fifteen years, research has demonstrated that engineered metallic substrates such as islands, nanoporous surfaces, nanoparticle dimers, and bow-tie antennas have tremendous potential to enhance the fluorescence intensity from 5 to more than 1000 fold [45-53]. The enhancement is thought to occur by the principle of metal enhanced fluorescence (MEF). Some studies have shown that by generating engineered surfaces with Au features that are sharp tipped and having gaps of nanometer size range between, significant enhancements in the fluorescence signal can be achieved. Other groups have shown that positioning dye molecules nanometric distances from non-metallic surfaces such as SiO_2 could enhance the emission by up to 20 times relative to a glass slide.

For significantly enhancing the sensitivity of optical biosensors, it is essential to fundamentally understand the materials already in widespread use in an effort to improve them and to develop novel advanced materials. This work investigates the use of shrink wrap film to

create a variety of structures that could potentially be used as sensitive biosensors for disease detection. The objective of this dissertation is to research, develop, test, and characterize shrink wrap structures for use as biosensors.

1.2 Structure of the dissertation

The remainder of this thesis is organized as follows: In chapter 2, an overview of top-down and bottom-up approaches is presented, followed by applying some of these techniques on our shrink wrap film to create a multitude of tunable structures. In chapter 3, a background of plasmonics is given and the optical properties of the tunable structures characterized. In chapter 4, the application of the wrinkle structures is demonstrated in one photon excitation for enhancing the fluorescence signal of labeled biomolecules. Chapter 5 illustrates the applicability of using the wrinkled structures to enhance the fluorescence signal of a single labeled biomolecule by two-photon excitation. Chapter 6 describes non-metallic structures generated using shrink film to enhance the fluorescence signal of labeled biomolecules for far-field fluorescence enhancements. Chapter 7 summarizes the work presented in the dissertation and present future studies that could be investigated by future researchers.

Chapter 2: Nanofabrication Techniques

2.1 Introduction

The field of nanotechnology has seen significant progress made in recent years to create and engineer structures that have dimensions between 1-100 nm by utilizing various nanofabrication techniques[54-56]. Nanofabrication involves the design and manufacture of devices on the nanometric length scale to provide structures and patterns for various applications in nanotechnology. The development in these nanofabrication technologies has led to an emphasis on improving health-care, providing more sensitive biosensors, and surfaces with unique properties and optics for detection. However, to continue creating new nanomaterials for these applications, nanofabrication approaches that allow the ability to control the structural, mechanical, optical, and electronic properties with fine precision is important. Generally, the nanofabrication approaches that have been applied to create nanoscale structures can be classified into two major categories: top-down and bottom-up methods [57].

2.2 Top-down approach

In a top-down approach, external equipment is used to direct the nanofabrication tools for patterning nanoscale size structures on a substrate. Typically, these top-down nanofabrication approaches require starting with a substrate and depositing thin layers of metal films, patterning features on surfaces using lithographic approaches, or etching materials to create features[58]. Various lithographic methods have been applied in the top-down approach including serial and parallel techniques for patterning nanoscale features. Common lithographic approaches include photolithography, nanoimprint lithography (NIL), electron-beam lithography (EBL), and focused ion beam (FIB)[59]. Usually, the main substrate is protected by a mask and any unprotected material is etched away via wet-etch or mechanically etched using ultraviolet light, X-rays, or

electron beams. Lithography is mainly used to create a desired pattern in a resist coated substrate and then transfer that pattern over to another substrate.

Conventional lithographic techniques such as optical photolithography have been the workhorse for high fidelity patterning since its introduction in the 1960s due to its ability to pattern features at the micrometer to sub-micron scale[60]. In photolithography, light passes through a photomask and creates an image on a wafer coated with a thin film of photoresist. The photoresist is an organic light-sensitive material and two different types could be used: positive or negative[61]. With a positive photoresist, when the material is under illumination, the exposed regions are highly soluble in developing solutions. The exposed photoresist is then removed in solution. On the other hand, a negative photoresist material will become cross-linked when exposed to light and experience a high solubility in developing solution. After the developing solution, the areas not exposed to light will be etched away. However, photolithography is limited in resolution due to the diffraction of light and hence features smaller than 200 nm are practically not able to be patterned even with the most state of the art facilities[61]. The lens numerical aperture (NA) is a critical parameter in the resolution limit of photolithography[62]. The NA is defined as

$$NA = n\sin(\theta) \qquad (2.1)$$

Where n is the refraction index of medium which light travels and θ is the maximum angle of light collected at focal point. Using the Rayleigh criterion, the minimum distance imaged by the lens is given

$$L_{\min} = 0.61 \cdot \frac{\lambda}{NA} \qquad (2.2)$$

Nanoimprint and interference lithography (IL) are other lithographic techniques which are capable of creating high-throughput patterning of nanostructures [63]. In NIL, a mold that has nanostructures on is transferred over to thin resist cast by embossing the structures into it. The mold is removed and reactive ion etching (RIE) is implemented to remove residual resist. However, similar to photolithography the resolution is diffraction limited. On the other hand, IL has the ability to pattern periodic features without using photomasks as required in photolithography. In this process, the interaction between two or more coherent light beams forms a periodic pattern over large areas which are recorded in photoresist media. Unlike NIL, the advantage of IL is that resolution is able to beat the diffraction limit because a very short wavelength 20-40 nm is typically used. However, one of the disadvantages of IL is that alignment of the laser to another structure is not simple. Furthermore, reflections from the light source that are not needed can induce macroscopic modulations over the gratings [64].

EBL has the capability to overcome these limits by beating the diffraction limit of light and fabricating arbitrarily shaped nanostructures with resolution down to less than 20 nm[65, 66]. EBL is a mask-less technology where an electron beam is scanned over the surface of a substrate which is covered by an electron-reactive resist. The de Broglie wavelength for high energy electrons is significantly smaller than light and hence, EBL has the ability to overcome diffraction limits that photolithography encounters[67]. Furthermore, since the spot size of the electron beam can be as small as a few nanometers, fine patterns close to the nanoscale regime can be achieved. The user creates a pattern on the computer and the digital representation of this pattern is used to scan an electron beam over the pattern. The exposed or unexposed regions depending upon which type of photoresist was used are selectively removed in order to create the small structures. EBL has been demonstrated to be a powerful technique that has the ability to

create nanoparticles of random size, shape, and spacing on a substrate. Similar to EBL, focused ion beam (FIB) has been employed to mill features of the nanoscale size directly into a surface. In a FIB system, instead of electrons, a focused beam of gallium ions is used to modify or pattern a design on a substrate [68]. Typically, the accelerated ions have energies that are tens of keV and are strong enough to remove atoms from a surface. The focused spot size of the ion beam can be as small as 10 nm and offers great versatility for creating features that are within this length scale in resolution. FIB also has the capability to deposit materials onto a surface.

The EBL and FIB techniques require the utilization of a scanning electron microscope (SEM) to create such high resolution structures. However, this also means that the price required to make these structures is expensive, tedious, and complicated. Both of these techniques also suffer from low throughput since they perform a pixel-by-pixel scan through the pattern area and a significant amount of time is required (10^7 pixels/s) to generate the desired patterned array[67].

2.2.1. Top-down metal fabrication techniques applied for MEF

Common top-down surfaces that have been engineered to enhance the fluorescence signal include roughened metallic surfaces, metal islands, nanoantennas, nanoporous surfaces, and nanoaperature arrays. Roughened metallic surfaces have been created by depositing metals at a slow deposition rate onto surfaces[47]. With metal thickness smaller than 2 nm, nanoscale metal particles have been deposited on the surfaces and as the thickness increased, the particles became larger. Increasing the thicknesses above 10 nm, the metal films formed a continuous layer. Metal island films such as silver films have been created by chemical reduction of silver nitrate onto a glass surface [69]. In these studies, the silver films were annealed to glass slides by thermal means and were noted to become larger. Nanoporous gold films have typically been fabricated

by taking free-standing thin films of $Ag_{65}Au_{35}$ alloys and exposing them to 70% nitric solution for short time periods of 5, 10, 15, and 20 minutes [70]. The ability to tune the pore sizes was controlled by varying the time the films were exposed in the nitric acid solution. Nanometric apertures of various sizes from 80-310 nm have been milled into gold films by using FIB [71].Yang et. al created an array of silver nanoparticles by combining NIL and electrochemical deposition of Ag nanoparticles [72]. Yoo et. al fabricated an order array of Ag patterns using platinum assisted NIL. The master for the nanostructures was first fabricated using EBL and then transferred over with NIL. Askashi et. al fabricated a Ag grating by thermal NIL and tuned the depth of the gratings by varying the thermal NIL conditions [73]. A similar approach was followed by Shibata et. al who also used NIL to fabricate their silver coated gratings[74]. Corrigan et. al used EBL to generate an array of silver nanoparticles and tuned the interparticle spacing between the nanoparticles from 150-390 nm [75].

Recently, an attractive and inexpensive approach is to nanofabricate metallic features onto shape memory polymers (SMP). SMPs are polymeric smart materials that can be programmed to deform into a fixed temporary shape and then return back to its original shape after introducing external stimuli such as photo, chemical, or thermal [76]. SMPs that require heat as a stimulus are often referred to as thermoplastic elastomers. The recovery of these materials involves the recoiling of polymer chains from a fixed temporary state to a less organized configured state which is accompanied by a conformational entropy change [77]. In the programming process, the polymer is heated above its glass transition temperature, T_g, and can be deformed into a certain shape. During the deformation of SMP, the elastic strain energy is stored and the materials are then heated, stretched, and cooled passed its transition temperature to fix the oriented polymer structure. When heat is applied, the stored elastic stress is released and

the polymer returns back to its original state. The original state is characterized by a cross-linked network of either physical such as intermolecular interactions or chemical such as covalently cross linked. Thermoplastic materials such as polymethylmethacrylate (PMMA), polycarbonate, polystyrene (PS) and cyclic olefin polymers have all been commonly used for research laboratory disposables including microtiter plates and petri dishes[78]. These plastics are attractive because they are inexpensive, robust, possess good optical properties, and their surfaces can be easily modified. Furthermore, since these plastics are compatible with roll to roll processing, patterning large scale features into these plastics is extremely affordable. In the past, textured surfaces have been created by depositing a stiff skin layer such as a thin metal film on a pre-strained substrate. Typically, the pre-straining of the substrate is accomplished by thermal or mechanical expansion. The wavelength size of the wrinkles are characterized by the following relation:

$$\lambda = 2\pi h_s \left(\frac{E_s}{3E_B}\right)^{\frac{1}{3}} \qquad (2.3)$$

where h_s is skin layer thickness, E_s is Young's modulus of the skin, E_B is Young's modulus of the substrate[79]. The amplitude of the wrinkles is proportional to λ and the applied strain (ε) from the substrate. Skin layers have been deposited on elastomeric substrates by either depositing a thin layer of material on a pre-strained substrate or modifying the top layer with plasma, ion beam, or ultraviolet light. Fu et. al first reported the ability to use heat shrink SMP to create wrinkles ranging from nano to micro scale [80]. In their process, a thin layer of Au was deposited onto pre-stressed PS and shrunk by heating past the T_g. When the PS retracted, the non-shrinkable Au film was forced to fold and buckle to generate multiscale wrinkles. The feature sizes of the wrinkles ranged from microns to 200 nm. Huntington et. al improved upon

the resolution limit of the sizes in the wrinkles and generated polymer nanowrinkles 250 to 50 nm by chemically treating PS thermoplastic films with different reactive ion etching (RIE) gases[81]. They were also able to achieve wrinkles smaller than 50 nm by varying the RIE exposure time. Others such as Zhang et. al have integrated their nanoporous surfaces onto heat shrink SMPs to achieve wrinkled nanoporous surfaces [70].

2.2.2 Fabrication of Composite Structures

Introduction

As described in literature, sharp tipped and closely packed metal structures have shown to be advantageous for fluorescence enhancement due to their ability to localize and concentrate the EM field around the surface of the metallic nanostructures when induced by illumination at a resonant frequency. In the seminal work by Fu et. al, a thin layer of Au was sputter coated onto a polystyrene shrinky dink film and upon heating, the PS shrinky dink retracted to a fraction of its size. When the PS shrink dink plastic retracted by 60% in area, the thin metal film was forced to fold and buckle to yield multi-scale wrinkles. The multi-scale wrinkles stemmed from the thermal mismatch due to the difference in the thermal expansion coefficients of the metals and polymer [80]. In their work, it was determined that as the Au thickness was increased from 10 to 50 nm, the wavelength of the wrinkles also increased. In a follow-up study published a year later, bimetallic films composed of silver (Ag) and Au were sputter coated onto the shrinky dink PS to create sharper and more defined structures[82]. Due to the differences in the stiffness mismatch of the combined metals with the non-shrinkable metal film on the SMP, the metal film wrinkled and cracked to generate nanogaps within the wrinkles. Since then our lab has discovered a new heat shrink SMP, polyolefin (PO), that when heated shrinks even further[83]. This PO film shrinks by 95% in area or 77% in length when heat is applied to it. Thus, the first goal was to

create metallic structures by depositing bimetallic films onto the PO SMP and heating. To introduce a bigger stiffness and thermal expansion mismatch between the metals, nickel (Ni) was sputtered as the first layer instead of Ag. The feature sizes of the structures were characterized with techniques such as a scanning electron microscope (SEM) and atomic force microscopy (AFM).

Experimental Techniques

To create the composite structures, the fabrication approach is shown in Figure 2.1(a). 1 mil thick pre-stressed PO shrink film (955-D, Sealed Air Corporation) laminated onto a 3 mil polyester backing was cleaned in isopropyl alcohol and dried with pressurized air. An array of holes, 2 mm in diameter, was created using CAD software (AUTOCAD, Autodesk, San Rafael, CA), and a carbon dioxide (CO_2) laser (VersaLaser VLS-2.30, Universal Laser Systems Inc. Scottsdale, AZ) was used to etch the array into sealing tape (Nunc sealing tape, Thermo Scientific, Rochester, NY). The laser cut tape acted as a mask for the deposition of metals onto the PO shrink film. The tape masks were then adhered on to the top of the PO pieces. For metal deposition, an ion beam sputter coater was used to accelerate 8 kV Ni, Au, and SiO_2 atoms from two ion guns (IBS/e South Bay Tech, San Clemente, CA) onto the masked PO pieces. The tape mask was removed from the metal coated PO pieces and substrates were shrunk by applying heat at 155 °C for 3 min. The PO shrink film contracts upon heating inducing the bimetallic film to buckle into sharp structures and create nano to submicron gaps between the wrinkle structures. This PO shrink film retracts by 95% in surface area, considerably more than previously reported [82]. As a result, smaller, sharper, and more densely packed wrinkled structures were thus created. Post-shrunk, 5 nm SiO_2 was ion-beam sputtered as the dielectric layer on top of the bimetallic structures to create the composite structures.

2.2.3 Characterization of composite structures

We deposited different thicknesses of Au on top of the PO shrink film and characterized the changes in surface topology using a scanning electron microscope (SEM) (FEI Magellan 400XHR SEM) and an atomic force microscope (AFM) (Asylum Research MFP-3D AFM). The Ni thickness was kept constant at 5 nm. Shrunk substrates were sputter coated with 3 nm Au (Q150R S, Quorum Technologies) and SEM images were obtained with 5 kV beam and 4 mm working distance. Figures. 2.1(b-d) shows the SEM images of the composite structures and illustrates that by increasing the Au thickness from 10 nm to 30 nm, the wrinkles become less densely packed and the sharpness at the edges of the wrinkles dissipate, consistent with previous studies [80, 82]. The high magnification SEM images are used to show the various sizes of the gaps from nano to micron (20 nm to 6 μm) between the metal wrinkle structures within a representative 6 μm viewing window.

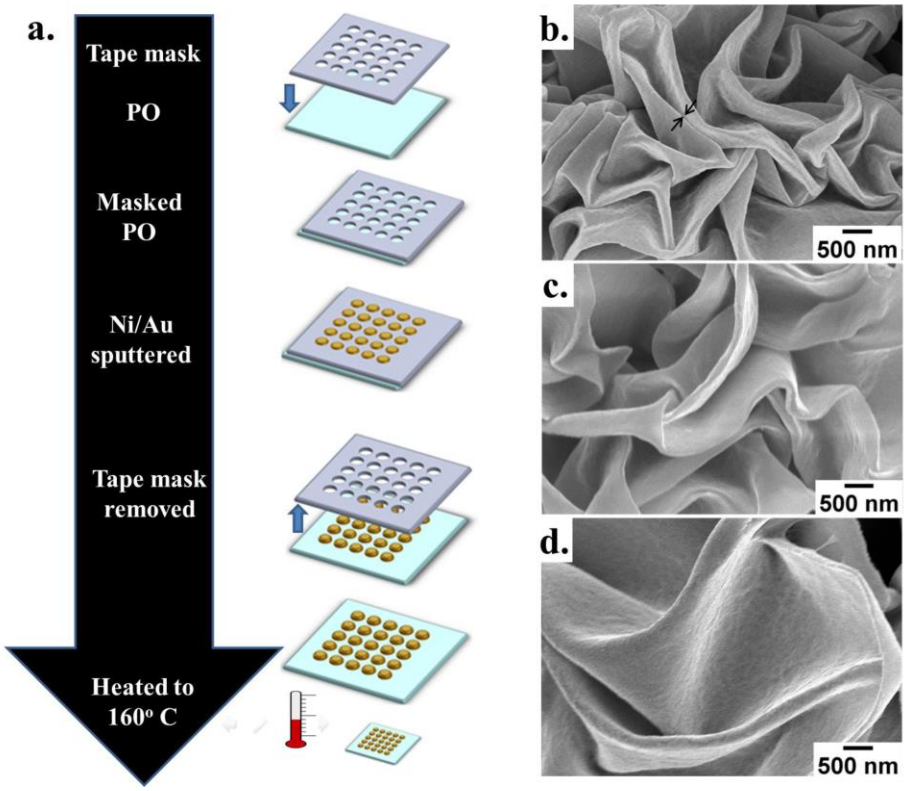

Figure 2.1 Characterization of composite structures (a) Process flow for creating islands of bimetallic structures on PO. SEM images of composite structures with different thickness of Au (b) 10 nm, (c) 20 nm, and (d) 30 nm. Black arrow in (b) indicates a nanogap.

These wrinkle structures are more controllable and robust than other heterogeneous structures, including the nanopetals which we have previously achieved large fluorescence enhancements [46]. Moreover, such wrinkle structures have been extensively characterized and leveraged for various applications [70, 81, 84-93]. Recent work has even shown that the wrinkles can be somewhat deterministic [81].

Figure 2.2 (a-c) shows the SEM images of the composite structures with a fixed Ni thickness of 5 nm and Au thicknesses from 10-30 nm, respectively, within a 20 μm viewing window. These SEM images also depict the same trend as expected by scaling

law that increasing the Au thickness leads to an increase in the size of the wrinkles and a decrease in the sharpness around the edges. Also, through these images, the wrinkles for 10 nm Au composite structures appear to be more densely packed than the 30 nm Au composite structures as revealed earlier in Figure 2.1.

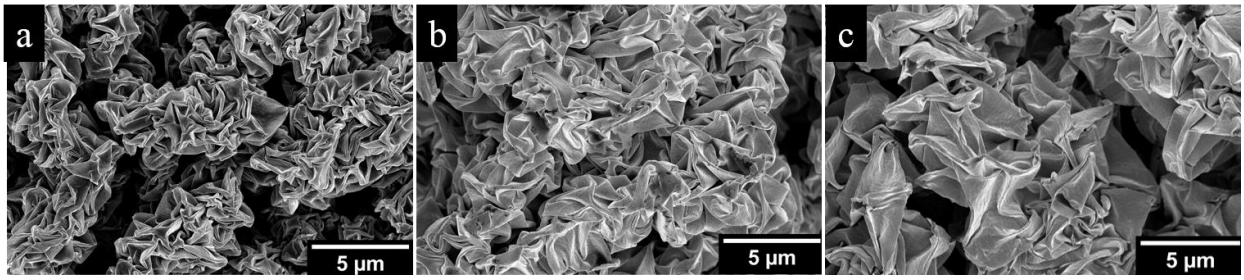

Figure 2.2 SEM characterization of composite structures within a 20 µm viewing window for a fixed Ni thickness of 5 nm and varying thickness (a) 10 nm Au (b) 20 nm Au, (c) 30 nm Au.

Recently, we demonstrated that with a very thin layer of Ni, effective ferro-magnetic nanotraps that localize strong magnetic fields can be formed with these wrinkles[88]. We found that increasing the Ni thickness to 25 nm increased the size and reduced the sharpness of the nanowrinkles and as a result decreased the magnetic strength. To determine the thickness for this study, Ni thickness was thus varied from 5-25 nm, leaving the Au thickness constant at 10 nm (Figure 2.3). As expected and consistent with scaling laws, thicker layers of Ni resulted in larger structures presented in Figures 2.3 (a-c). Therefore, for this study, 5 nm of Ni was used throughout.

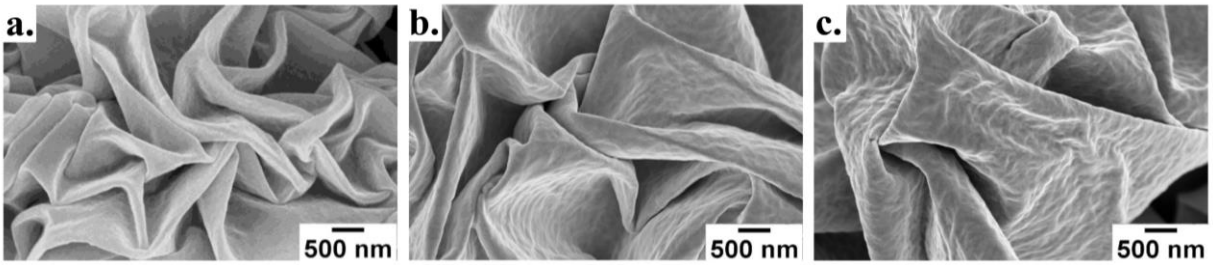

Figure 2.3 SEM characterization of composite structures with fixed 10 nm Au and varying thicknesses of Ni (a) 5 nm, (b) 15 nm, (c) 25 nm.

The previous work by Fu et al. deposited thin metal films composed of Ag and Au on a sheet of shrinky dink polystyrene to create their cracked, nanopetal structures. We also explored depositing thin films of Ag and Au onto the PO SMP and compared the morphology of the metallic structures to the composite structures, post heating. Figure 2.4 illustrates that while wrinkled metallic structures are also created with these Ag and Au films, the wrinkles appear to be larger and somewhat smoother around the edges than the Ni/Au composite structures. According to literature, the young's modulus for Ni is between 117 and 174 GPa for thicknesses between 2 and 10 nm while for 10 nm Au, young modulus has been calculated to be around 100 GPa. For the previously published paper by Fu et. al, the young's modulus of Au and Ag for 80 nm thickness were similar, 80 and 83 GPa. We believe that due to this additional difference in the stiffness mismatch, we are able to achieve wrinkles wavelengths smaller than previously published.

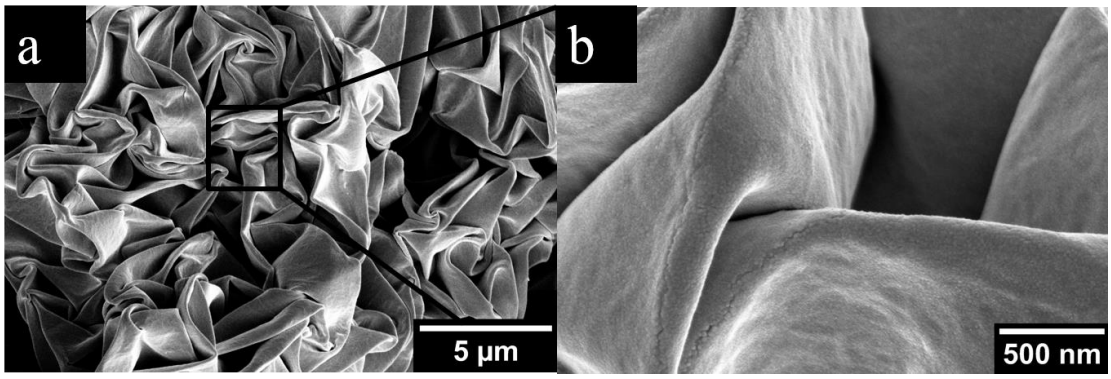

Figure 2.4 SEM images of composite structures with 5 nm Ag and 10 nm Au (a) zoomed out (b) zoomed in

We also looked at the effects of heating the PO metal film to different temperatures past its T_g. Heating the PO metal film to different temperatures results in the PO shrinking to different degrees. Thus, in addition to studying the effects of the Au thicknesses on the morphology of the structures, the substrates were shrunk partially to 40% (115^o C) and 70% (130^{o}C) in area. The morphologies for these structures were characterized by SEM as shown in Figure 2.5.

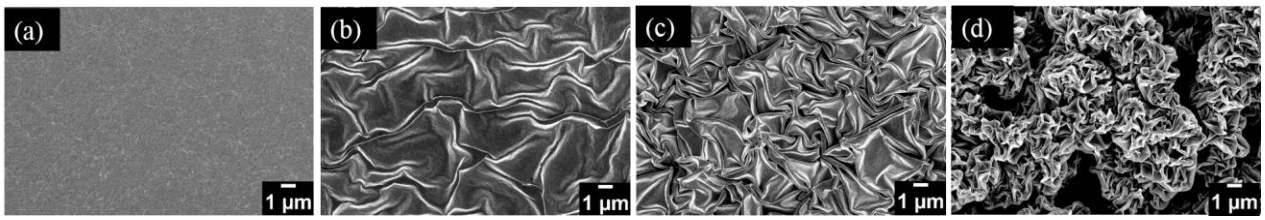

Figure 2.5 SEM characterization of structures created by shrinking the metallic film to various degree of shrinkage in area (a) 0%, (b) 40%, (c) 70%, and (d) 95% in area.

Figure 2.5(b) shows that with 40% shrinkage in area, the wrinkles are beginning to form but the gaps within the wrinkles are large. Shrinking further to 70% leads to smaller wrinkles and an increased probability of nanogaps between the wrinkles. At full shrinkage, the wrinkles are clearly defined and gaps are pervasive throughout the wrinkles. The surface topology of the flat metal and composite structures was further characterized using a modified version of the tapping

mode of an AFM. Figure 2.6(a) illustrates that with just 5 nm Ni, the morphology of the surface was observed to be rough and riddled with defects. With the addition of 10 nm Au onto the 5 nm Ni surface, the surface was noted to transition to a smoother, continuous surface.

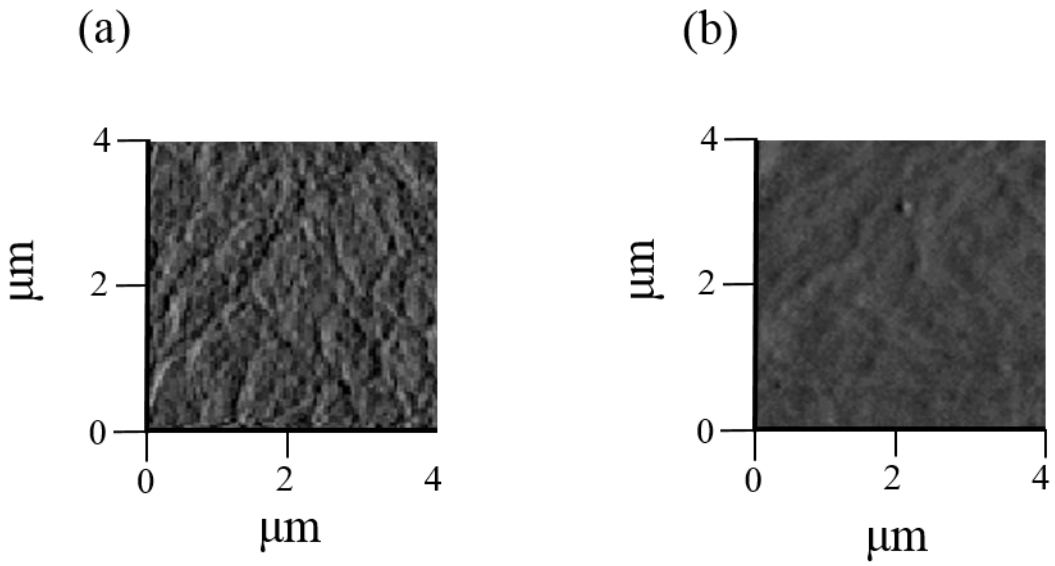

Figure 2.6 AFM images of the morphologies of the flat 5 nm Ni film and (b) sputtered with an additional 10 nm Au (a) Flat 5 nm Ni on PO (b) 5 nm Ni, 10 nm Au on PO

The height topology of the flat metals films and composite structures are presented in the Figure 2.7 (a-b). Figure 2.7 (a) illustrates that the metal film is filled with surface defects that causes variations in the height profile but overall the film is relatively flat. Another interesting observation that can made is that that the morphology of the flat metal films are composed of tiny islands of metal film. With the addition of 10 nm Au, the metal film becomes smoother as illustrated in the AFM profile. However, the three-dimensional view of the composite structures reveals that a distribution in the heights from the nm up to 3.6 µm can be observed Figure 2.7 (b).

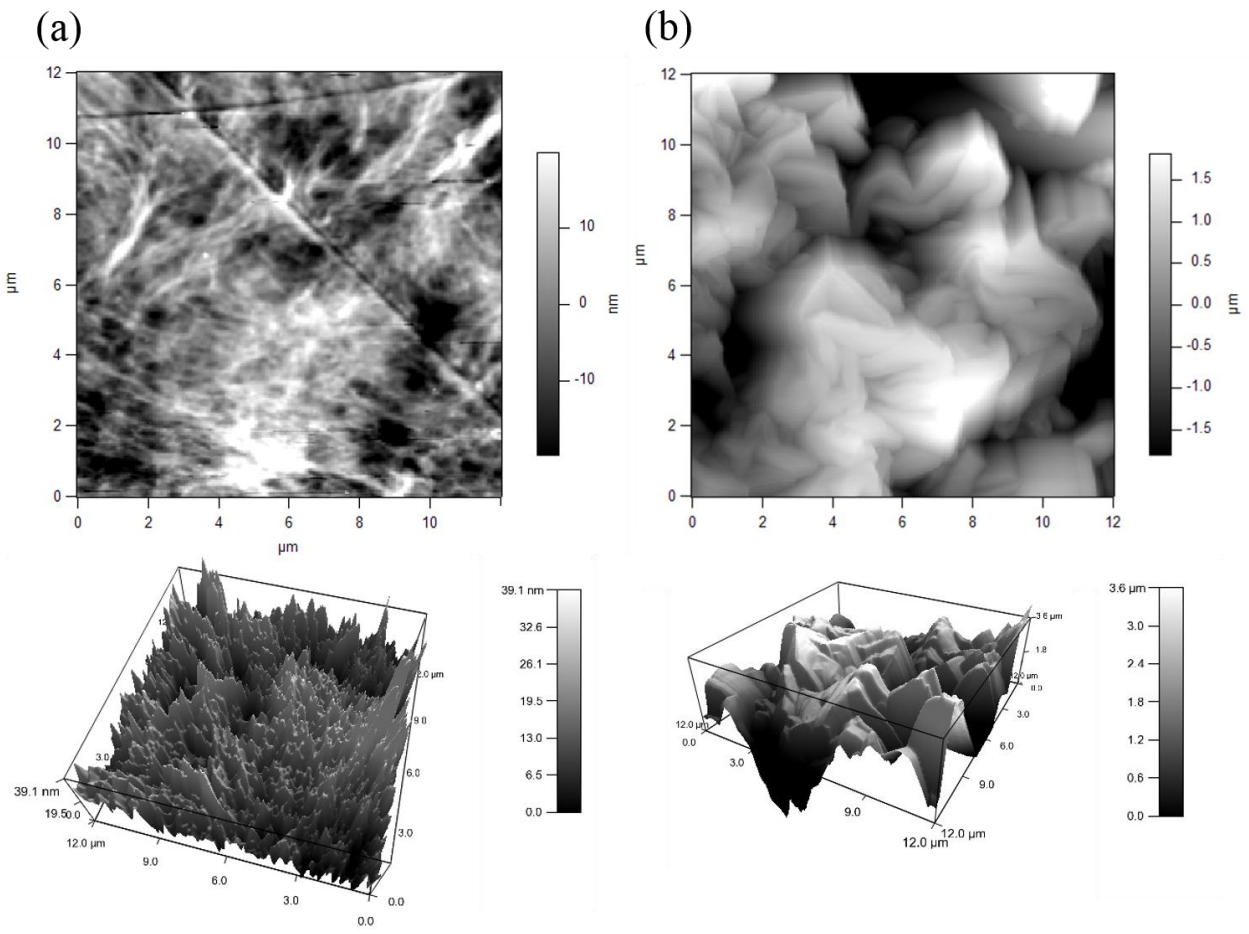

Figure 2.7 3D AFM image of the morphology and height distribution for (a) Flat 5 nm Ni, 10 nm Au on PO (b) 10 nm Au composite structures

Energy dispersive spectroscopy (EDS) was also performed on the 10 nm Au composite structures to determine the surface composition of the Au wrinkles which we predicted to be mainly Au and Ni with some SiO_2 (Figure 2.8).

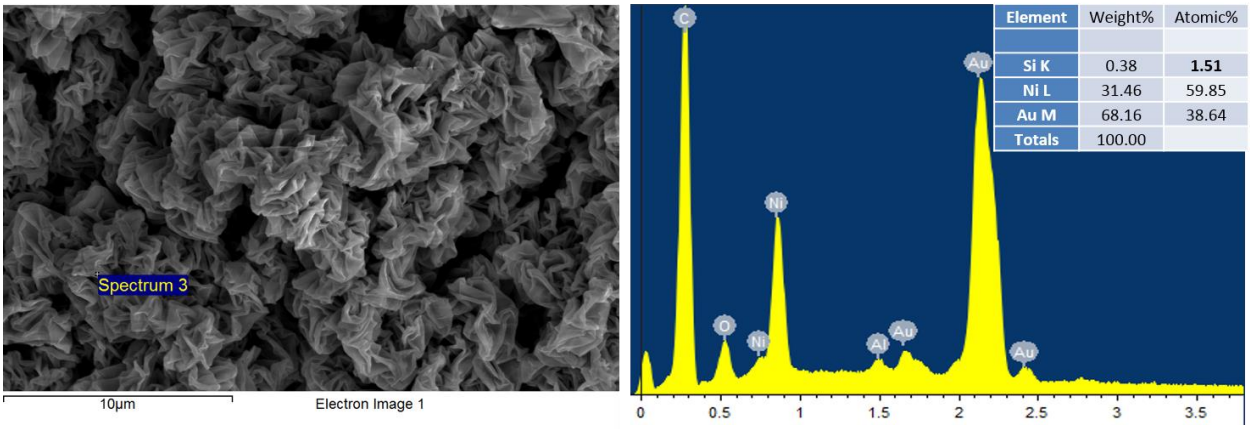

Figure 2.8 EDS characterization of 10 nm Au structures

EDS is a widely used elemental analysis technique that has been used in conjunction with SEM. In this method, an electron beam from the SEM bombards a solid sample, ejecting the electrons and creating vacancies which are subsequently filled by electrons from a higher state[94]. To balance the energy difference between the two electrons' states, x-rays are emitted and the energy is correlated to the element it was emitted from. The EDS spectra reveals that after the 10 nm Au composite structures were created, the wrinkles were composed of about 69% of Au, 31% of Ni, and 0.4% of Si. One of the challenges with EDS is that the electron beam penetrates deeps into the sample and thus the top surface might actually have a higher percentage of SiO_2. However, to confirm that the upper layer is mainly Au, focused ion beam (FIB) should be done to slice the top part of the surface and then perform EDX analysis.

Measuring the contact angles on the composite structures indicates that the surfaces are superhydrophobic because their contact angles are greater than 150^o (Figure 2.9). A surface that is superhydrophobic is not able to support the spreading of drop or wetting at the plane of contact in an aqueous environment.

Figure 2.9 The profile for a water droplet on 10 nm Au composite structures

Although the surfaces were revealed to be superhydrophobic, studies have been done with superhydrophobic surfaces for single molecule detection using spectroscopic techniques. Angelis et. al. utilized their superhydrophobic surfaces to detect attomolar concentrations of DNA molecules using SERS[95]. Scopellit et. al found that with the increased roughened surfaces at the nanoscale, a 500% increase in BSA protein adsorption was observed over the allowable coverage amount[96]. They concluded that the adsorption of proteins was regulated by surface nanostructures, in particular the nanometer pore shape. Similar work by Pirouz et. al and Mahmoudi et. al [97, 98] have confirmed that nanometer scale roughness plays a significant role in protein adsorption.

2.3 Bottom-up approach

Bottom-up processes are a cheaper alternative to top-down approaches that do not necessarily require the use of expensive machinery. Bottom-up nanofabrication approaches typically use molecular or atomic components as the building blocks to construct more complex nanostructured assemblies. In nature, there are several examples of materials made using bottom

up approaches such as DNA, RNA, and protein [99]. A bottom-up process typically involves the chemical synthesis of particles, molecular self-assembly, or vapor-liquid growth in the form of using electrolysis or reduction of ionic compounds in solution for chemical deposition of material.

2.3.1 Bottom-up metal fabrication techniques

Examples of plasmonic structures created using bottom-up techniques include metal nanoparticles, nanowires, and nanorods. Gold nanoparticles are typically synthesized by the chemical reduction of Au(III) to Au(0) by using sodium citrate as a reducing agent[100]. The citrate agent serves as both a reducing agent and capping agent that prevents the Au NPs from generating larger particles. Tuning the size of the particle can easily be achieved by simplify varying the Au/citrate ratio. Nanorods are most commonly created by the seed-mediated approach developed by Murphy's group in 2001[101]. In their method, spherical seed nanoparticles are added to a solution composed of gold salt, silver nitrate, ascorbic acid, and cetyltrimethylammonium bromide (CTAB). This eventually leads to the formation of gold nanoparticles which have a rod-like morphology. The gold salt in growth solution is gently reduced in the presence of seed particles while the CTAB helps with rod formation by binding to the side facets of the nanoparticle. To tune the length of the gold nanorods, the amount of silver nitrate additive is varied. Nanoantenna arrays have been created by coupling metal nanoparticles close to each other so that within the nanogaps, interesting effects can be observed[102].

2.3.2 Colloidal lithography

Within the fields of chemistry, material science, and optics, colloidal lithography has been applied extensively for research. Colloidal crystals have been used for photonic applications along with applications in antireflection coatings, sensors, optical filters, porous

membranes, lithographic masks, and for surface enhanced Raman microscopy applications. Colloids are a group of insoluble particles that are on the order of less than a micron in size and are dispersed well in a solvent. In 1980, Peiranski discovered that when these particles were arranged in a periodic array, they form colloidal crystals [103]. However, a year after this discovery, Fisher and Zingsheim showed the most important aspect of using a monolayer of colloidal spheres was that when applied as a mask, structures smaller than the wavelength of light could be formed[104]. Deckman et. al expanded upon the method and demonstrated that the technique could be applied for surface patterning in large areas[105]. However, it was not until the 1990s that it was recognized by Van Duyne et. al that when metal was evaporated onto the colloidal spheres, tetrahedron metal nanostructures could be created on the substrate[106]. Since then, significant advances have been made in the field of colloidal lithography or now more commonly referred to as nanosphere lithography. Nanosphere lithography offers several main advantages over other conventional lithographic techniques such as photolithography, EBL, FIB lithography, or dip pen lithography to create patterns on the surfaces. Photolithography is limited by the diffraction of light in resolution, but colloidal lithography is able to overcome this by creating interstitial sites between the colloidal spheres which can be less than wavelength of light. Unlike, EBL, FIB, and dip pen lithography, the process is easily adoptable and inexpensive since minimal machinery is required to create the patterns. Furthermore, the method is rapid and multiple samples can be fabricated simultaneously.

Monodisperse microspheres such as polystyrene (PS) or silica, SiO_2, have the ability to self-assemble into single and multilayers that are a hexagonal closed pack array. In order to fabricate these arrays, a variety of methods have been applied such as dip coating, spin coating, and drop coating [107]. The stability of the colloidal spheres is governed by a balance between

the attractive Van der Waals forces and repulsive forces which can be electrostatic[108]. This electrostatic force between the particles are affected by the ionic strength and has been shown to affect the quality of colloidal crystals. The DLVO theory, named after Deraguin Landau Vervey Overbeek, has been introduced to describe the interactions between the colloidal spheres and the competing effects of electrostatic repulsions and attractive Van der Waals forces. Briefly Van der Waal forces are attractive forces that occur over short distances (<10-20 nm), and are the collective effects of permanent dipole/induced dipole interactions (Keesom interactions), permanent dipole/induced dipole interactions (Debye interactions), and induced dipole/induced dipole interactions (London interactions).

Most of the self-assembly process require solvent evaporation from a droplet of colloidal nanosphere particles in suspension. As the liquid starts to evaporate, the water level approaches a height that is on the same order as the dimensions of the colloid. A meniscus is formed between the particles and the liquid film around the particle deforms. As a result, attractive capillary forces emerge to form the self-assembly of the particles. The spheres self-assemble into a close-packed hexagonal array because thermodynamically, the Gibbs free energy is minimum and chemical equilibrium has been achieved[109]. These capillary forces also play a role with particles at the air/water interface. More important, it was determined that the main factor for the self-assembly process was the attractive capillary forces and convective transport of the nanospheres. The key to a successful ordered array, though, is the rate of solvent evaporation. In particular adjusting the temperature and humidity of the system significantly affected the array assembly. Other important factors that have been realized through investigation are tuning the concentration of particles, particle size, surface charge, and hydrophobicity of particles.

Compared to conventional lithographic techniques, bottom up approaches do not provide as much control, but are significantly cheaper, convenient, and less labor intensive. Nanosphere lithography (NSL) is one of the most inexpensive and convenient techniques that have been used to fabricate a close packed array of nanospheres. These nanospheres have also been tailored to generate various nanostructures such as nanopores, nanopillars, nanowires, and nanoholes on solid surfaces[110]. Nagayama et. al developed a method that utilized dip coating to assemble colloidal nanospheres into a hexagonal pack as the liquid slowly evaporated [111]. In their method, they closely adjusted the withdrawal speed of the substrate and monitored the evaporation rate to obtain large 2D ordered arrays. An improvement in this method was developed by Nagao et. al where they dropped a volume of colloidal suspension on the substrate and inclined the substrate vertically until it was dried[112]. With this dip coating method, controlling the rate of evaporation properly was still a challenge and generally took a long time before the solvent evaporated. A way to speed up the evaporation rate is to utilize a spin coater to spin coat the colloidal suspensions onto the substrate [113]. With a spin coater, the spin speed, size of the nanosphere, and wettability play an important role in the self-assembly of a monolayer of colloidal nanospheres. The thickness of the evaporating film has shown to be inversely proportional to the spin speed. Rehg and Higgs, Dushkin et. al, and Colson et. al. showed that a rapid evaporation rate is one of the best parameters for achieving high hexagonal close packing [114, 115].

2.3.3. Nanopillars

Periodic arrays of sub-wavelength structures have garnered significant interest for surface enhanced Raman spectroscopy (SERS) and metal enhanced fluorescence (MEF), and for anti-reflective coating properties. For SERS and MEF, coupling metal nanoparticles with nanometer

scale spacing can induce strong local electromagnetic field enhancements at the plasmon resonance significantly increasing the Raman signal or fluorescence of a molecule. Inspired by moth eyes, metal nanoparticle arrays can also reduce the reflection of incident light, shown useful for improving the efficiency of solar cells. Tuning the localized surface plasmon resonance in noble metal structures is pivotal in optimizing a wide range of applications, such as nanophotonic devices[116-118], biological sensors[119, 120], and photovoltaics[121]. The highest enhancement factors for surface enhanced Raman spectroscopy (SERS)[122] and metal enhanced fluorescence (MEF)[123], currently greater than 1x10^9[124] and 1,100 fold[125],respectively, are attained when the plasmon frequency is between the frequency of the incident light and that of the light emitted from the analyte molecule[126]. The ability to tune the resonance frequency is largely dependent on the ability to control the materials, size, shape, and periodicity of nanostructures. This has been mainly achieved using top-down methods such as electron beam lithography, focused ion beam lithography, and dip pen lithography. For instance, Caldwell et all, has used e-beam lithography to generate Au nanopillar arrays, with diameters ranging from 320 nm to 120 nm and distances from 270 nm to 60 nm, with uniform enhancement factors as high as ~1.2x10^8 [127]. However, as mentioned previously, these traditional top down methods are not adoptable commercially, due to high cost, long process time, and low throughput. Bottom-down approaches such as nanosphere lithography[128] offer more robust and cheaper solutions. NSL can be applied to create nanopillars by using simple etching techniques to reduce the size of the self-assembled nanospheres and etch into the substrate. In work by Lim et. al, nan pillar arrays, similar in resemblance to the cones in a moth's eye, were fabricated on both sides of glass using NSL, resulting in a 99% transparency in the visible region [124]. By tuning the height and pillar shape, they were able to tune the frequency region in

which the AR properties occurred. However, the spacing between pillars, which plays a direct role in the refractive index gradient, remained fixed, due to the inherent inability of NSL to alter periodicity independently of structure height and size. Deckman et. al demonstrated that tall post-like structures could be generated on a substrate by reactive ion milling a silicon wafer that was masked by polymeric spheres[129]. The shape and height of the post could be tuned by changing the reactivity of the ion beam. Kuo et. al showed that fabrication of Si nanopillar arrays could be achieved by also using RIE to obtain nanopillars with diameters as small as 40 nm with tunable gap distances between 20-80 nm[130]. Cheung *et. al* created nanopillars by self-assembling polystyrene (PS) beads onto a silicon surface and then reactive ion etching (RIE) with oxygen to reduce the size of the beads [131]. Following this, deep RIE of silicon was performed for specific times in order to generate the pillar structures of various heights. A similar technique was used by Sainiemi *et. al* to create high aspect ratio silicon nanopillars that could be used for chemical analysis[132]. Valsesia et. al functionalized the surfaces of their nanopillars by selective immobilization of bovine serum albumin (BSA) through EDC/NHS chemistry [133]. Wu et. al employed NSL, oxygen plasma etching, and E-beam evaporator to create nanocorals that had rough surfaces which was used for SERS detection[134]. Unlike most other previous techniques, Wu et. al released the nanocorals into water similar to a colloidal suspension. More recently, Wu *et. al* fabricated a macroporous Ag film by using NSL to assemble PS microspheres into a monolayer and then also used water to release the PS microspheres before re-loading monolayer onto another silicon wafer [135]. The monolayer was used as a template to fabricate an inverse opal silica film before immobilizing AuNPs onto the film. Following this, the Ag nanosheet was created by immersing the AuNPs coated inverse opal film into a silver nitration solution mixture. Another interesting approach is to deposit thin Au

films onto the self-assembled PS nanospheres. A coating of Au is formed on the upper part of the hemispheres and a small Au dot array on the substrates in the interstices between the PS nanospheres. Caldwell *et. al* deposited Ag by atomic layer deposition to cover their silicon nanopillar templates and reduce nanopillar gaps to less than 2 nm from where plasmonic hot spots were observed[136].

One of the interesting aspects of metal nanostructures is that the plasmonic properties also depend on the dielectric environment. A slight change in the refractive index of the dielectric environment can cause a shift in the absorption peak of the LSPR sensor. However, recently it has been demonstrated that immobilizing metal particles directly onto solid substrates creates an inhomogeneous environment around the particles[137]. This is related to the fact that refractive index is affected by a combination of the substrate and medium. However, since the refractive index is not affected significantly by changes in the environment, the sensitivity is lower. To introduce a larger gap between the substrate and electromagnetic field around particle, placing metal particles on top of prefabricated pillars can be an effective way to improve the spectral overlap.

2.3.3.1. Nanopillar structures on shrink film

Ideally, new techniques which combine the best of both top down and bottom methods should be explored. In this section, a versatile technique to fabricate an array of nanopillar like structures is described. By integrating the advantages of nanosphere lithography to generate a hexagonal closed pack array of PS beads onto a heat shrink SMP, polyolefin film (PO) and the ability to shrink to different degrees, tunability with the structures is shown. Oxygen plasma etch is used

as an independent parameter to vary the size of the PS beads and the height of nano bead-pillars. This is accomplished as shown in the process illustrated in Figure 2.10.

Experimental

Polyolefin (PO) films (955-D, Sealed Air Corporation) with thickness of approximately 1 mil laminated on a 3 mil polyester backing were cleaned in isopropyl alcohol and then dried with pressurized air. The clean PO film was then oxygen plasma treated for 30 s at a power of 60 W to increase the hydrophilic nature and change the surface energy of the PO surfaces. A solution of 500 nm polystyrene (PS) beads (Bangs lab) was diluted to a 1:1 ratio with triton X-100 and methanol (1:400 by volume). Approximately 12 µL of this solution was then spin coated onto the PO film for 5 minutes at 1200 RPM and allowed to dry for four hours up to overnight. After spin coating, the substrate was plasma etched at a power of 60 W in an oxygen plasma asher for different times. The times selected for etching were 540s, 630, 730, and 810 s. Immediately following the plasma etch step, samples were sonicated in ethanol for a minute and subsequently sonicated in deionized (DI) water to remove residual etchant material. The samples were left to air dry overnight. The substrates were then mounted with double-sided tape onto a glass slide and placed in a convection oven. The substrates were heated from room temperature (23^{o}C) to different temperatures ranging from 90 °C to 115 °C. As the substrate started to shrink during the heating process, the percent changes in length from the original size were recorded with a digital caliper. The ratio of the final width of the substrate relative to the initial width was used to calculate the percent change in length. With electron beam vapor deposition, the substrates were coated with a 5 nm titanium adhesion layer and 50 nm Au. During the metal deposition process, the temperatures did not exceed past 115° C in order to avoid shrinkage to the substrate. An

atomic force microscope (AFM) (Asylum Research MFP-3D AFM) with silicon cantilevers (Olympus) was used to characterize the resulting topography of our substrate, and a scanning electron microscope (SEM) (FEI- Magellan 400 XHR), at ~ 2 Kv, was used to image the surface topology of the structures.

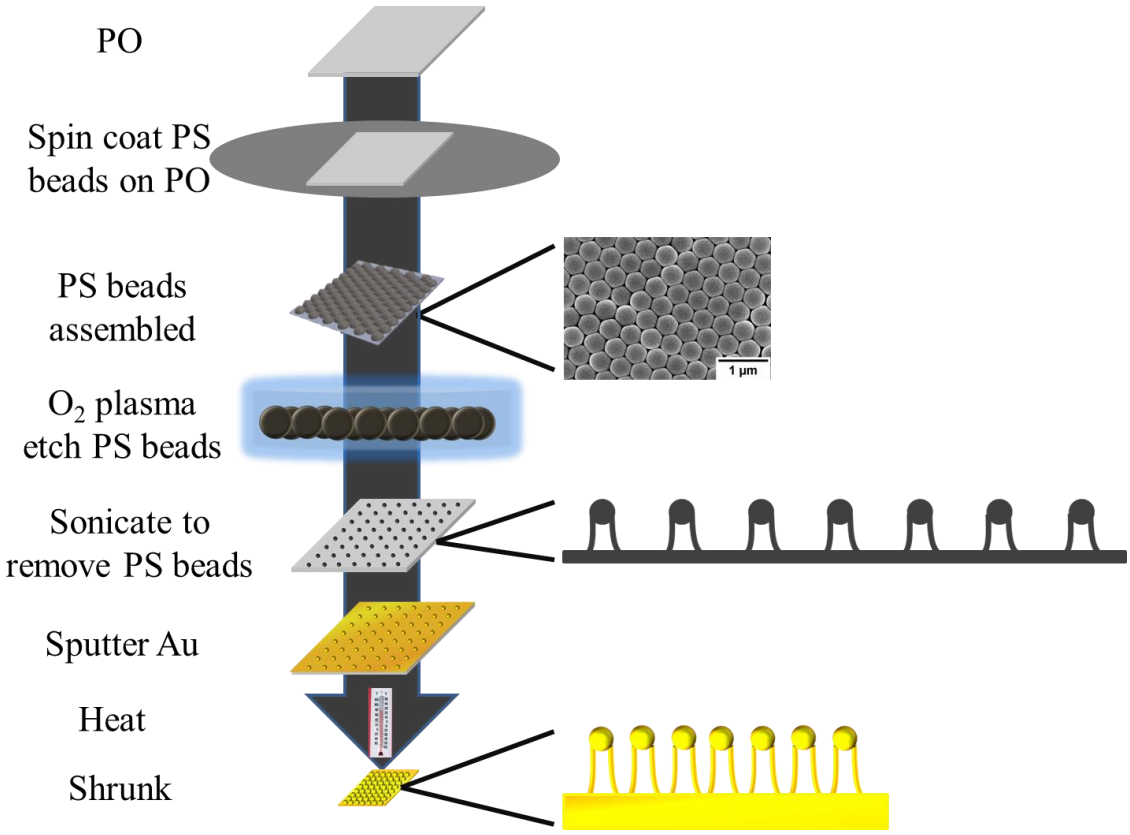

Figure 2.10 Schematic process flow for fabrication of nanopillar bead arrays.

The oxygen plasma etch time was varied to determine the etch rate of PS beads and the underlying PO. SEM images after etching are shown in Figure 2.11 (a-d) that have been etched for time periods of (a) 540 s, (b) 630 s, (c) 720 s, (d) 810 s, respectively. These time points were selected because plasma etching of the PS beads was found to be most effective in this time range. For oxygen plasma etch times less than 540 s, minimal etching of the PS beads was observed and past 810 s, the PS beads were noted to have been destroyed. Hence, etching for

time periods between 540 to 810 s led to reduction in diameter of PS beads and also etching into the substrate as revealed in Figure 2.11. As expected as the PS beads are etched for longer time intervals from 540 s to 810 s, the diameter of the PS beads is also reduced. A reduction in the diameter of the PS beads also led to an increase in the interparticle spacing between the nanopillars. The width of the PS beads decreased by approximately 140 nm from 240 nm to 100 nm when the etch time increased from 540 to 810 s. This was also accompanied by an increase of 150 nm with the edge to edge spacing. AFM topography line profiles for the 540 s and 810 s etch time are shown in Figures Figure 2.11 (e and f). These height profiles depict that with the longer etch time of 810 s, the top point of the pillars become sharper relative to the smooth tops observed on pillars after an etch time of 540 s. The height scale legend on the right shows that the heights range from approximately 60 nm for pillars etched for 540 s and up to 160 nm for plasma etch time of 810 s. The height increase is also observed to be monotonic with etch time.

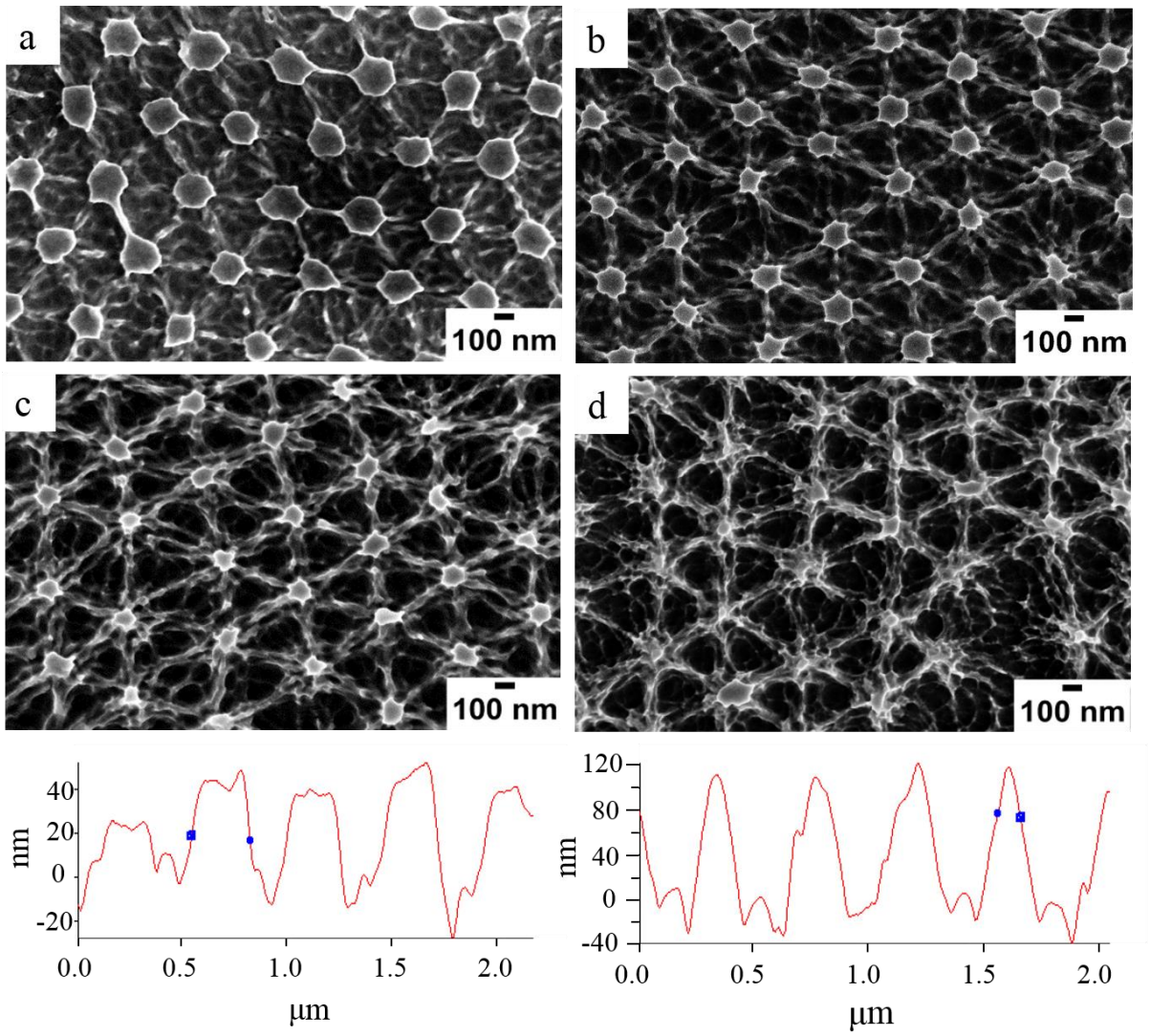

Figure 2.11 SEM images of gold coated 500 nm PS bead arrays that were reduced in size using various plasma etch times: a. 540 s, b. 630 s, c. 730 s, d. 810 s. Scale bar is 100 nm. 2 µm AFM height profiles for samples etched for e. 540 s, and f. 810 s provide the shape of the resulting nanopillar beads.

Figure 2.12 provides a summary of the AFM topography images of the etched beads for the different etch time intervals and also shrunk to different degrees. As mentioned previously

after 810s of oxygen plasma etching, further etching of the pillar features on the surface was not possible due to the obliteration of the PS NSL mask. Thus, the aspect ratio of the structures is limited by the etching of the substrate and PS beads. One possibility that hasn't been explored is that if a higher aspect ratio is needed, reactive ion etching (RIE) can be applied due to the difference in dry etch rates between PO and PS. High-aspect ratio structures are especially important for plasmonic applications where these structures have been correlated with strong local electric fields[138]. Traditionally, NSL has been performed on silicon, Si, substrates to generate pillars with heights up to 400 nm by using selective etching methods, such as RIE, with fluorination or chemical etchants. One of the disadvantages of using surface such as Si though is that on such a hard surface the beads do not adhere to the surface. Thus, sonication in solvents would lead to the easy removal of the beads. Using a soft PO film, the PS beads remain bound to the PO film surface and due to the similarity in the materials, the beads appeared to be strongly adhered to the PO surface. Interestingly enough, sonication of the PS coated PO films in harsh organic solvents such as hexanes and dichloromethane did not release of PS beads. Thus, with a selective etching approach, higher aspect ratio pillars can be attained.

In conventional NSL, the ability to tune the feature sizes once the pattern is created is not feasible. With a heat-shrink SMP, the ability to independently control the feature size and periodicity should be attainable. Figure 2.12 shows a summary of the AFM topography images for PS bead arrays on PO etched for different durations and heated for different time periods. Visually, it can be noted from the AFM images that when the substrate shrinks to different degrees, the spacing between the PS bead nanopillar arrays decrease with a similar percentage. In addition, an advantage of shrinking the substrate is that an increase in 30 nm in the height of the nano bead pillars is noted to occur. From the law of mass conservation, the film must increase in

the Z direction since the film contracts in both the X and Y direction. When the PO shrink film was shrunk to approximately 35% in length, a 30 nm increase in the height was observed. Although the PO film has the ability to retract by up 77% in length when heated to 155ºC, the substrates were only shrunk to approximately 35% in length. This limit is governed by the fact that during the etching process, the PO surface stiffens with the additional skin layer. This thin oxide layer formed during oxygen plasma etching combined with the metal from the metal deposition introduces a stiffer layer on the PO with the PS beads. Thus, when the PO film was shrunk past 35% in length, wrinkles were visible observed to mask the PS bead array. A summary of the differences in the widths, heights, and distances measured for the substrates is presented in Table 2.1. As an added measure for a more quantitative analysis, the same values are also plotted as a function of etch time presented in Figure 2.13.

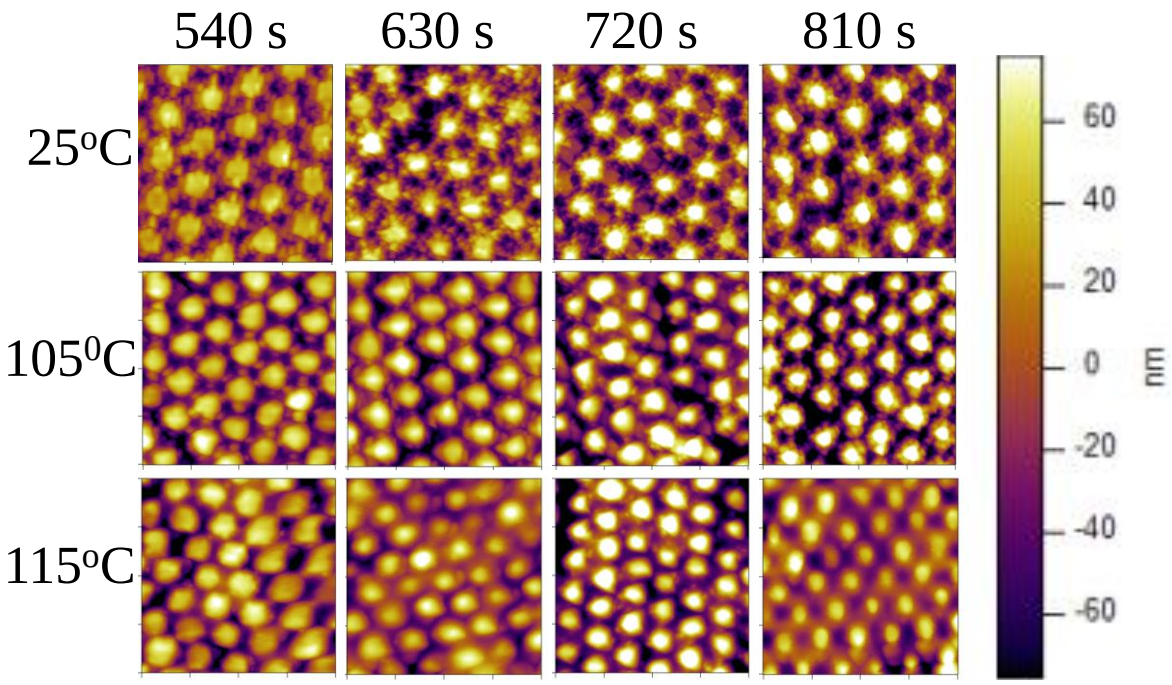

Figure 2.12 AFM topography images of gold coated 500 nm PS bead arrays on PO, etched for different time intervals and then shrunk in size from 0% to 20% to 33% by heating them from 25ºC to 105ºC to 115ºC, respectively.

As presented in Table 2.1 and illustrated in Figure 2.12, the nanopillars do not vary much in width after heating. In theory, shrinking the substrates should result in smaller diameter of the pillars. This may be related to the PO being segmented into small areas when etched into pillars, preventing the normal shrinking expected. The largest measured pillars appear to shrink to a small extent with an increase in temperature. This may be due to the segmented PO still being large enough to decrease in surface area to some small extent. As expected, the center to center spacings decreased as a function of heat. A 35% reduction in the distances was observed or from 450 to 300 nm. The reduction in the spacing correlates well to the change in length of the heat shrink PO after heating. Also, variation in shrinking in the x and y directions of the substrate is noted and attributed to occur due to the asymmetric stretching of the substrate. Achieving control

over this asymmetry is possible by constraining the sample in one direction while heating the other side. The ability to control the asymmetry of the heat shrink PO film will allow more tunability in the nanostructure arrays and maintain the periodicity.

Table 2.1 Gap spacing and width dimensions of PS bead arrays for different etch times and shrink temperatures.

Etch time (s)	**Shrink Temp (^{o}C)**	**Width (nm)**	**Spacing in x (nm)**	**Spacing in y (nm)**	**Height (nm)**
540	25	237 ± 6	452 ± 11	448 ± 10	65 ± 4
540	105	224 ± 5	366 ± 10	384 10	79 ± 3
540	115	215 ± 14	314 ± 9	375 ± 15	85 ± 4
630	25	123 ± 7	451 ± 14	429 ± 19	100 ± 6
630	105	118 ± 7	381. ± 4	376 ± 5	120 ± 7
630	115	119 ± 9	314 ± 4	351 ± 6	125 ± 4
720	25	128 ± 8	438 ± 12	445 ± 10	97 ± 5
720	105	128 ± 4	381 ± 9	380 ± 10	105 ± 6
720	115	126 ± 2	343 ± 10	294 ± 9	113 ± 4
810	25	95 ± 7	439 ± 11	452 ± 9	124 ± 5
810	105	97 ± 5	386 ± 7	356 ± 6	132 ± 4
810	115	92 ± 7	320 ± 11	330 ± 8	143 ± 6

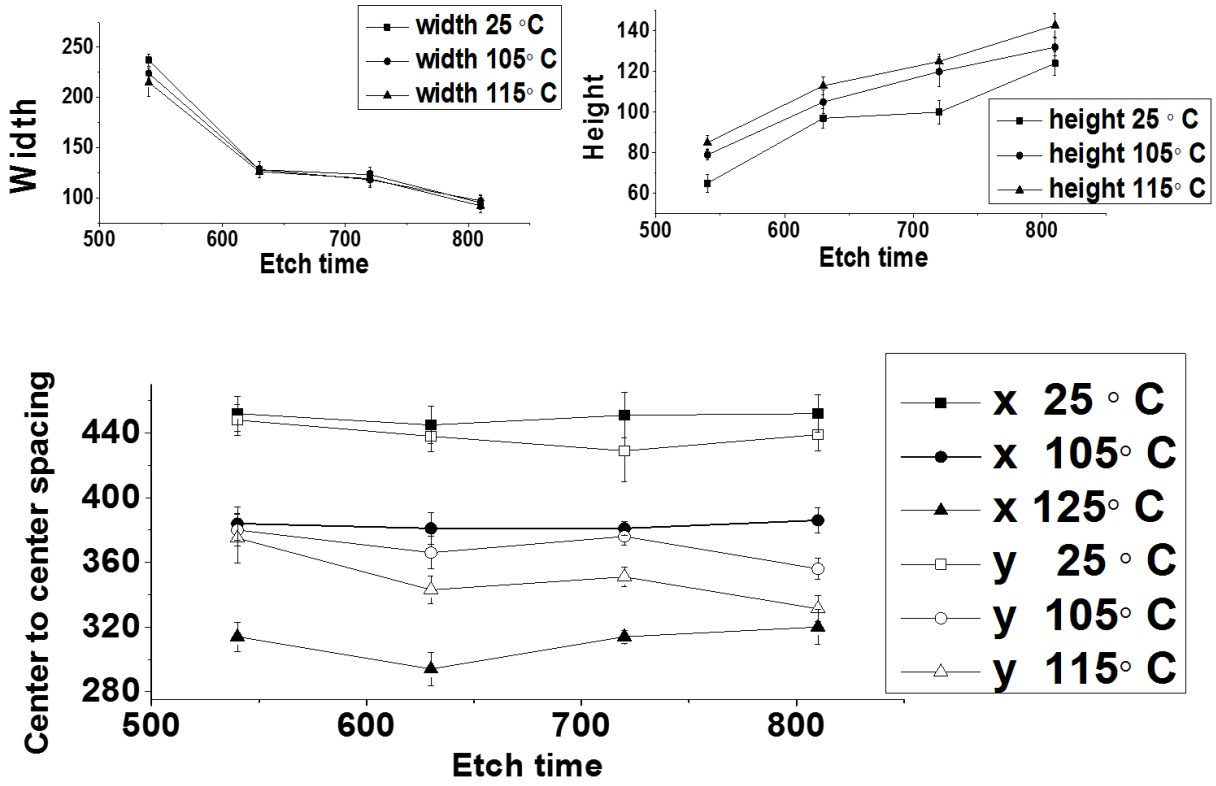

Figure 2.13 Spacing, width, and heights for PS bead arrays shown as a function of etch time and shrink temperatures.

2.3.4 Nanotriangles

The hexagonally close-packed nanospheres can also serve as a shadow mask that can be applied to create nanotriangles of various dimensions. After initial self-assembly of the nanospheres on the substrate, Au can be evaporated onto the surface and deposited through the monolayer mask. The interstices between the PS spheres allows for metal such as Au to be deposited onto the substrate creating an array of triangular shaped particles. Following this, the PS nanospheres can be removed by sonication in an organic solvent such as ethanol to leave behind an array of Au nanotriangles. Between sharp tipped nanotriangles, significant amplifications with the incident electromagnetic field have been demonstrated [139-141]. Fayyaz et. al created an array of Au nanotriangles by E-beam evaporation deposition of Au onto self-assembled PS beads of different

sizes in diameter[142]. They tested different sizes of PS nanospheres and described different heights and distances between adjacent triangles. As anticipated, the heights and distances decreased as the size of the PS nanosphere mask were smaller. Haes et. al applied a similar process to create their Au triangles and used to transmission electron microscopy (TEM) to characterize their surfaces [143]. The TEM images revealed that around the sides of the triangular particles, small spherical nanoparticles with dimensions around 10-20 nm were present. They speculated that during the sonication step, some of the larger particles broke up into smaller particles. Other groups have focused their efforts to control the tip to tip spacing to confine the excitation light to enhance the electric field to different magnitudes. Lohmuller et. al developed a method to control the tip to tip distance in between the gold nanotriangles from 5-100 nm by combining NSL and oxygen plasma etch[144]. During the plasma etch process, the size of the nanosphere particles were reduced as the particles were etched. However, if the spheres were touching each other, then a thread was formed at the point where they were neighboring each other. When metal was deposited onto this mask, the shadows from the nanothreads controlled the final tip to tip distance between the individual triangles. They noted that the mean gap size for their plasma etched conditions had a range but more than 10% of the gaps were smaller than 50 nm. A similar process presented by Dai et. al tuned the tip to tip distance between the neighboring nanotriangles to be as small as 10 nm just by controlling the time the substrates were oxygen plasma etched. Dai et. al created a large uniform array of bowtie nanoantenna array by self-assembling PS particles on silica into a hexagonal pack[145]. The PS masks were reduced in size by using oxygen plasma etch and then Ag was deposited onto the surface. As expected, the diameter of the PS particles was reduced by etching and resulted in enlargement of the opening between the PS particles. Interestingly, though, with an etch time of

180 sec, the PS nanosphere particles melded into each other to create gaps between the triangles that were smaller than 10 nm. This resulted in the formation of the bowtie nanoantenna array. Without any oxygen plasma processing, the gaps between the nanotriangles were found to be around 200 nm. Hennemaan et. al used NSL to create a range of Ag triangles by varying the diameter of PS spheres from 200-1500 nm and the Au film thickness from 40 to 200 nm[146]. They found that only with certain combination of sphere sizes and film thickness could flat triangles be obtained. They determined that a majority of their triangles had an edge length that was approximately 80% of a sixth of the circumference of their spheres.

One of the key advantages with fabricating nanotriangles using NSL is that the aspect ratio can simply be tuned by either changing the size of nanospheres or controlling the evaporated metal thickness on the surface. Studies have shown that for nanospheres with diameters of 628 nm, 356 nm, 456 nm, and 77 nm, perpendicular bisector lengths for the triangles of 180 nm, 109 nm, 135 nm, and 288 nm have been achieved. As the bisector length increases, the aspect ratio also increases linearly. Similarly, with higher metal thickness, the aspect ratio decreases proportionally. The relationship between the perpendicular bisector of the triangular particle and the interparticle spacing, d_{ip}, to the diameter of the nanosphere can be related by the following two equations[147]:

$$a = \frac{3}{2}(\sqrt{3} - 1 - \frac{1}{\sqrt{3}})D$$
$$d_{ip} = \frac{1}{\sqrt{3}}D \quad (2.4)$$

According to this equation, starting with 400 nm diameter spheres would result in approximately 100 nm for the perpendicular bisector length. Morarescu et. al investigated the effect of changing the aspect ratio on the optical properties of the Au triangles [148]. They

calculated that increasing the aspect ratio of the structures resulted in a red-shift of their plasmon resonance from the near-infrared to infrared wavelengths. They also showed that the sharpness of the tips of the triangles were affected by changing the colloidal sphere's diameter. Tabatabaei et. al showed that by depositing thicker layers of Au that were about half the diameter of a particle resulted in the formation of tetrahedral pyramids[149]. However, in this study they showed that the tip sharpness was not the dominant factor for enhancement of the electric. They attributed field enhancements to be more dependent on the proximity of the pyramid edges. Thus, these studies demonstrate that the enhancement of the electric field is a combination of the sharpness of the tip and also the spacing between the nanotriangles.

2.3.4.1 Nanotriangles on shrink film

In this section, a versatile technique to fabricate an array of nanotriangle structures is described. By integrating the advantages of nanosphere lithography to generate a hexagonal closed pack array of PS beads onto a heat shrink SMP, polyolefin film (PO) and the ability to shrink to different degrees, tunability with the structures is shown. Oxygen plasma etch is used as an independent parameter to vary the size of the Au triangles and gaps within the triangles. This is accomplished as shown in the process illustrated in Figure 2.14.

Experimental

Heat shrink PO films were cleaned in isopropyl alcohol and then dried with pressurized air. The clean PO film was then corona treated for 35 s to increase the hydrophilic nature and change the surface energy of the PO surfaces. A solution of 500 nm carboxylate polystyrene (PS-COOH) beads (Bangs lab) was diluted to a 1:1 ratio with triton X-100 and methanol (1:400 by volume). Approximately 12 µL of this solution was then spin coated onto the PO film for 5 minutes at 1200 RPM and allowed to dry for four hours up to overnight. After spin coating, the substrate

with the PS-COOH beads was plasma etched at a power of 20 W in an oxygen plasma asher for a range of time intervals from 0-95 seconds (s). The substrates were then coated with 4 nm Cr and 40 nm Au by electron beam vapor deposition. To prevent shrinkage of the substrates, the temperatures did not exceed past 40° C during the metal deposition. Following the metal deposition, samples were sonicated in ethanol for two minutes followed by sonication in millipore water to remove the PS-COOH beads. The samples were left to air dry overnight. The substrates were then mounted with double-sided tape onto a glass slide and placed in a convection oven. The substrates were heated from room temperature (23^{o}C) to different temperatures ranging from 90 °C to 155 °C. As the substrate started to shrink during the heating process, the percent changes in length from the original size were recorded with a digital caliper. The ratio of the final width of the substrate relative to the initial width was used to calculate the percent change in length. During the metal deposition process, the temperatures did not exceed past 40° C in order to avoid shrinkage to the substrate. An atomic force microscope (AFM) (Asylum Research MFP-3D AFM) with silicon cantilevers (Olympus) was used to characterize the resulting topography of our substrate, and a scanning electron microscope (SEM) (FEI-Magellan 400 XHR), at ~ 2 kv, was used to image the surface topology of the structures.

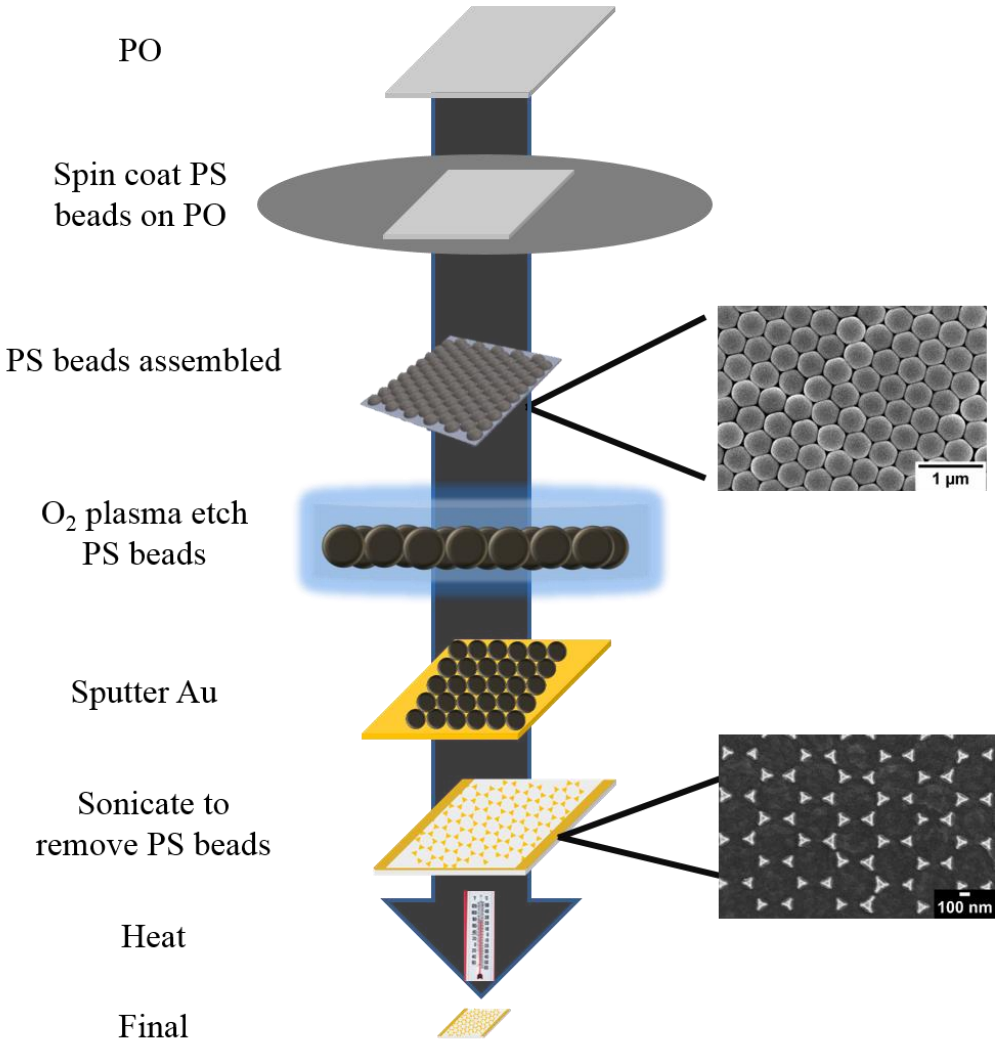

Figure 2.14 Schematic process flow for fabrication of Au nanotriangle arrays.

Characterization

Figure 2.15 presents the SEM images of the Au nanotriangles etched for various time intervals of (a) 0 s, (b) 30 s, (c) 45 s, and (d) 90 s. The height of the triangles measured from the apex to the base were observed to get smaller with longer etch times and an increase in the gaps between the triangular particles also was noted. This is counter intuitive to what was expected because etching for longer times should have yielded triangular particles that were larger in size along

with an increase in the gaps. These preliminary results suggested two possible options that could yield such results. In the first option, when the beads are self-assembled into a monolayer, the beads are not actually touching and there is slight gaps between them. However, during the etching process, the PS beads get closer to each other and the sides of the beads are mainly getting etched. The other possibility is that the beads are not uniformly etched and so the sides of the bead are etched while the corners of beads are etched at a slower rate.

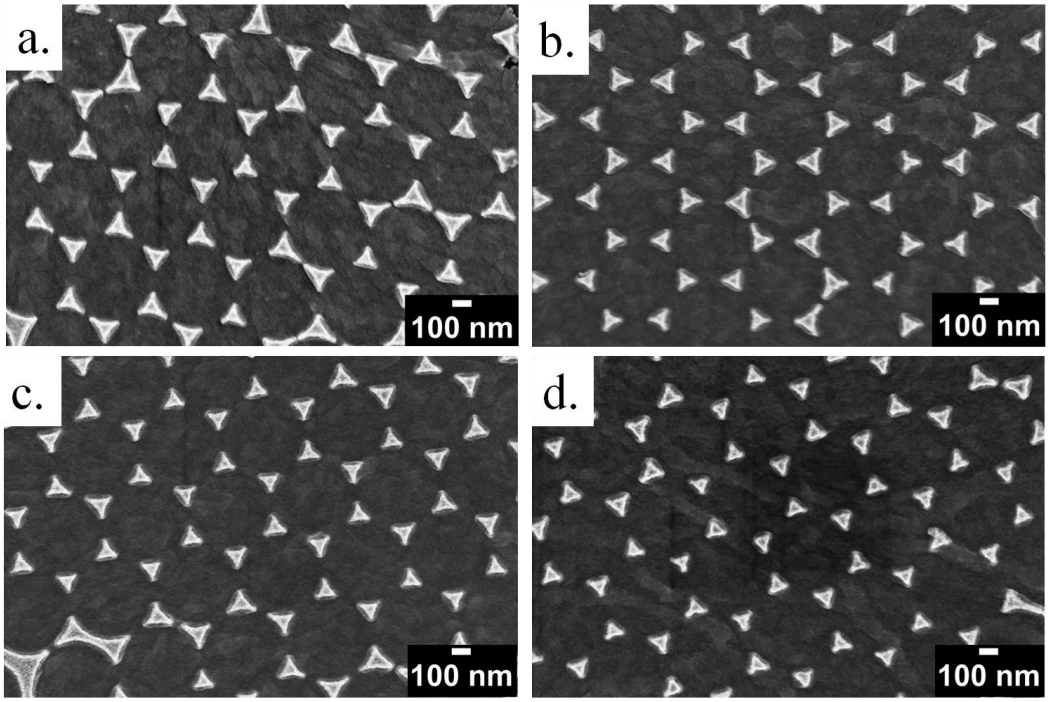

Figure 2.15 SEM images of Au nanotriangles created using various plasma etch times: a. 0 s, b. 30 s, c. 45 s, d. 60 s.

Figure 2.16 presents the SEM images of the 30 s etched Au nanotriangles shrunk to different degrees in length (a) 0%, (b) 25%, (c) 40%, and (d) 77 percent in length. As expected, the gaps between the Au triangular particles were observed to get smaller as the heat shrink SMP was shrunk. However, shrinking past 35 percent, the triangular particles were also noted to have their

features masked by wrinkles that also formed due to the stiffness mismatch of the heat shrink SMP with other stiff skin layers introduced during the oxygen plasma step. It was initially thought that the additional stiff skin layer was added when oxygen plasma was used to etch the colloidal particles. However, preliminary results with shrinking the colloidal particles that had not been etched with oxygen plasma also yielded wrinkles. Thus, it is speculated that the additional stiff skin layer was deposited during potentially the E-beam evaporation process.

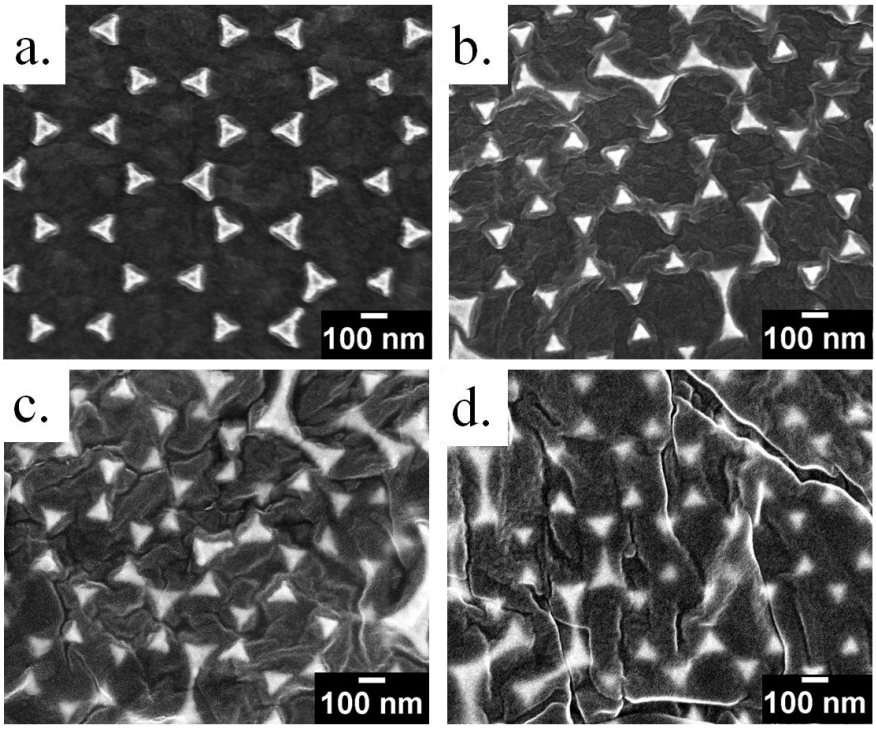

Figure 2.16 SEM images of 30 s etched Au nanotriangles shrunk to different degrees in length (a). 0%, (b). 25%, (c) 50%, and (d) full-77%.

2.4 Summary

In this chapter, we used commodity shrink wrap film as a platform and combined with top-down and bottom-up approaches to create scalable methods for synthesis of tunable metallic structures.

A simple approach to pattern metal films onto the shrink wrap film was shown and by leveraging the stiffness mismatch of the metals with the shrink wrap during the shrinkage, nano to microscale metallic structures were created. By varying the thickness of metal deposited on the shrink film, we were able to tune the morphology of our structures and gaps between them. We also described methods to self-assemble colloidal particles onto the shrink wrap film to form an array of periodic structures. We etched the particles to various sizes and leveraged the shrinkage of the shrink wrap to control the gaps between the etched particles. For this dissertation, the work was mainly focused on using simple top and down approaches to create scalable structures. However, methods such as EBL and FIB should also be explored to determine their feasibility of being combined with the shrink film technology to create tunable structures for future plasmonic applications.

Chapter 3 Surface Plasmons

3.1 Optical Properties of Metal

A bulk metal is composed of a collection of single metal atoms that each have a free electron or quasi-free electron, which have the ability to move freely when an external electrical field is applied[150]. The mobility of the electrons to move freely in a metal is what affects the metal's thermal conductivity, electrical conductivity, and optical reflectivity. The free electrons in the metal behave like a gas of free charge carriers, similar to plasma that can undergo a collective oscillation of plasmon waves when the frequency of the electric field is correct. In order for the metal to be useable for plasmonics, the real part of the dielectric function has to be negative which is satisfied when the plasmon frequency of the material is higher than the frequency of the incident light[151]. The plasmon frequency is high since the metals have a high density of free electrons. In addition, the imaginary part of the metal's dielectric has to be low because it corresponds to dielectric losses experienced when the metal is polarized [152, 153]. Different metal have different plasmonic responses, but the metals suited as a good candidates for plasmonic applications due to their inherent plasma frequency are gold (Au), silver (Ag), copper (Cu), and aluminum (Al)[153]. Of these metals, Au and Ag have been extensively used for plasmonic applications because they have low losses and possess unique optical properties due to their LSP resonance (LSPR) in the visible and near infrared region, a frequency range that is suitable for most lasers[154].

The Drude-Sommerfield model often has been considered a classical model that can be used to describe the permittivity of metals[155]. In the Drude-Sommerfield model of a metal, a gas of

free electrons and a rigid ionic lattice are considered. The equation of motion for the free-electron gas is noted by equation 3.1.

$$m^* \frac{d^2\bar{r}}{d^2t} + m^* \gamma \frac{d\bar{r}}{dt} = -e\bar{E}_o \exp(-i\omega t) \quad (3.1)$$

In this equation m* is the effective mass of free electrons, γ is damping coefficient that describes electron scattering, -e is charge of electron, ω is the angular frequency of exciting radiation, and $E_o^{e(-i\omega t)}$ is external driving field. If one assumes that electron position is $r(t) = r_o e^{-i\omega t}$, the above equation can be simplified to equation 3.2.

$$-\omega^2 m^* \vec{r} + -i\omega m^* \gamma \vec{r} = -e\bar{E}_o \quad (3.2)$$

The macroscopic polarization of the metal can be determined to be:

$$\vec{P} = -\frac{ne^2}{m^*(\omega^2 + i\gamma\omega)}\bar{E}_o \quad (3.3)$$

Where n is the density of electrons in equation 3.3. From the polarization, the dispersive permittivity can be obtained and written as equation 3.4.

$$\varepsilon_{Drude}(\omega) = 1 - \frac{\omega_p^{\ 2}}{\omega^2 + i\gamma\omega} \quad (3.4)$$

Where ω_p is the plasma frequency and is defined as the following:

$$\omega_p = \sqrt{\frac{ne^2}{m^*\varepsilon_o}} \quad (3.5)$$

The dielectric constant can be divided into the real and imaginary parts according to equation 3.6.

$$\varepsilon_{Drude}(\omega) = 1 - \frac{{\omega_p}^2}{\omega^2 + i\gamma\omega} + i\frac{\gamma{\omega_p}^2}{\omega(\omega^2 + \gamma^2)} \qquad (3.6)$$

As presented in equation 3.4, when the frequency, ω, is significantly smaller than ω_p, the second term becomes larger than 1 and hence, the real part of the dielectric constant would negative. This typically occurs in the visible and near-infrared wavelengths. The dielectric constant can be related to the refractive index of the material, η, by the square root of the dielectric constant as indicated in equation 3.7.

$$\eta = \sqrt{\varepsilon} \qquad (3.7)$$

Thus substituting equation 3.7 into equation 3.4 yields that η^2 is equal to equation 3.4. When ω is less than ω_p, η is a complex number. The dielectric constant is also a complex number that has a real and imaginary part. In this complex number, the real part contributes to polarization and the imaginary part contributes to the dissipation of the energy in the metal. As a result of the dielectric constant being negative, the light has a small penetration depth into the metal and some the light is reflected[156].

While the Drude-Sommerfeld model works well with lower frequencies such as near infrared, infrared and some of longer visible wavelengths, the model fails at the higher frequencies or lower visible wavelengths[157]. This is because the Drude-Sommerfeld model assumes the metal only has free electrons and ignores any possible bound electrons. However, for Au, the imaginary part of the dielectric constant is observed to increase significantly for wavelengths shorter than 550 nm because of the interband transitions[157]. The interband transitions that occur due to the excitation of bound electrons to conduction electrons are

responsible for this. To account for the effect of bound electrons, the Lorentz-Drude model has been developed which is given by equation 3.8[158].

$$m^* \frac{d^2\bar{r}}{dt^2} + m\gamma \frac{d\bar{r}}{dt} + \alpha\bar{r} = e\bar{E}_o e^{(-i\omega t)} \qquad (3.8)$$

Where m is the effective mass of bound electron, γ is damping coefficient, α is spring constant of the bound electron. With the addition of bound electrons to dielectric constant

$$\varepsilon_{Lorentz}(\omega) = \frac{\Omega^2{}_p}{(\omega_o{}^2 - \omega^2) - i\gamma\omega} \qquad (3.9)$$

Where

$$\Omega_p = \sqrt{ne^2/(m\varepsilon_o)} \qquad (3.10)$$

(n is number of bound electrons per unit volume), ω_o is natural frequency of bound electrons $(\omega_o = \sqrt{a/m})$. Then the dielectric function from Lorentz-Drude can be re-written as a new form that incorporates the Drude dielectric function and Lorentz.

3.1.1 Optical properties of composite structures

After surface characterization of the composite structures, the optical properties were investigated. Post-shrinkage, the composite structures are very opaque and as a result of this, there is minimal light passing through. Thus, despite extensive efforts to measure the transmission properties of the composite structures with a UV-vis spectrophotometer, the result could not be measured accurately. Preliminary transmission spectra results collected from 450-900 nm results did suggest that potentially there were characteristic dips located around 560, 690, 790 nm which were not present in the flat metal controls or in the solution. The characteristic dips could potentially be related to surface plasmonic effects, but with very low

transmission readings this cannot be concluded. Since, the slit size for the beam of light is typically around 1 mm, an average spectra of all the optical properties of the composite structures within 1 mm would be measured. This is not ideal because the composite structures are heterogeneous in size, so the plasmon resonance would not be a single peak. However, with a laser beam, the spot size can be smaller than the beam size for a UV-vis spectrophotometer. The two-photon excitation spectra of the composite structures was investigated by exciting every 5 nm from 745-900 nm. The laser power at each wavelength was measured and was revealed to be the strongest at 800 nm. In order to keep the laser power same at each wavelength, a factor was applied to each of the laser powers at each of the wavelengths. This factor was measured by dividing the laser power at a specific wavelength of interest with the maximum laser power. Then the factor was squared since two-photon is a non-linear process. The correction factor was multiplied to each of the fluorescence intensities obtained for the composite structures at the each of the excitation wavelengths. The excitation spectra is shown in Figure 3.1(a) and reveals that a peak around 780-790 nm occurs for the composite structures. This indicates that the composite structures are possibly able to scatter more light between these wavelengths. We speculate that this possibility would overlap well with the plasmon resonance band of the composite structures if the extinction spectra could have been recorded as has been previously suggested by other studies[159]. Gold nanoparticles and nanorods have recently shown to have interesting two-photon photoluminescence properties when excited at their resonance wavelength [159, 160]. It was determined that the two-photon luminescence was sensitive to the local electric field enhancement on nanoscale, rough metal films[161]. To perform these studies, emission spectrum of the Au particles are collected at the resonant wavelength. The emission spectrum in Figure 3.1(b) suggests that the emission spectrum in select areas on the composite structures is from

500-650 nm and is very broad. The broadness of the emission spectrum can be attributed to the heterogeneity within the structures. The emission spectrum was observed to vary from region to region, but in general had a broad emission from 500-650 nm. The emission spectrum of the control which was just the Ni structures without the Au did not exhibit similar emission spectrum characteristics. We hypothesize from these results when exciting the composite structures with two-photon, the best excitation wavelength would be to choose between 780-790 nm and to choose fluorescent molecules whose two photon excitation cross section is within 15 nm from the plasmon absorption peak of the Au structures. Furthermore, from the emission data, we speculate that selecting dyes that emit between 500-650 nm would be optimal for maximum emission intensity.

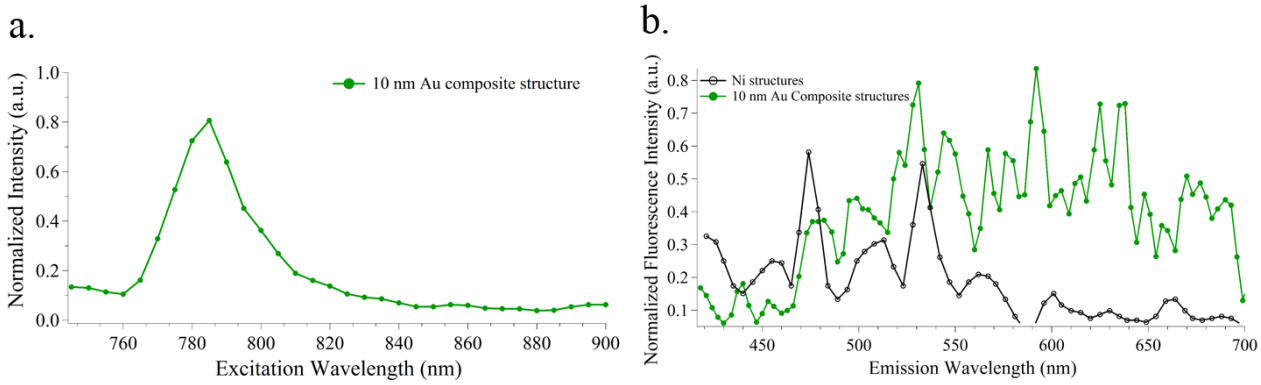

Figure 3.1. (a) Excitation spectra from 740-900 nm of 10 nm Au composite structures (b) Emission spectra of 10 nm Au composite structures.

3.1.2 Optical properties of Au nanotriangles

The optical properties of the Au nanotriangles were also investigated by reflectance spectroscopy. The reflectance spectra for the Au nanotriangles is presented in Figure 3.2. The reflectance of the unshrunk triangular particles was recorded to be broad and peak around 790-810 nm. With a partial shrinkage of 25% in length, the triangular particles were noted to blue-

shift to have a lower reflectance occurring between 750-770 nm. Further shrinkage revealed that as the triangular particles approached closer to each other, the particles blue-shifted and peaked around 730-750 nm. Finally with full shrinkage of the substrates, the reflectance dropped further down and revealed to have a very broad spectra. The decreases observed in the reflectance of the substrates was anticipated because as the PO film shrinks, the substrate becomes more opaque.

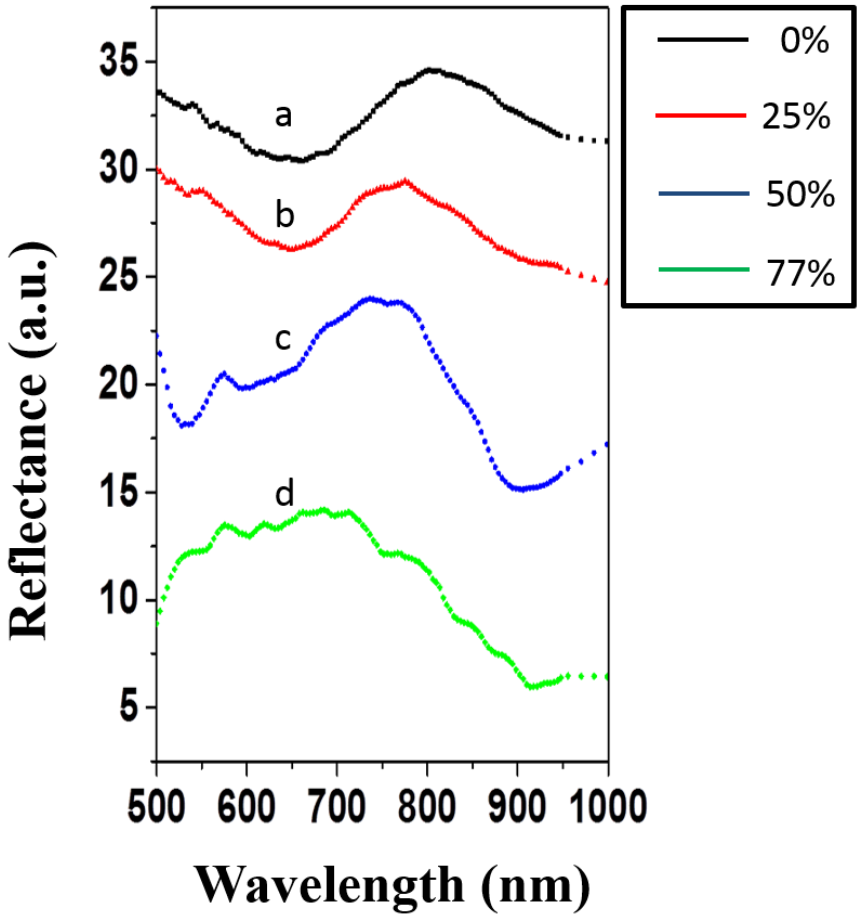

Figure 3.2. Reflectance spectra of 30 s etched Au nanotriangles shrunk to different degrees (a) 0%, b. 25%, c. 50%, d. 77% in length.

3.2 Surface plasmons

When light interacts with a metallic surface, the collective excitation of the free valence electrons close to the surface of the metal is called a surface plasmon (SP) [162]. This effect was first discovered by Robert W. Wood in 1897 who observed irregular light distribution from metallic diffraction gratings [163]. In 1902, he also noted that energy was lost as heat when the SPs propagated along the metal surface. Fifty years later, Ritchie introduced the idea that on a metallic surface, the excited electrons had the possibility of coherent fluctuating into what are referred as SP oscillations. The existence of these SPs would later be confirmed by experiments by Powell and Swan in 1960 and improved by Otto, Kretschmann and Raether. Fano also developed a theory to explain Woods observations by coupling light into electromagnetic (EM) surface waves aided by metallic surface gratings. Two types of SPs exist: propagating (PSPs) and localized (LSPs)[164]. When the electrons oscillate to create surface plasmons at the surface of the metal, an electron wave is generated. This electron wave has interactions with a photon from light and electrons in the metal. This electron wave starts to accumulate electrons in an area and this leads to other areas having less electrons and as a result, become positively charged. The electron wave keeps propagating along the metal and dielectric interface until it decays. PSPs or SP polaritons proceed in the x-y direction along a flat smooth metal-dielectric interface, decaying exponentially away from the surface. These PSPs are also capable of transforming the incident light's energy into a surface wave, and the incident angle is critical for the excitation and emission. LSPs occur when the incident laser light interacts with nanostructures and results in the conduction electrons to collectively oscillate to generate dipole fields [165]. A redistribution of the electric field intensities around the metal nanostructures may occur when the incoming electric field interacts with the dipolar fields. A positive charge is left behind when the electrons

are displaced and the positive charge tries to pull back the electrons to their original positions by exerting an attractive force on the electrons. The coulomb interaction between the electrons and metallic nuclei cause the plasmons to oscillate collectively. When the plasmons oscillate and move coherently at a resonant frequency, the incident electromagnetic (EM) field is significantly amplified; this results in an increased local EM at the surface of the nanostructures [166]. A molecule in close proximity to the metal nanostructures can feel the significantly increased electromagnetic (EM) fields generated at the surface of the nanostructures and have an increased induced dipole. Several factors affect the magnitude of the EM enhancement such as the metal, geometry of the structures, roughness, frequency of the incident light, and properties of the fluorophore.

3.3 Brief theory behind electromagnetic field enhancement

The conventional description of EM field enhancement is based on the classical Mie scattering theory that was theoretically described by Mie in 1908 for spherical nanoparticles [167]. In his theory he was able to explain the red color of gold nanoparticles cause by absorption and scattering of the light by solving Maxwell's equations. He solved Maxwell equations for a small sphere that interacted with electromagnetic light wave and was surrounded by a dielectric medium using the dielectric constant of the bulk metal. When spherical nanoparticles were excited with an EM field, the nanoparticles produced an intense absorption attributed to plasmon resonance. Mie's theory also has some assumptions that the particles and their surrounding environment are homogeneous and can be described by bulk dielectric properties[168]. At the same time, the Mie theory is a better model for spherical particles that are significantly smaller than the wavelength of light. With this taken into account, the light's electric field can be assumed to be constant. This is often referred to as the quasi-static

assumption. Solving Maxwell's equations led to a relationship for the extinction cross section of metallic nanospheres. The Mie theory starts by applying Maxwell equations (3.4.1-3.4.4) [167].

$$\nabla \bullet E = 0 \qquad (3.4.1)$$

$$\nabla \bullet H = 0 \qquad (3.4.2)$$

$$\nabla XE = i\omega\mu H \qquad (3.4.3)$$

$$\nabla XH = -i\omega\varepsilon E \qquad (3.4.4)$$

where E is the electric field, H is the magnetic field, ω is the angular frequency, μ is the permeability, and ε is the permittivity (dielectric constant). The optical properties of a sphere can be calculated by using Maxwell's equations. When an electric field, E_o, is applied to a spherical particle, the electric field inside the particle is given by equation 3.4.5[168].

$$E_1 = -E_o \frac{3\varepsilon_2}{\varepsilon_1 + 2\varepsilon_2} \qquad (3.4.5)$$

In this equation, ε_2 is the dielectric constant of the surrounding medium and ε_1 is the dielectric constant of metal. Equation 3.4.6 presents a complex expression for the dielectric constant of the metal that can be applied

$$\varepsilon(\omega) = \varepsilon'(\omega) + i\,\varepsilon''(\omega) \quad (3.4.6)$$

where ε' and ε'' are the real and imaginary part of the dielectric function of the metallic nanoparticles[167]. When the electromagnetic field interacts with the spherical nanoparticle, the charges of the free conduction electrons become polarized and this polarization relation can be expressed in equation 3.4.7.

$$\alpha(\omega) = 4\pi\varepsilon_o a^3 \frac{\varepsilon_1(\omega) - \varepsilon_2}{\varepsilon_1(\omega) + 2\varepsilon_2} \qquad (3.4.7)$$

Polarizability is a measure of how easily electrons can be moved in response to an electric field [169]. Equation 3.4.5 can also be written in terms of when a molecule is in close proximity to the spherical particles[170]. The dipolar field, E_{sp}, that spherical particle produces is represented in equation 3.4.8. The magnitude of the field felt by a nearby molecule depends on the radius of the sphere r, distance d from molecule, metal's dielectric constant ε, and the incident field strength, E_o .

$$E_{sp} = r^3 \frac{\varepsilon - \varepsilon_o}{\varepsilon + 2\varepsilon_o} (\frac{1}{r+d})^3 E_o \quad (3.4.8)$$

Here ε is the real dielectric constant of the metal structure and ε_o is the dielectric constant of the environment. A molecule in close proximity to the metal nanostructures feels an enhanced EM which is the sum of the electric field from the incident light and the dipolar field generated within the particle (E_o+E_{sp}). As shown in equation 3.4.8, the maximum enhancement occurs when the denominator of the first term approaches infinity, satisfied when ε = - 2εo [167]. Furthermore, the field enhancement decays with r^{-3}.

The extinction cross section which is the power removed from the incident beam due to the particle can be calculated by taking the sum of the scattering and absorption cross sections.

$$\sigma_{ext} = \sigma_{abs} + \sigma_{sca} \quad (3.4.7)$$

Where σ_{ext}, σ_{abs}, σ_{sca} are the extinction, absorption, and scattering cross section. The physical cross section of a sphere with radius *a* is noted as πa^2. For particles significantly smaller than the wavelength of the light, the σ_{sca} is negligible and only the σ_{abs} is significant. The mean free path of the free electrons in the metal is around 50 nm and since the particles are relatively small,

scattering is generally inefficient. However, as the particle size increases, the σ_{sca} becomes dominant relative to σ_{abs} because larger particles have higher probability to scatter more light.

The scattering cross section can be related to the power and can be calculated after determining the scattered fields.

$$\sigma_{sca} = \frac{P_{scat}}{I_o} = \frac{k^4}{6\pi\varepsilon_o^{\,2}}\left|\alpha(\omega)\right|^2 \qquad (3.4.8)$$

Where I_o is power density of incident light and $\alpha(\omega)$ is the polarizability of the sphere presented earlier in 3.4.5.

The dissipated power by the sphere can be applied to calculate the absorption cross section

$$\sigma_{abs} = \frac{P_{abs}}{I_o} = \frac{k}{\varepsilon_o}\mathrm{Im}\left[\alpha(\omega)\right] \qquad (3.4.9)$$

[169]. In the Mie theory, vector spherical harmonics of the scattered field can be expressed in a series of multipole expansion, where the first term is a dipole mode, second is quadrupole mode, fourth is octupole mode and so on[171]. For particle sizes smaller than 50 nm, only dipolar modes are able to be excited by light at optical frequencies. However, particle sizes larger than 50 nm, quadrupole and higher resonance mode contributions also appear. At these sizes, the dynamic depolarization and radiation damping occur[172]. Dynamic depolarization occurs when not all the conduction electrons are able to be excited in phase because the electric field oscillates as a function on position, leading to a reduction in the depolarization at the center of the particle. As a result of this, there is a red-shift in the particles resonance. The ability of AuNPs to convert incident radiation into absorption and scattering components is quantified by measuring the cross

sections and the sum of this represent extinction. The extinction cross section of the sphere is greater than the physical cross section of the sphere when $-\varepsilon_1$ approaches to $2\varepsilon_2$.

Thus far, a simple model has been considered to understand the scattering and absorption properties for small spherical nanoparticle. However, in reality most of the particles are not spherical and have other geometrical shapes that can also be modeled. According to the Mie theory, the extinction spectrum, $E(\lambda)$ of an arbitrary shaped nanoparticle is described by Equation 3.4.21 [173]:

$$E(\lambda) = \frac{24\pi^2 N r^3 \varepsilon_o^{3/2}}{\lambda \ln(10)} \left[\frac{\varepsilon_i(\lambda)}{(\varepsilon_r(\lambda) + \chi\varepsilon_o)^2 + \varepsilon_i(\lambda)^2} \right] \qquad (3.4.21)$$

The Mie theory is based on the assumption that the nanoparticles are spherical and homogeneous, but the surface plasmon oscillation in metallic nanoparticles deviates from this theory as the particles become non-spherical. In order to account for these deviations from spherical particles, the χ value is defined as the shape factor. For spherical particles, χ is two but for particles can be as high as 20[173]. Other theoretical models such as the Gans modification of the Mie theory, discrete dipole approximation (DDA), T-matrix method, and Finite difference time domain (FDTD) describe that a shift in the surface plasmon resonance occurs when the size or shape of the nanoparticle deviates from spherical geometry[174, 175]. The DDA approximation calculates the extinction cross section for particles by dividing it into polarizable cubes and assuming that the elements are small enough that they only dipole interactions with incident electric field. In the FDTD method, the electromagnetic field distribution is calculated within an individual unit cell array. As a result, recent work has been focused on understanding the optical properties of nonspherical nanoparticles such as rods, disks, cubes, and prisms [176-

181]. In these circumstances, the localized surface plasmon resonance (LSPR) is split into multiple other plasmon modes, dipole, quadropole , and octupole plasmon resonance[182].

Chapter 4 Fluorescence and Approaches for Enhanced Detection

4.1. Principles of fluorescence

In 1852, British scientist George Gabriel Stokes reported and coined the term fluorescence[183]. In his experiment, Stokes observed that when ultraviolet light was shined on a tube of quinine sulfate, a bright blue light was emitted. Furthermore, he also noted a shift in the emission and absorption wavelength where the fluorescence emission always occurred at a longer wavelength than the excitation light. This shift in the emission and absorption is also referred to as the Stoke's Shift. In the early 19^{th} century, investigations showed that samples such as minerals, resins, crystals, chlorophyll, and inorganic compounds fluoresced when U.V. light was shined on them. It was not until the 1930s when fluorochromes were used as staining probes to identify components in tissues, pathogens, and bacteria for biological investigations[184].

Fluorescence occurs when a fluorescent molecule absorbs light photons at one wavelength and emits at a longer wavelength. Fluorescent molecules are typically composed of polyaromatic hydrocarbons or heterocycles and have large conjugated π electron systems[185]. Unexcited fluorescent molecules have electrons in the ground state and after excitation by incident light from the U.V. visible spectrum, the electron transitions from the ground to excited state. The electronic states of a molecule and its transition between those states are often graphically depicted using a Jablonski diagram to illustrate the processes. The y-axis is a graph of energy which increases from the bottom, ground state, to the top, excited state. Figure 4.1 presents the Jablonski diagram that illustrates the processes involved in creation of an excited electronic singlet state by absorption of a photon of light and the subsequent emission of fluorescence. In step 1, a photon of light is absorbed a specific wavelength and the electrons from the fluorophore are raised from the ground state (S_o) to a higher electronic energy level

(S1'). This absorption process is very fast and generally occurs within femtoseconds, 10^{-15} seconds. In the second step, the electron relaxes from the highest vibrational state to the lowest electronic excited state by internal conversion processes such as vibrational or rotational. Vibrational relaxation is the process where the electron gives away the energy in vibrational mode in the form of kinetic energy and returns to the lowest electronic excited state. The vibrational relaxation process occurs typically due to collisions between molecules and occurs with picoseconds, 10^{-12}, seconds between vibrational levels. Once, the electron has reached the lowest electronic excited state, the electron decays back to the ground state by either radiative and/or non-radiative processes. This could occur by either by heat or quenching which are both non-radiative or as depicted in step 3, the emission of a photon of light which is radiative. Since some of the initial energy within the molecule is lost through heat or vibration during the internal conversion process, the emitted energy is generally less than the excitation energy. This difference in the emitted energy from the excited energy is also referred to as the Stoke's shift.

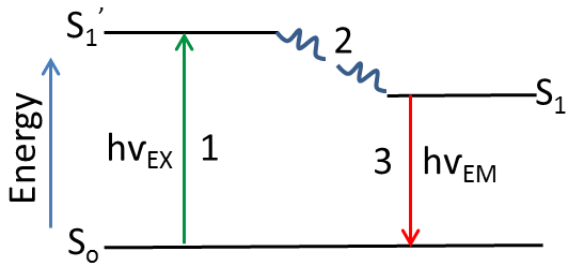

Figure 4.1 Jablonski energy diagram for a fluorophore excited in free space (no metals) [186]

The emission of a photon of light to return the electron back to the ground state occurs in a longer time domain within the range of nanoseconds and is also known as the fluorescence lifetime. A fluorescent molecule is characterized by its quantum yield Q_o, which is defined as the

ratio of photons emitted to photons absorbed and lifetime, τ_o. Q_o, and τ_o are defined in equation 4.1.1.

$$Q_o = \frac{\Gamma}{\Gamma + k_{nr}} \quad (4.1.1)$$

$$\tau_o = \frac{1}{\Gamma + k_{nr}} \quad (4.1.2)$$

In these equations, Γ is the radiative decay rate or the fluorescence decay rate and k_{nr} is the rate of non-radiative decay. [186]. The k_{nr} is affected by the interactions between the fluorophores and local environment such as collisional quenching, molecular associations, and energy transfer. The maximum possible value for Q_o that a molecule can have is 1.00. τ_o for a species is dependent on the surroundings and is affected by factors such as pH, temperature, polarity, viscosity, and binding. τ_o in particular, can be reduced by quenching, a process caused from collisions within the transient state excited interactions.

Fluorescence lifetime measurements can be collected in the time or frequency domain depending on the type of microscope used. The time and frequency domain utilize the fluorescence decay law that is based on first order kinetics. In the fluorescence decay law, if populations of molecules are instantaneously excited when the photons are absorbed, then the fluorescence intensity as a function of time, I(t), decays slowly to the ground state. This equation to express this intensity decay relation is presented in 4.1.3 and I(t) is the intensity at time t, α is a pre-exponential factor, and τ is the lifetime[187].

.

$$I(t) = \alpha e^{-\frac{t}{\tau}} \qquad (4.1.3)$$

In the time domain, a time-correlated single photon counting is applied to measure the exponential decay and a pulsed excitation source is required [188]. A short pulse of light excites the sample and the emission is recorded as a function of time. In the frequency domain, a modulated source of laser light is used to excite the sample. The fluorescence emitted from the sample has a similar waveform to the modulated light, but is modulated and phase shifted from the incident excitation laser light. The modulation (M) and phase φ are calculated from measuring the decrease in the amplitude of the modulated light and distance between the excitation light and emitted light. The phasor is described by its modulation (M) and phase φ. In the frequency domain, the φ and m are described by:

$$\vartheta(\tau_\theta) = \tan^{-1}(\omega t) \quad (4.1.4)$$

$$m(\tau_M) = \frac{1}{\sqrt{1+\omega^2\tau^2}} \quad (4.1.5)$$

Where $\omega = 2\pi f$ is the angular frequency of the modulated excitation light and τ is the lifetime, f is the generator-set frequency [189]. The excitation of light is defined as the following:

$$E(t) = E_o + E_\omega \cos(\omega t + \varphi_E) \quad (4.1.6)$$

Where ω is the frequency of excitation modulation and E_o and E_ω are the DC (long time average of fluorescence signal) and AC (amplitude of oscillation) of the excitation. The phase of the excitation light is known and denoted as φ_E. The excitation light's modulation of depth is defined as E_ω/E_o. From equations 4.1.4 and 4.1.5., two different lifetimes, τ_θ and τ_M can be calculated. If the lifetimes τ_θ and τ_M are equal to each other, then the fluorescence lifetime is single

exponential. When the lifetimes are not equal to each other, then the fluorescence lifetime is multi-exponential. In order to measure multiple lifetimes, measurements of phase and modulation have to be performed at multiple frequencies.

The phasor analysis can be applied to examine and visualize the lifetime distribution of the species. In this method, at each pixel, the lifetime data is converted into a coordinate pair which is called a phasor and a histogram of number of pixels with these phasor coordinates is called phasor plot. To identify the regions of an image that correspond to lifetime values, SIM FCS has been applied. Each of the phasor coordinates is written as s and g coordinates which is calculated using rapid intensity normalized cosine and sine of the histogram as presented in equations 4.1.7 and 4.1.8[190].

$$g = \frac{1}{N} \sum_{p=0}^{n_p - 1} \cos(2\pi p / n_p) H(p) \quad (4.1.7)$$

$$s = \frac{1}{N} \sum_{p=0}^{n_p - 1} \sin(2\pi p / n_p) H(p) \quad (4.1.8)$$

In these equations, N is the total number of photons and n_p is the number of bins in phase histogram. The phase, φ, and modulation, m, can be related to the s and g coordinates by the following vector transformation equations:

$$\phi = \tan^{-1}\left(\frac{s}{g}\right) \qquad (4.1.8)$$

$$m = \sqrt{g^2 + s^2} \qquad (4.1.9)$$

Each of the s and g coordinates can then be treated as a vector referred to as a phasor and plotted on a two-dimensional histogram plot to yield a phasor plot. From the phasor plot, all single exponential lifetimes are located on the universal circle and is shown as a semicircle around g is 0.5 where lifetime values are given as:

$$\tau = \frac{s}{2\pi f g} \qquad (4.1.10)$$

If the lifetime falls within the universal circle, then the molecular species have a complex decay and are attributed to multi-exponential lifetime which can be modeled using higher Fourier harmonics[191]. Furthermore, if there are two molecular species present that have single exponential lifetime decay, then a normalized linear combination of component phasors fall within the universal circle. Depending on which species is predominant out of the two will affect where the lifetime lies on the line.

4.2 One-photon versus two-photon excitation

The environment that the fluorophore is placed in has a strong influence on the fluorescence lifetime and intensity. The fluorescent molecule can be excited by two different methods: one photon or two-photon. In one photon excitation, a fluorescent molecule is excited using a visible laser by a single photon of a particular energy from the ground state to an excited state [192]. From the excited state, the molecule will emit a photon at a higher wavelength to relax back to the ground state. In two-photon excitation, a laser excites the sample by using the near simultaneous absorption of two lower energy near-infrared photons that each contains half the energy[192]. From the excited state, the fluorophore relaxes by vibrational process to the lowest

energy state and then similar to one-photon excitation, emits a photon of light in the visible wavelength before relaxing back to the ground state (Figure 4.2).

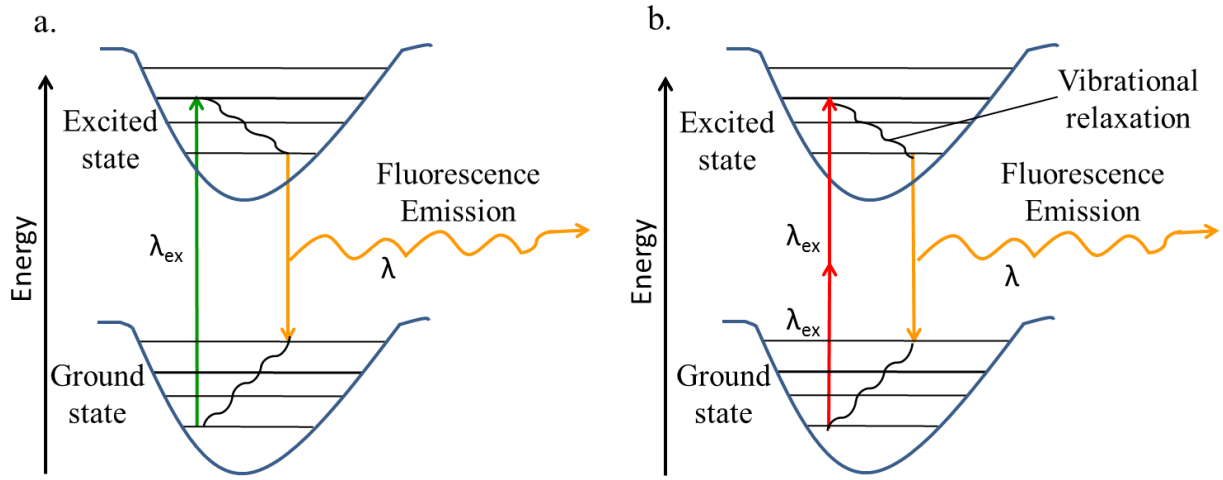

Figure 4.2. Jablonski diagram for (A) one-photon and (B) two-photon excitation of a fluorophore[193].

The two-photon absorption process is a second order process and has a much smaller cross section around 10^{-50} (cm^4s/photon) than the one photon absorption process which is around 10^{-16} cm^4s/photon [194]. This means that with conventional lasers, the probability of two-photon excitation with light is significantly smaller than with one-photon excitation. Thus, for two-photon excitation a highly focused single pulsed laser is used to deliver a high flux of photons through the objective. Another important aspect of two-photon excitation microscopy is that a high numerical aperture objective is required to finely focus the excitation source to a diffraction-limited spot. The number of photons absorbed per fluorophore per pulse can be calculated using equation 4.2.1[194].

$$n_a = \frac{{p_o}^2 \delta}{\tau_p {f_p}^2} \left(\frac{(NA)^2}{2hc\lambda} \right)^2 \qquad (4.2.1)$$

Where τ_p is the pulse duration, δ is the fluorophore's two-photon absorption at a wavelength, λ, p_o is average incident laser intensity, f_p is the laser's repetition rate, NA is the numerical aperture, h is the Planck's constant, and c is speed of light. From the above equation, it can be shown that for a fixed laser power and repetition frequency, the probability of excitation increases significantly with an increased NA for the objective or with a reduction in the pulse width of the laser[195]. Also as the NA is increased, the excitation power is locally restricted further to smaller focal volume. Typically, to achieve such a high photon flux, a femtosecond titanium-sapphire (Ti-sapphire) system is required for generating a 100-fs pulse at a repetition rate of 80 or 100 MHz[195].

In 1931, Maria Goerppert Mayer established the theoretical groundwork for two-photon excitation and investigated the theoretical impact of two-photon absorption by atoms [196, 197]. With the introduction of the laser in the 1960s, these assumptions were confirmed experimentally by Werner Kaiser and I.C Garrett for the first time in 1961 [198]. However, it was not until the development of mode-locked lasers in 1990 when W. Webb, W. Denk, and J. Strickler created a two-photon laser scanning microscope that biological applications became to fruition. Using 2-photon laser scanning microscopy, they were able to show that photobleaching of the fluorophores was restricted to the focal plane and also that three-dimensional studies could be performed [199]. Furthermore, due to the nonlinear nature of the two-photon excitation, the fluorescence emission increased quadratically.

The advantages of using two-photon excitation versus one-photon is that there is reduced photodamage, less scattering losses, and a deeper penetration into the specimen[192, 200]. The scattering losses that occur from the attenuation of the incident light are less in the near-infrared wavelengths regime because the scattering cross section decreases. Furthermore, the emission

pinhole aperture reduces the out-of-focus fluorescence light which leads to a higher collection efficiency of the fluorescence signal yielding a larger intensity in the signal. Since the excitation volume is limited to the sub-femtoliter regime, there is an improvement in the stability of the fluorophore. Furthermore, since the excitation is only achieved around the focal plane where laser light is concentrated, there is little biological specimen damage to the regions above and below the focal plane that are not being imaged. The non-linear dependence of the fluorophore excitation on the laser light intensity restricts the photon absorption to a narrow region at the focal plane where the photon flux is the highest [201]. The differences in the excitation volumes using one-photon excitation or two-photon excitation are illustrated in Figure 4.3.

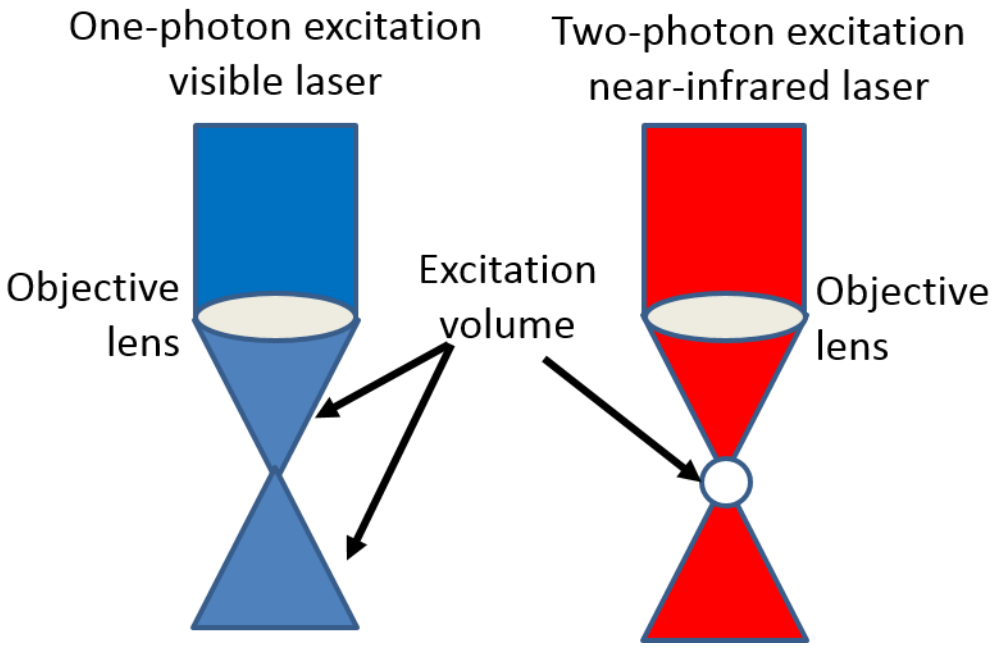

Figure 4.3. A comparison of excitation profiles with laser of one photon (left) and two photon (right). [202]

The absorption rates for one and two-photon excitation are calculated as:

$$\text{One-photon excitation (OPE): } k_{12} = \sigma_{OPE}\theta \qquad (4.2.2)$$

Two-photon excitation (TPE): $k_{12} = \frac{\sigma_{TPE}}{2}\theta^2$ (4.2.3)

Where σ is the absorption cross section (cm^2 and cm^2/s) and Θ is intensity of the excitation light (photons/cm^2s)[202]. From these, one can see that a linear relationship is expected for the fluorescence signal with one-photon excitation while a quadratic increase is expected with two-photon excitation.

4.3. Principles of metal enhanced fluorescence (MEF)

MEF is an effect that yields increases in the fluorescence signal when fluorophores are placed nanometric distances from a metallic surface. MEF is characterized by an enhancement in the emission signal, quantum yield, photo stability, and a decrease in the fluorescence lifetime of fluorophores[203]. The pioneering work of Purcell started the notion that lifetime of an excited atomic state is dependent on a combination of its properties and also its surrounding environment[204]. This was then proven experimentally in the late 1960s with Chance et. al and Drexhage et. al's studies [205]. Drexhage et. al observed that when a fluorescent molecule was placed within sub-wavelength distance to a reflective metallic film, a distribution of enhancements in the fluorescence signal and changes in the emissive lifetime were observed. In their studies, an europium complex was positioned at varying distances from a planar silver surface by creating a multilayer sandwich using the Langmuir-Blodgett technique. It was noted that the distance the fluorophore was place away from the surface affected the fluorescence lifetime. As the fluorophore was placed certain distances away from the metal surface, the fluorescence lifetime oscillated and close to the surface (below 10 nm), the fluorescence lifetime was strongly quenched. The quenching of the fluorescence lifetime was explained due to nonradiative transfer of energy from the fluorophore to the metal. A follow-up study by

DeMartini et. al noted that the fluorescence lifetime of the europium complex shortened in a microcavity composed of a dielectric mirror[206]. Suzuki and Yokoyama also followed similar experiments on an organic dye but did not observe significant changes in the lifetime values[207]. Thus far, these initial ground work studies mainly looked at how the fluorescence lifetime changes as the fluorophore was placed different distances from the metal surface, but did not investigate in depth the enhancements. Following these initial studies, Lackowicz and Geddes showed in 2002 that when the fluorophore was placed in close proximity to metallic structures, enhanced emissions in the fluorescence signal were also observed that complemented with the fluorescence lifetime changes[208]. They coined the term metal enhanced fluorescence for this phenomenon. Their work demonstrated that when the fluorophore was positioned at nanometeric scale distances from the metallic structures and the absorption/emission bands of the fluorophore overlapped with the plasmonic resonance of the metallic structure, enhancements were seen. Through these investigations, it was thought that the fluorophores can interact with the metal through three possible mechanisms.

In the first, the interaction of the field from the incident light at a specific frequency with the free electrons on the metal surface localizes the incident electromagnetic (EM) field around the vicinity of the metal nanostructures. In the second, the near-field interaction of the dipole moment of the fluorophore couples with the metal surface to generate spatial oscillations of the electron density referred to as localized surface plasmon resonance (LSPR). In the third mechanism, this LSP field can modify the radiative decay rate of the fluorophore by altering the photonic density of states. The photonic density of states is defined as the number of electromagnetic modes allowed per frequency unit. In short, the LSP field can increase the excitation field and the radiative emission rate of the fluorophore. A fluorophore in the near-field

(within tens of nanometers) can have a significantly enhanced radiative emission rate and shortened lifetime. A shortening in the inherent lifetime of the fluorophore increases its photostability [209]. However, if the fluorophore at distances less than 5 nm away with the metallic surface, the molecular dipole of the fluorophore can directly and non-radiatively transfer its energy to the metal surface, such that the signal is quenched [210]. The optical properties and enhanced localized electromagnetic fields of these metallic nanostructures are strongly dependent on the composition, size, shape, and dielectric properties of the substrate and medium above the surface [211]. Early studies indicated that nanoscale confinement of the EM field within sub-wavelength volumes could enhance the field strength by several orders of magnitude relative to the incident light [212-214]. Furthermore, metallic nanostructures with sharp corners or tips could further enhance the local electric field [215, 216].

As mentioned previously, the environment that the fluorophore is surrounded in has an effect on both the lifetime and intensity. As shown in equation 4 and 5, the Q_o and τ are thought to be affected by both the non-radiative and radiative decay rate. When fluorophores are placed in nanometric distances from metallic surfaces, the Q_o and τ, additional terms are added to account for these theoretical contributions due to the metallic surfaces.

$$Q_m = \frac{\Gamma + \Gamma_m}{\Gamma + k_{nr} + \Gamma_{nr} + \Gamma_m} \quad (4.3.1)$$

$$\tau_m = \frac{1}{\Gamma + k_{nr} + \Gamma_{nr} + \Gamma_m} \quad (4.3.2)$$

Where Q_o and Q are quantum yields due to the fluorophore in free conditions and close to the metallic surface. Under the circumstances where the fluorescence is closed to metallic nanostructures, the incident electric field is amplified significantly generated by the interaction of the light with the surface plasmons (Figure 4.4).

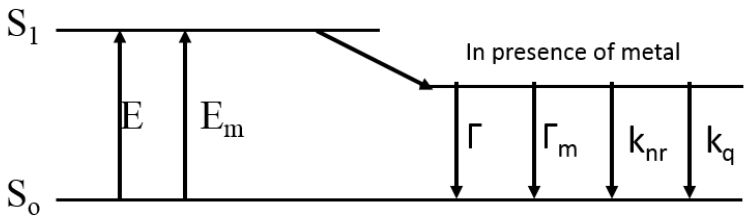

Figure 4.4. Jablonski diagram for a fluorophore excited near metallic surfaces [186]

In this Jablonski diagram, the increase in the radiative decay rate induced by the metal surface is denoted by Γ_m and k_m is the non-radiative decay rate due to the metal. Hence, from the above equation, it can be inferred that an increase in the radiative decay rate caused by the metal will yield an increase in the quantum yield of the fluorophore in the presence of the metal while the lifetime will decrease.

4.4 Techniques to enhance fluorescence detection by metallic structures

The type of metallic surface the flurophore is placed on has an effect on if the fluorescence signal will be enhanced or quenched. When fluorophores are placed in close proximity on flat metal films, strong quenching effects in the fluorescence are mostly observed because the surface plasmons propagate on the thin metal films since they are not able to be effectively trapped. Unlike flat films, roughened metal films which have nanostructures smaller than the wavelength of light (200 nm) can support the ability to trap the surface plasmons. The MEF phenomenon is distant dependent and maximum enhancements for fluorophores have been shown to occur when the fluorophore was place 5-20 nm away from the metallic surfaces. Fluorophores placed within 5 nm away from the metal surface are generally quenched [217-219]. As mentioned early, when the fluorescence is quenched, the energy from the molecular dipole that is excited is transferred to the metal surface. In addition to the distance dependence on the enhancement in the

fluorescence intensity, the localized electromagnetic field enhancements around these metallic nanostructures are strongly wavelength dependent. Thus, the spectral overlap between the dye and the LSPR modes of the metallic nanostructures also plays a role in the enhancements. The incident electric field enhancements that surround metal nanostructures[220]. Thus, along with the correct placement of the fluorophore on the metal nanostructures, studies have shown that the spectral properties of the fluorophore and LSPR properties of the nanostructured surface should be somewhat similar.

While fluorescence is a very sensitive technique, its detection limit is dependent on the quantum yield of the fluorophore, photostability of the fluorophores, and autofluorescence of the background. Investigations in how to utilize MEF for surface assays has led recently to several applications focused on studying interaction of fluorophores with nanostructured metal surfaces[219, 221, 222]. Parfenov et. al created silver fractal structures to which they adsorbed 10 μM fluorescein (FITC) bound to human serum albumin (HSA) and observed a 100 fold increase relative to glass[223]. HSA served as a spacer to position the FITC the appropriate distance away from the silver fractals. Mateeva et. al and Lukomska et. al observed that with Ag island films and monolayers of silver colloids, the emission signal could be increased an additional 5-15 fold with enhancements up to 300 fold at the hot spots [224, 225]. Sorenson et al showed that for Ag colloids on Au films, enhancements on average of 50 fold could be observed with almost a 200 fold enhancement at the hot spots. Zhang et. al generated a silver film by vapor deposition to create a fluoroimmunoassay that was used to investigate how the SiO_2 thickness and metal thickness affected the MEF enhancements [226]. In their study, they studied both how the SiO_2 and Ag film thicknesses affected the enhancements in the fluorescence signal. The SiO_2 layer acted as a spacer to position the fluorophores conjugated to anti-IgG different

distances from the Ag film. Interestingly, both factors, the Ag film thickness and SiO_2 film thickness were important to obtain enhancements in the fluorescence signal. On a thin thickness of 2 nm of Ag, the fluorescence signal was quenched, but as the film thickness increased, the enhancement in the fluorescence signal increased. They attributed this to the fact that at thin thicknesses, Ag particles deposited on the surface were individual nanoparticles. Since at this small regime, absorption dominates over scattering, they thought that the small metal particles quenched the fluorescence. As they increased the Ag film thickness, the particles coalesced and became larger so that the scattering component dominated and could enhance the fluorescence signal. An additional enhancement in the signal was then provided by depositing a thin layer of SiO_2 onto the metallic surface. SiO_2 thicknesses below and above 10 nm provided less enhancement relative to when 10 nm SiO_2 was deposited on the surface. Since the IgG molecule has a theoretical height of 10 nm, the additional 10 nm height from the SiO_2 was considered to be efficient enough for obtaining enhancements. Zhang et. al used thermal vapor deposition to deposit copper, another noble metal, onto silanized glass slides that enhanced the fluorescence signal of their dye by 3 times[227]. Similar to their previous study with Ag, they noted that the fluorescence signal was best enhanced when copper was composed of continuous metal particles relative to continuous films where the fluorescence signal became quenched. Xie et. al used Au nanoparticles that had a shell layer of silver on the surface and deposited them onto a glass slide pre-functionalized with (3-aminopropyl)-trimethoxysilane (APTMS) [228]. By varying the time immersed in the silver enhancer solution and concentration of the Au colloid solution, the size of the nanoparticles could be tuned and Au nanoparticle layers with different interparticle distances were observed. FITC-HSA was incubated overnight on the surfaces to bind the proteins to Au-Ag nanoparticles and enhancements were compared to fluorescence intensity observed on glass.

They determined that their fluorescence enhancements were dependent primarily on the size of the particles and observed the largest enhancement when the Au-Ag nanoparticles were left for 3 min in the silver enhancer solution. Furthermore, they also examined how the size of pure Au nanoparticles with no Ag shell affected the emission intensities. Similar to Zhang's study, they found that as the size of the Au nanoparticles increased, the emission increased. The fluorescence lifetime was also observed to shorten in the presence of the Au colloids. Goldys et. al. created silver fractal like structures and non-covalently bound HSA-FITC to the surfaces [229]. They observed that the highest enhancements in the fluorescence signal were observed for regions that occupied small fractions of structural areas. These structural areas when examined under an environmental scanning electron microscope (ESEM) were composed of fractals made of loose arrangements of silver nanowires. They also observed that the fluorescence lifetime in thin regions were shorter than in regions where the Ag layer was dense. Fu et. al presented a novel method to fabricate metal wrinkles of nano to submicron size by sputtering Au onto a pre-stressed polystyrene sheet. Controlling the thickness of the Au deposited on the polystyrene sheets tuned the size of the wrinkles [230]. Dye molecules were dissolved in a polymer solution and spin coated on the Au wrinkles to place the dye molecules a distance away from the metallic surfaces. A 7-fold fluorescence enhancement of the dye on the Au wrinkles was observed relative to glass. Szmacinski et. al fabricated a multilayer glass slide substrate composed of a Ag mirror, SiO_2 layer, and Ag nanoparticles[231]. The surfaces of the multilayer substrates were coated with a layer of biotinylated bovine serum albumin (b-BSA) and immobilized with a streptavidin dye. In the visible wavelengths, enhancements in the fluorescence signal up to 31 fold were demonstrated. Bek et. al placed a 40 nm fluorescent PS bead between two 60 nm AuNPs (gold nanoparticles) spaced and utilized AFM to mechanically push the AuNPs towards

each other [232]. When the fluorescent PS bead was placed less than 90 nm apart from one of the AuNPs, the fluorescence increased by 150% and bringing the second AuNP closer to the fluorescent bead increased the fluorescence by 270%.

These studies showed that the magnitude of enhancement in the fluorescence signal is dependent upon several factors such as size of the structures, plasmon resonance of the structures, and the distance the fluorophores were placed away from these metallic surfaces.

4.5 One-photon excitation of rhodamine B on composite structures

Previous studies have demonstrated that a strong overlap between the surface plasmon resonance band of the metallic structures and the excitation/emission spectra of fluorophore has been crucial to obtain effective fluorescence enhancements[231]. Thus, based on preliminary transmission spectra measurements where a dip was observed around 555 nm, rhodamine B that has an absorption and emission peak that spectrally overlaps around 555 nm was selected. To prevent quenching of the fluorophore due to the close proximity of the fluorophore to the metal structures (5 nm Ni/10 nm Au), 5 nm SiO_2 was sputtered on the bimetallic islands formed after heating to yield composite structures. For controls, 15 nm SiO_2, 15 nm Au, and 15 nm Ni were sputtered on the shrink film and heated to generate similar structures to the composite structures. Also, 5 nm Ni/10 nm Au were sputtered on a glass slide to yield a bimetallic glass slide that was then heated and sputtered with 5 nm SiO_2 to yield a composite glass slide. Two main possibilities for enhancing the fluorescence signal were investigated through these studies. First, the ability of the roughened surfaces to enhance the fluorescence signal was considered by not sputtering the thin spacer layer of 5 nm SiO_2, post heating onto the controls. Second, the ability of the fluorescence signal to get enhanced through the scattering of light by the SiO_2 structures was studied by measuring the enhanced fluorescence signal with the 15 nm SiO_2 structures. A

confocal laser scanning microscope (LSM) with a 545 +/- 15 nm laser excitation was used to image the substrates and an emission filter of 575-650 nm was used to collect the fluorescence. A 40X objective (numerical aperture, N.A=0.75) and 25 µm X 25 µm laser scan area was selected for imaging purposes. Less than 1.0 µW laser power was chosen to excite the samples. A 200 nM solution of rhodamine B was added to the top of the substrates and then imaged.

Figure 4.5.1 I-III presents the fluorescence images, line plot profile, and histogram profile, respectively, for the 200 nM rhodamine B on the composite structures, composite glass slide, and the controls. In general, the fluorescence signals of the rhodamine B molecules on the controls: glass, composite glass slide, Au structures, and Ni structures exhibited fluorescence intensities which were similar to each other. The average fluorescence signal of the rhodamine B molecules on the substrates is measured by taking the integrated intensity using the region of interest (ROI) analysis in Image J. The true fluorescence signal was calculated by taking the ROI of the fluorescence signal of rhodamine B on the substrates minus the background fluorescence signal on the substrates when they are in HPLC water. The ROI area is kept the same over the images and all values are compared to the true fluorescence signal on glass. A 15-17 times enhanced signal of the rhodamine B molecules on the SiO_2 structures relative to glass is observed. Interestingly, though, more than a 150 times enhanced fluorescence signal of the rhodamine B molecules relative to glass was revealed to occur in select areas on the composite structures. While the fluorescence signal of the rhodamine B molecules on the SiO_2 structures also exhibited an enhanced signal, the intensity was uniform throughout the structured areas unlike the composite structures where the bright spot was confined to very small regions. While, the composite glass slide did not show any appreciable enhancements in the fluorescence signal of rhodamine B, AFM analysis of the surface indicated that the surface was similar to a

continuous film (Figure 2.6). Figure 4.51-II shows an intensity profile of the rhodamine B molecules on the substrates as a function of position. The 25 μm line is drawn horizontally across the brightest spot in each of the images to determine the size in diameter of the hot spots. The diameter of the bright signals in the hot spot was measured to be less than 450 nm, which defined by Rayleigh criterion is at the spatial resolution limit of the microscope. According to physics and optics, the theoretical diffraction limited spatial resolution is defined according to equation 2.2, presented previously in Chapter 2. The laser's excitation wavelength, λ_{exc} = 561 nm, and the NA of the microscope objective was 0.75, so the spatial resolution limit of the microscope was calculated to be around 450 nm.

To determine the overall distribution of the fluorescence signal per pixel generated by the composite structures relative to the other substrate, a histogram was plotted (Figure 4.5.1-III). Fluorescence values that were at least 10 times higher than the background noise was selected as the threshold for what was considered bright intensity. The background noise was calculated by measuring the fluorescence signal of the substrates with HPLC water. For the composite structures, fluorescence values higher than 300 were considered to be bright intensities. In general, the frequency of brighter intensities per pixel relative to the controls were observed for rhodamine B molecules on the composite structures. Rhodamine B molecules on the SiO_2 structures had the second frequency of bright intensities per pixel; while the glass had the lowest intensity per pixel. The glass slide, composite glass slide, Ni and Au structures, all had similar maximum fluorescence intensities.

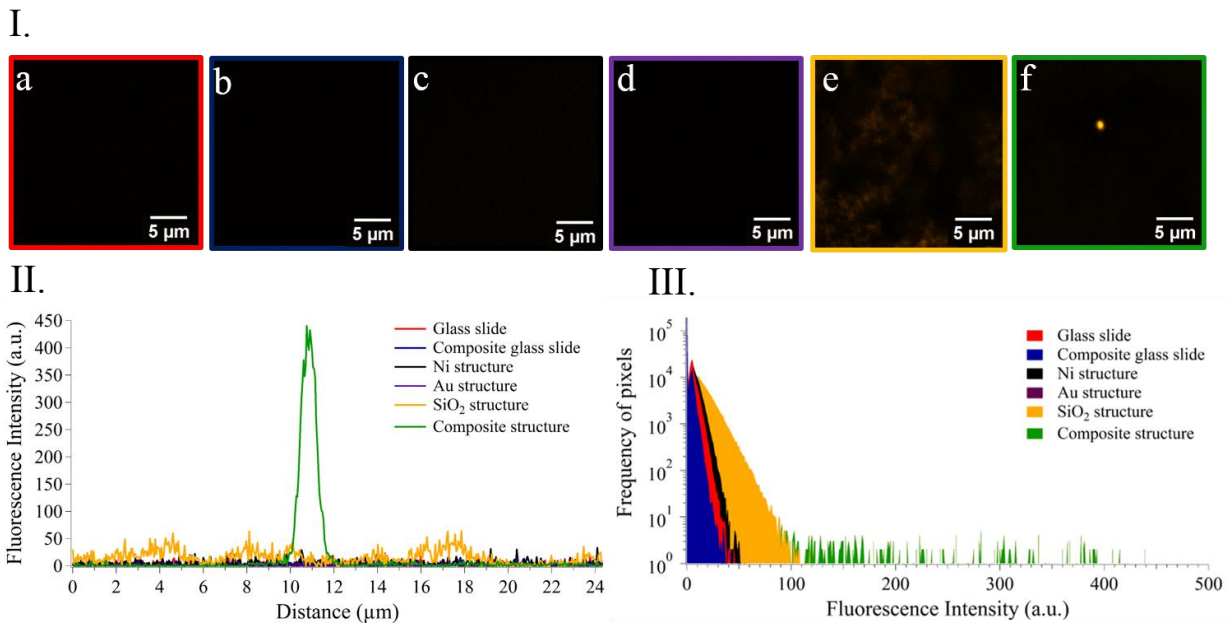

Figure 4.5 Fluorescence images for 200 nM rhodamine B excited from 530-560 nm at excitation power of 1.0 µW on (a) glass (b) composite glass slide (c) SiO_2 structures (d) Ni structures (e) Au structures (f) composite structures. II Line plot profile of 25 µm line drawn through brightest region III. Histogram distribution for rhodamine B on the corresponding substrates.

The enhanced signals observed on the surfaces are specific to rhodamine B, as confirmed by the emission spectrum of the fluorescence signal (Figure 4.6). Emission spectrum were collected using a Zeiss confocal laser scanning microscope (LSM 710) with a 561 nm argon laser for excitation and an emission filter of 415 – 710 nm with a 40X (W) objective (NA = 1.20, Zeiss Korr C-Apochromat). Figure 4.6 illustrates that the emission peak for rhodamine B on the composite structures occurred at 575 nm. The emission peak of rhodamine B in solution occurred at 578 nm which was also observed on the composite glass slide, Ni, Au, and SiO_2 structures. Thus, a slight blue shift of 3 nm for the peak position of the emission signal was recorded to occur on the composite structures. This slight blue shift of 3 nm can be attributed to the change in the molecular environment of the dye and possibly the strong localized electromagnetic field observed by the fluorophore[233]. Similar, to the plot and histogram

profiles, the trend for the brightest emission observed on the composite structures, followed by the SiO_2 structures was similar.

The composite glass slide has an almost 4 times increase in the emission signal of rhodamine B which is possible since studies have shown metallic glass slides with a thin dielectric spacer can enhance the fluorescence signal due to LSPR effects[69]. If we look at the effect of roughened surfaces on enhancing the fluorescence signal, we estimate that the roughness from the structures caused an average of 2-4 times increase in the emission signal. This increase in the signal could be attributed to the surface roughness which has shown to increase the fluorescence signal by about 5 fold relative to planar surfaces or possibly more rhodamine B molecules on the structures. The scattering from the SiO_2 structures was observed to enhance the emission signal by about 17-18 times relative to in solution on glass. Thus, we calculate that the actual plasmonic effect with the composite structures might be enhancing the fluorescence signal around 5-6 times. However, for the emission signal measurements, the background signal was not subtracted from the corresponding substrates and thus some of the fluorescence signal on the SiO_2 structures could also be attributed to the background. The ROI analysis that was conducted to measure the noise from the substrates with HPLC water suggested that the fluorescence was minimal for the composite structures, Ni structures, and glass slide.

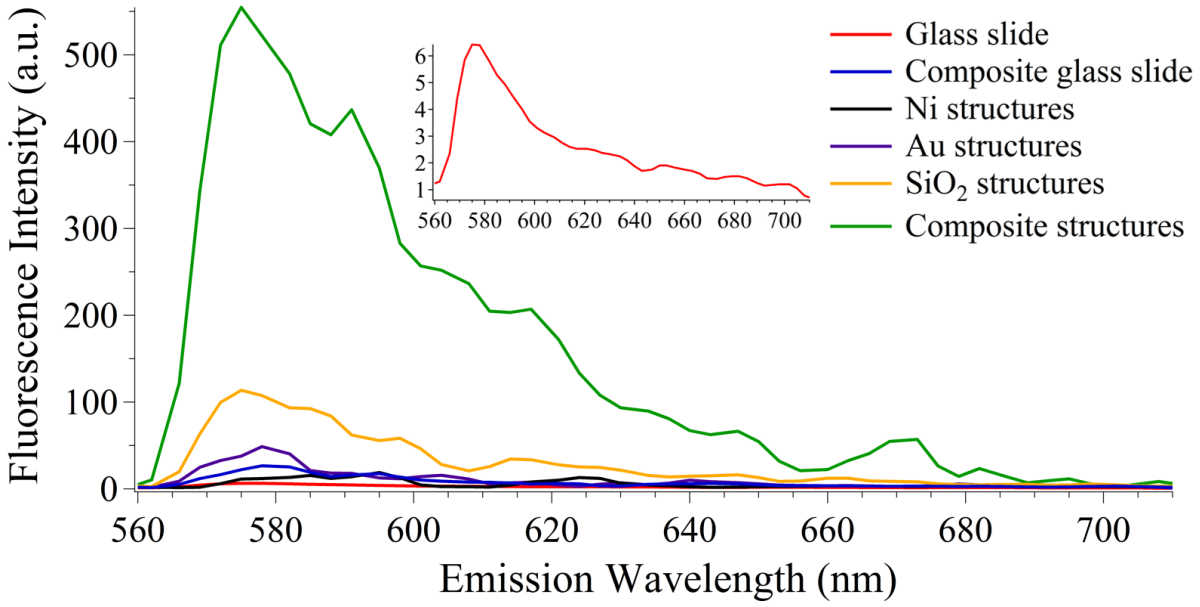

Figure 4.6 Emission spectrum of 200 nM rhodamine B on the substrates.

Thus far, the results indicated that the fluorescence signal of molecules of rhodamine B was the brightest on the composite structures relative to the rest of the substrates. As has been depicted previously by other groups, if a plasmonic effect was related to an increase in the fluorescence signal, then the lifetime of the fluorophore is also expected to be reduced [69, 209]. Simultaneous fluorescence and lifetime characterization was performed using the one-photon confocal (LSM) and a white modulated laser (Fianium). The lifetime decays were collected in frequency domain and analyzed using a SIM FCS program developed at the Laboratory of Fluorescence Dynamics (LFD), University of California, Irvine. Figure 4.7 shows a dramatic decrease of about 80% in the fluorescence lifetime of rhodamine B molecules on the composite structures relative to glass slide. The observed decrease in lifetime could be attributed to the enhancement of local excitation electric fields, leading to an increased excitation rate of fluorophores and radiative decay rate. This significant increase in the radative decay rate could imply an increase in the quantum efficiency of the fluorophore. In order to investigate this

further, however, a calculation of the radiative and non-radiative rate would need to be done. The fluorescence lifetime of the rhodamine B on the SiO_2 structures is shorter by 200 ps than what is on glass. This slight shortening in the fluorescence lifetime could possibly be attributed to concentration quenching effects from the fluorescent molecules in close proximity to each other on the SiO_2 structures or surrounding environmental effects. Interestingly, though, the fluorescence lifetime of the rhodamine B molecules on the Ni, and Au is longer than what it is in solution. This may be due to the fact that fluorescence lifetime of dyes are greatly affected by polarity interactions; since the structured surfaces are relatively hydrophobic, the hydrophobic interactions of the fluorophores with the metallic structures could induce changes in the normal lifetime of the fluorophore[234].

From these experiments, it appears that the enhancement in the signal of rhodamine B molecules composite structures are not entirely due to LSPR effects, because for the large fluorescence increase of 100 times, a significantly shorter lifetime was expected. As alluded to before, though, the large increases in the fluorescence signal could be attributed to two possible factors. First, the SiO_2 on the structures scatters the emitted light from the rhodamine B molecules by around 15-17 times. Then, the fluorescence signal is enhanced additionally by about 5-6 times due to plasmonic effects suggested by the 80% shortening in the fluorescence lifetime relative to the rhodamine B molecules in solution. However, another fact that we must consider is that the fluorescence enhancement in rhodamine B could be related to an aggregation of the rhodamine B dye molecules. There is a possibility that there are more molecules within the bright spots on the composite structures relative to controls which is why the fluorescence signal is significantly brighter.

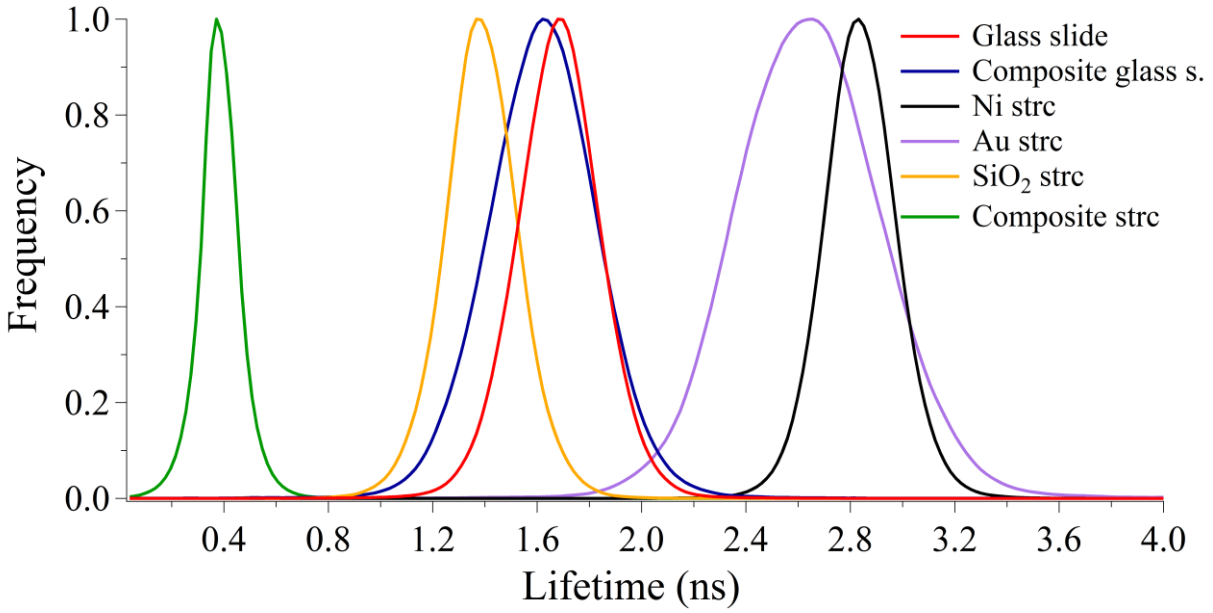

Figure 4.7 Fluorescence lifetime distribution for 200 nM rhodamine B on glass, composite glass slide, Ni structure, Au structure, SiO_2 structure, and composite structure.

4.6 One-photon excitation of IgG-Alexa Fluor 555

Next, to evaluate the antibody detection capabilities of the composite structures, 1 µg/mL (5 nM) goat anti-mouse immunoglobulin (Ig)G labeled with Alexa Fluor 555 (IgG-A555) was tested. IgG was chosen as the model protein because it is one of the most abundant class of immunoglobulin in blood and Alexa Fluor is known to be a relatively photostable fluorophore[235]. 5 nM IgG-A555 was pipetted on top of the composite structures, SiO_2 structures, and glass. For each mole of an antibody, there are approximately 4 molecules of Alexa 555 dye. Figure 4.8 (a-d) shows the fluorescence images and the corresponding emission spectra. Enhancements in the fluorescence signal of up to 250 were observed on the composite structures. We conjecture that the IgG antibody adds an additional 2-6 nm as a spacer to the 5 nm SiO_2, placing the fluorescent molecules at an optimal distance from the metallic structures similar to previously reported work [236, 237]. Previous studies have also demonstrated that a strong overlap between the surface plasmon resonance band of the metallic structures and the

excitation/emission spectra of fluorophore has been crucial to obtain effective fluorescence enhancements. The inset in Figure 4.8(d) also shows an enhanced emission spectrum of the IgG-A555 on the glass slide to compare the emission spectrum obtained from the composite structures to glass. The emission spectrum suggest that they are similar, with the exception that the emission spectrum from the composite structures is significantly enhanced.

Figure 4.8(e) illustrates that the enhanced fluorescence signals of the bright spots on the composite structures also follows a shortening in the fluorescence lifetime. However, for the largest increase in the fluorescence signal of IgG-Alexa-555 on the composite structures, the shortening in the lifetime is not as significant compared to the results with rhodamine B. As was previously shown, the enhanced signal is not purely due to a plasmonic effect, rather a combination of plasmonic and light scattering by the SiO_2 structures. With the rhodamine B results, the fluorescence signal was observed to increase by approximately 15-17 on the SiO_2 structures relative to glass. If this is factored into the 250 increase in the signal, then the enhanced fluorescence signal due to a plasmonic effect would be around 20 times. Although, for a 20 times increase in the fluorescence signal, we would anticipate a significantly shorter fluorescence lifetime; we hypothesize that the since the fluorescent molecules are now fixed to a protein, their rotational motion is restricted which could induce changes in the photo-physical properties of the fluorophore [238, 239]. Similar to the rhodamine B studies, another possibility is that some of the enhanced single is attributed to the aggregation of proteins. Thus, potentially in the enhanced areas there are possibly more labeled antibodies than on the glass slide. In order to understand these enhancements better, it would be important to find methods to be able to determine the number of molecules that are getting enhanced and compare among the surfaces. A method that could potentially be applied to calculate the number of molecules within a fixed

region is using fluctuation correlation spectroscopy (FCS) to determine if any of the molecules within the bright spots have intensities that are fluctuating.

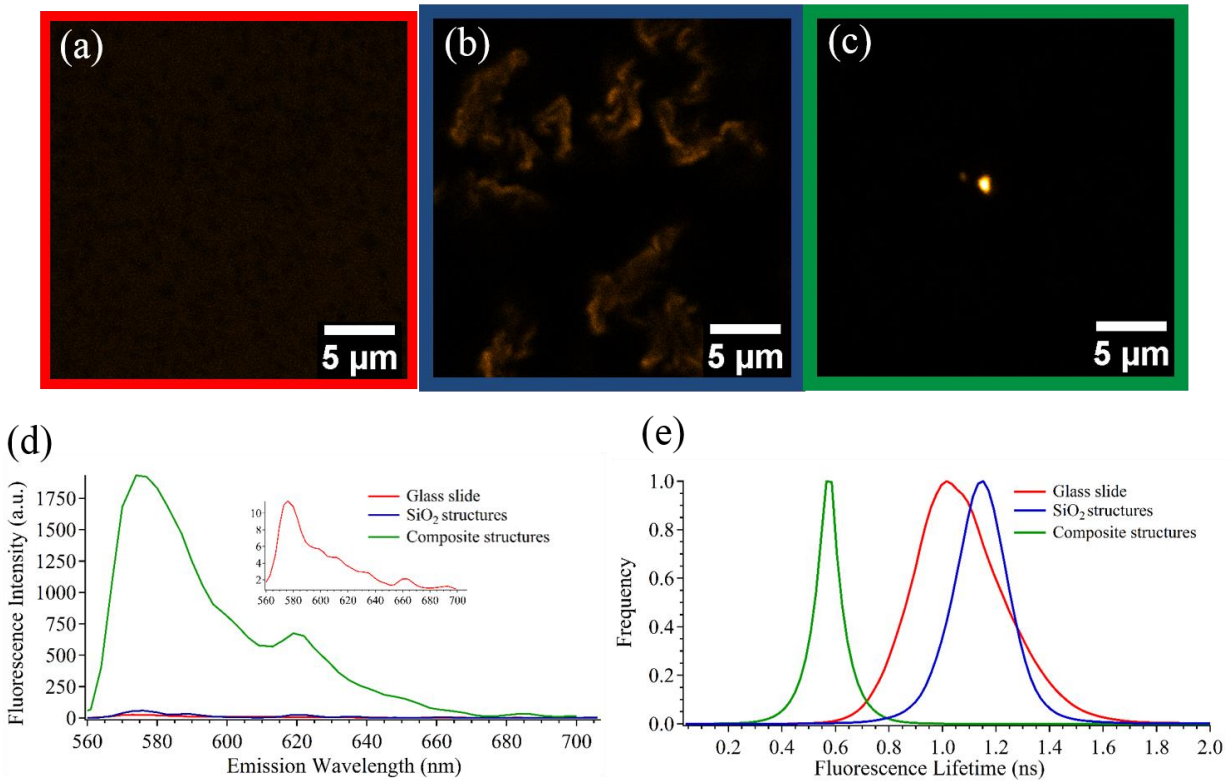

Figure 4.8 Fluorescence images for 5 nM A555-IgG on (a) Glass slide (b) SiO_2 structures (c) Composite structures (d) Emission spectrum of 5 nM A555-IgG on the substrates (e) Lifetime distribution of 5 nM A555-IgG on the substrates.

4.7 One-photon excitation of biotin-streptavidin-TRITC on composite structures

The results presented in section 4.5-4.6 suggested that as a proof of concept, the composite structures could be potentially used as substrates to enhance the emission of dye molecules and labeled antibodies. However, for a functional biosensor, biomolecules such as proteins have to be able to covalently attach to the surface so that during washing steps non-specifically bound proteins are removed from surfaces. Thus, in our next study, we improved our approach by covalently linking biomolecules to our metallic surface. Covalent attachment of the biomolecules to the metal surfaces also enables more control of the number of labeled molecules

attaching to the surface which would enable a better understanding of the enhanced emission signal better. Furthermore, we also examined the dependence of the enhanced signals on the thickness of SiO_2 by depositing 5, 7.5, 15, and 20 nm SiO_2. In the text, from here on out, the metallic substrates with the different thicknesses of SiO_2 will be, in general, referred to as bimetallic islands prior to heating and composite structures, post heating. When discussing about a specific SiO_2 thickness, the amount of SiO_2 deposited will be mentioned. For example a composite structure with 5 nm SiO_2 will be labeled/discussed as 5 nm SiO_2.

A tape mask with an array of 1 mm size holes in diameter was applied to the PO-shrink film and deposited with a thin film of 5 nm Ni, followed by 10 nm Au to yield bimetallic islands. Different SiO_2 deposition thicknesses (5 nm, 10 nm, 15 nm, and 20 nm) were sputtered on top of the masked PO shrink film. After the metal and SiO_2 depositions, the bimetallic islands were oxygen plasma treated and immersed in 2 (v/v)% 3-aminopropyl trimethoxysilane (3-APTMS) to introduce functional amine groups. After rinsing in 100% ethanol, substrates were left to cure overnight. As a model bioassay, we selected a biotin-streptavidin binding system. Streptavidin conjugated to TRITC, a low quantum yield dye (0.1) that excites at 543 nm, was selected to overlap with the previous one-photon studies performed with rhodamine B and Alexa 555. The bimetallic islands and glass slide were covered with 700 µL of 100 µg/mL biotin solution in 1X phosphate buffered saline (pH 7.4). After 1 hour of incubation, the unbound biotin were rinsed with copious amounts of nanopure water. Subsequently, after drying the substrates completely, 3 µL of 10 µg/mL streptavidin conjugated to TRITC was added to the bimetallic islands and left to incubate 1 hour. The substrates were rinsed first with 0.05% Tween-20, followed by rinsing with copious amounts of nanopure water. After substrates were dried completely with air, the adhesive masks were slowly removed and the substrates were exposed to a heat gun (HL 1810S,

Steinel, Bloomington, MN) for less than 5 seconds. To flatten out the pieces, the shrunk substrates were left for 5 minutes in a toaster oven at 160^0C.

The imaging conditions were the same as was applied for the rhodamine B and Alexa 555 studies. Figure 4.9 shows that the average fluorescence signal on the composite structures increased with SiO_2 thickness and were overall brighter than the fluorescence signal observed on the glass slide. In contrast, significantly bright spots were observed on the composite structures with 15 nm SiO_2 relative to glass. The emission spectrum presented in Figure 4.9(g) shows that the signal for the bright spots was also observed to increase with increasing thickness of SiO_2 until reaching a maximum at 15 nm before decreasing. The enhanced signal observed from the composite structures were 35 for 5 nm SiO_2, 200 for 7.5 nm SiO_2, 310 for 15 nm SiO_2, and 40 for 20 nm SiO_2. The increases in the fluorescence intensities was calculated by taking the ratio between the maximum intensities observed at 575 nm, where the dye emitted the strongest, for glass and the composite structures. The increases in the emission observed with 7.5 and 15 nm SiO_2 is consistent with other previous studies where optimal fluorescence signal increases were observed between 5-15 nm and decreased with higher thicknesses [240]. To determine the overall distribution of the fluorescence signal per pixel generated by the composite structures, a histogram was plotted (Figure 4.9f). Similar to the emission spectrum, pixels with higher intensities relative to glass were observed for all the silica thicknesses on the composite structures. The highest intensities were also similarly observed with 15 nm SiO_2 and observed to decrease after 20 nm SiO_2.

We postulate that in the regions where the significantly bright spots were observed were a result of the fluorophores being localized in a region with strong electromagnetic field. We also hypothesize that the decrease in the enhancement signal observed with the covalently linked

fluorophores to the passively adsorbed may be because of the fluorophores random distribution when they are not covalently linked. Thus, in some regions the fluorophores may be an appropriate distance from the metal surface to produce effective enhancements and quenched in others. However, without knowing the number of molecules in the spots that are getting enhanced, it is hard to accurately compare the results. We speculate that covalently linking the fluorophores to the bimetallic surfaces, the fluorophores are more evenly positioned than without covalent linkage.

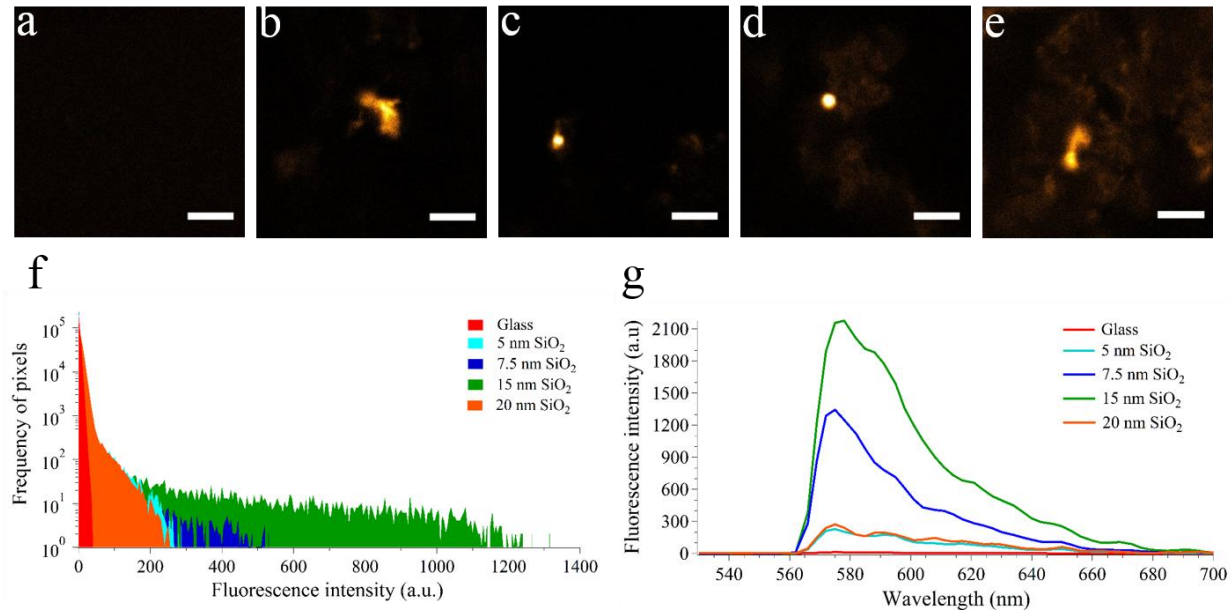

Figure 4.9 Fluorescence, histogram profile and emission spectrum of streptavidin conjugated to TRTIC on (a). Glass slide, (b). Composite structures with 5 nm SiO_2 (c). Composite structures with 7.5 nm SiO_2 (d). Composite structures with 15 nm SiO_2 (e). Composite structures with 20 nm SiO_2 (f). Histogram profile for effect of SiO_2 thickness on enhanced signal (g) Emission spectrum for bright spots. Scale bar is 5 µm.

Arguably, the magnitude of the fluorescence signal could also include a contribution from a larger number of fluorophores on the surface on the bimetallic nanostructures due to an increase in the surface relative to glass. However, if it was purely a concentration effect, we expect that the fluorescence signal should increase at most by 20 fold. As previously reported, the PO film

experiences a 77% reduction in each length upon heating, which results in a theoretical 20-fold consolidation of surface area[83]. We also know from Lin et. al's studies that the SiO_2 structures are able to enhance the fluorescence signal of covalently linked biotin-streptavidin-TRITC molecules by almost 100 times relative to a glass slide[241]. Thus based on these results, we predict that the composite structures further enhance the fluorescence signal by about 3 times due to LSPR effects. To investigate if the increased fluorescence intensities observed were due to a plasmonic effect, lifetime decay were also measured. A confocal laser scanning microscope (LSM) with a 545 +/- 15 nm laser excitation was used to image the substrates and an emission filter of 575-650 nm was used to collect the fluorescence. A 40X objective (numerical aperture, N.A=0.75) and 25 µm X 25 µm laser scan area was selected for imaging purposes. Less than 1.5 µW laser power was chosen to excite the samples. Simultaneous fluorescence and lifetime characterization was performed using the one-photon confocal (LSM) and a white modulated laser. The lifetime decays were collected with a frequency modulated analyzed using a SimFCS program and the lifetime distribution were represented in a phasor plot.

Since the emission spectrum and histogram showed that the brighter signals were observed with the composite structures with 7.5 nm SiO_2 and 15 nm SiO_2, lifetime analysis was performed on these to understand the fluorescence enhancements better. Figure 4.10 (A-G) shows that a dramatic decrease in the fluorescence lifetime of streptavidin-TRITC immobilized on the composite structures with 15 nm SiO_2 was observed relative to glass. Furthermore, similar to the brighter signal seen on the composite structures with 15 nm SiO_2, the lifetime was shortest too. The lifetime mapping also showed that the shortest lifetime was observed at the brightest intensity and slightly radially away from the brightest spot, the lifetimes became longer. This could be a result of the increased excitation field localized at the center. The fluorescence

lifetime in the unenhanced regions on the bimetallic nanostructured islands is less than glass probably because the fluorophores in these regions are oriented in different positions such that the non-radiative decay rate dominates over the intrinsic radiative decay rate.

Thus, the observed decrease in lifetime could be attributed to the enhancement of local excitation electric fields, leading to an increased excitation rate of fluorophores and radiative decay rate. This significant increase in the radiative decay rate could imply an increase in the quantum efficiency of the fluorophore. In order to investigate this further, however, a calculation of the radiative and non-radiative rate would need to be done.

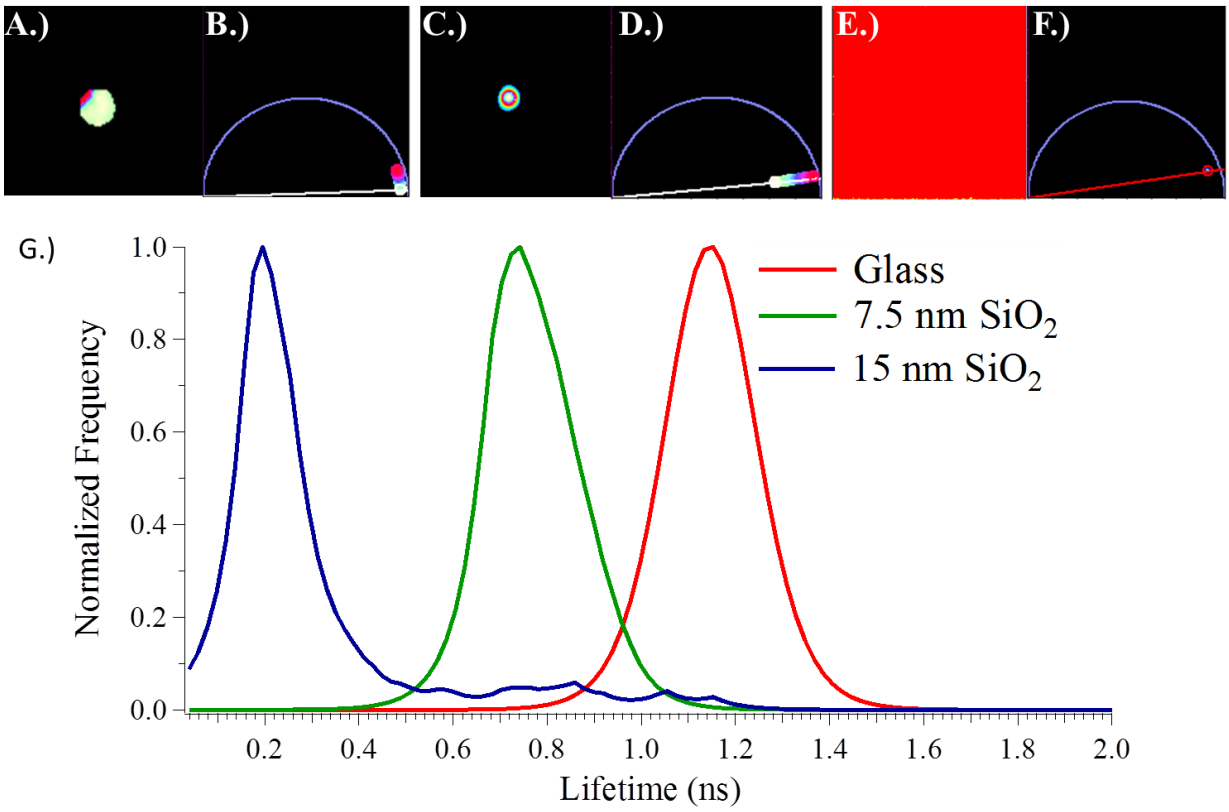

Figure 4.10 Fluorescence lifetime profile for streptavidin conjugated to TRITC on (a,b) FLIM map of the composite structures with 15 nm SiO_2 and corresponding phasor plot histogram (c,d) FLIM map of the composite structures with 7.5 nm SiO_2 and corresponding phasor plot histogram, (e,f) FLIM map of the glass slide and corresponding phasor plot histogram. (g) Summary of lifetime profile for composite structures and glass slide.

4.8 Summary

Our results indicate that the composite structures created are suitable for surface functionalization and enhancing through a combination of scattering and LSPR effects, the emission of the rhodamine B molecules by 100 times and by more than 250 times for IgG conjugated to Alexa Fluor 555 with one photon excitation. We also demonstrate that our metallic surfaces have the capabilities of enhancing the emission signal of bound labeled biomolecules by around 300 times. The fluorescence enhancements observed are thought to occur by a combination of light scattering of the SiO_2 on rough surfaces and plasmonic effects around the composite structures. The light scattering from the SiO_2 structures is observed to increase the fluorescence signal of the labeled biomolecules by around 15-17 times for unbound and 100 times for bound relative to glass. However, these studies need further investigation into calculating the number of molecules getting enhanced within the localized region and normalizing this across the different substrates. The composite structures can be tuned to have a diverse range of nanostructures and nanogap sizes that can potentially have other plasmon resonances for achieving large fluorescence enhancements in other regions of the visible wavelength spectrum. Other fluorescently labeled proteins that excite in the blue and red wavelength regimes can be selected to investigate if enhanced emission signals can be generated. We have also recently demonstrated that our Ni structures can generate strong localized magnetic gradients to serve as effective nanogaps [242]. Combining this useful advantage with our gold structures can pave a way to create a comprehensive integrated device that can trap and detect magnetically labeled molecules and nanoparticles. Furthermore, our approach can be easily integrated into a portable microfluidic device to serve as a relatively low-cost and powerful technique for fabricating highly sensitive microfluidic sensors. Development of such

tools opens up the potential to bring a rapid, portable, diagnostic device that can detect biomarkers at a lower concentration than traditional sensors. Future work also with laser polarization studies will help understand if the fluorescence enhancements can be increased further.

Chapter 5 Single Molecule Detection

5.1 Introduction

For diseases diagnosis, having the ability to isolate and detect a single protein molecule associated specifically with the disease would facilitate with being able to diagnosis the disease at an earlier stage when it is treatable and can be halted from spreading further [243, 244]. Methods to achieve single molecule detection have been extensively explored by either reducing the observation volume to reduce the number of molecules examined and/or trapping single biomolecules by using metallic apertures [125, 245-247]. When compared to bulk measurements, single molecule techniques have numerous advantages that make it an attractive approach to explore further. First, they provide individual information about the dynamics of an individual molecule as opposed to an average of the population [248]. Also, tracking individual particles is a good way to understand the how biomolecules behave when interacting with their surrounding environment [249]. In addition, small changes in individual molecules are easier to monitor than when it is a collection of molecules.

The first demonstration of single molecule detection was performed in 1961 by Boris Rotman who sprayed a solution of enzyme and a fluorgeneic substrate over silicone oil to create droplets in oil [250]. After waiting for several hours, Rotman was able to detect and measure single enzyme molecules by examining the droplets that became fluorescent. Hirschfeld and his team used total internal reflection microscopy (TIRM) and applied a high laser power to photobleach labeled proteins [251]. After a majority of the labeled proteins were photobleached, only a few remained that needed to be analyzed. However, practically speaking, photobleaching of labeled protein molecules is not as feasible for early disease detection because typically there are only a few biomolecules to start with [247].

A more practical approach involves using techniques to reduce the observation volume significantly so that less number of molecules is studied. However, even with this method there is a limit to how far light can be confined in a small volume [252]. Several different methods have been developed to investigate and isolate single molecules from a bulk solution such as fluctuation correlation spectroscopy (FCS), total internal reflection microscopy (TIRF), zero-mode wave guides, and near-field scanning optical microscopy. Each of these methods have their advantages and disadvantages which have been listed below.

5.2 Single molecule detection methods

5.2.1 Fluctuation correlation spectroscopy (FCS)

FCS has emerged as a powerful experimental technique to study the molecular motions of a few fluorescent molecules in solution, cells and tissues[253]. In this method, examining the fluorescence intensity for spontaneous fluctuations can elucidate a wide variety of information about the molecule such as the diffusion coefficients, local molecular concentrations, rate of binding, and inter or intramolecular reactions [254]. FCS was introduced in 1972, Elson, Magde, and Webb used FCS to observe the fluctuations in the binding reaction process between ethidium bromide (EtBr) to double-stranded DNA. [255]. When EtBr bound in between the DNA bases, the fluorescence quantum yield increased significantly relative to when it was free moving in solution. Following these studies, further investigations were performed and two sources of fluctuations in the fluorescence intensity were noted. The first was related to the diffusion of molecules in and out of the sampling volume, and second was related to the chemical fluctuations in the binding/debinding of EtBr. Several years after the introduction of FCS, the theoretical framework behind single-point FCS had been somewhat understood, but optical

technology that could monitor the fluctuations in a small excitation volume still needed to be developed. With the introduction of confocal microscopy and two-photon microscopy, advances in FCS have been achieved[252]. Typically, the FCS analysis is done by exciting at small volumes using confocal microscopy or two-photon excitation and recording the fluorescence intensity as a function of time as molecules diffuse in and out of the excitation volume. In order to analyze the time when the fluctuations in the intensity occur, the analysis is performed using autocorrelation functions. For FCS analysis, the amplitude spectrum and temporal spectrum of the fluctuations are examined for understanding the fluctuations in the fluorescence intensity and these are obtained by using the photon-counting histogram and autocorrelation function, respectively[256].

By mathematical treatment of the fluctuations in the fluorescence intensity, a mathematical model can be derived. The following autocorrelation function can be derived which is presented in 5.2.1.1[257].

$$G(\tau) = \frac{< I(t)I(t+\tau) >}{< I(t)^2 >} \qquad (5.2.1.1)$$

In this equation, I is the intensity, t is the time, and τ is a time after t. From the amplitude of the autocorrelation function, the concentration of the fluorophore can be calculated because the amplitude is inversely proportional to the number of molecules. From the autocorrelation function, another relevant parameter that can be described by looking at the decay of the autocorrelation function is the diffusion time. The diffusion coefficient, D, is calculated at the half point of the autocorrelation function and is represented in equation 5.2.1.2 [258].

$$D = \frac{\omega_o^{\,2}}{4\tau_D} \qquad (5.2.1.2)$$

In equation 5.2.1.2, ω_o is defined as the distance from the optical axis and τ_D is the diffusion time. The Stocks-Einstein equation can be applied to obtain a relation between the diffusion coefficient D and hydrodynamic radius of a spherical object which is given by 5.2.1.3[257].

$$r_b = \frac{k_B T}{6\pi D\eta} \qquad (5.2.1.3)$$

In this equation, k_B is Boltzman constant, T is thermodynamic temperature and η is viscosity coefficient.

In order to fully understand a single fluorescence molecule, a few requirements must be met. Typically for FCS analysis to be effective, a high fluorescence count rate per molecule and low background noise is required. This means that the signal to noise ratio of the fluorescent molecule has to be greater than 3:1, while still keeping the excitation volume small enough to be able to distinguish individual objects. Also, for FCS analysis, the optimal biomolecule concentration has to be within the nM to 1 μM regime to observe few events [259].

5.2.2 Total internal reflection fluorescence (TIRF)

In 1981, Axelrod developed the technique of total internal reflection fluorescence (TIRF) which utilizes the interaction of light with different refractive indexes to observe fluorescent molecules diffusing at the interface[260]. When a beam of light travels from a media with a higher index of refraction to another media that has a smaller index of refraction, at the interface, some of the excitation is light reflected and at a specific angle some is refracted. When the illumination angle approaches the critical angle, the refracted beam becomes almost parallel to the interface. In this

case, all the excitation light is reflected back to achieve TIR. Higher than the critical angle, the beam's electric field generates an evanescent wave which extends into the second medium. Moving distances further away from the interface, the evanescent wave decays exponentially and is not able to sufficiently excite fluorescent molecules beyond 100 nm. When the laser beam shows TIR on the interface between the mediums with the different refractive indexes, the fluorescent molecules are excited by the evanescent wave. With this setup, an almost 2 orders of magnitude difference is observed in the observation volume relative to the conventional confocal microscope[261]. TIRF can also be combined with FCS techniques to provide excellent confinement in the z-direction, but still requires the use of a pinhole to reduce the lateral resolution. Thus, one of the issues with TIRF-FCS is that out of focus photobleaching that can result in a reduction of the fluorophores [262, 263].

5.2.3. Zero-mode waveguides (ZMW)

Similar to TIRF, ZMW use evanescent waves to reduce excitation volume to within 100 nm above the surface[264]. This idea was introduced in 2003 by Craighead and Webb[265]. Unlike TIRF, ZMW confines the excitation volume further than TIRF microscopy by utilizing sub wavelength holes that are on the order of 100 nm milled in metal films. These sub wavelength holes restrict the propagation of light from traveling further than the aperture. For a nanoaperature diameter of 100 nm, a three order magnitude of reduction in the detection volume from regular confocal microscopy can be obtained[266]. Furthermore, the sub-wavelength aperture can also enhance the signal to noise ratio for single molecule detection by increasing the fluorescence rate per emitter. However, as the aperture diameter decreases below 100 nm, the

fluorescence signal has observed to become quenched due to the nonradiative energy transfer to the metal.

5.2.4 Near-field scanning optical microscopy (NSOM)

NSOM operates similarly to an AFM by using a sharp tip to scan the surface and the height movement of the scanning probe is tuned by the atomic force interaction between the sample and probe tip. Pohl et. al was the first to demonstrate the use of NSOM as a feasible approach for improved resolution past the diffraction limit in imaging[267]. NSOM uses a nanoaperature similar to ZMWs to reduce the observation volume to within the attoliter regime. The resolution of this method is dependent on sample-to-probe distance and the size of the aperature. The sample is illuminated with evanescent light by a single-mode optical fiber probe and is strongly localized to the aperature. Further away from the probe, the evanescent field decays rapidly. However, similar to TIRF, NSOM is best for imaging samples that are positioned and held within nanometers of surface as the probe is scanned.

5.2.5 Two-photon microscopy

Almost all of the techniques described previously use some method to reduce the excitation volume so that a lower number of molecules are present in the system. This way it would be easier to monitor the fluctuation of individual molecules distinctly. However, one of the problems is that when there are less labeled biomolecules present in the system, the fluorescence signal for the molecules can be significantly weaker and difficult to detect over the background. In fact, one of the persistent challenges in fluorescence microscopy is to increase the signal to noise ratio of weakly fluorescent biomarkers or of biomolecules present at low concentration [268, 269]. Thus, in combination with small observation volumes, methods to enhance the

intensity of molecules have been exploited by researchers. Strategies to increase both the quantum yield of the dye as well as to reduce the excitation volume have been demonstrated using nanoplasmonic structures such as gold (Au) bowtie antennas, zero-mode waveguides, nanoparticles, and thin films [270-274]. These strategies have significantly enhanced fluorescence signals due to near field plasmonic interactions. Two-photon excitation fluorescence (TPEF) microscopy is a widely used imaging method in biomedical diagnostics[275]. TPE is leveraged extensively for biological imaging studies because in the near infrared region, there is less scattering loss, reduced photodamage, and a greater penetration depth [276]. TPE is able to significantly decrease the out-of focus fluorescence which is excited by scattered light and ultimately reduce background fluorescence. There is limited fluorescence from the background because the excitation probability is only noticeable at the diffraction limited focal point of the laser beam. The reduction in laser excitation scatter arises from the fact that the Rayleigh and Raman scatter from the laser excitation can be filtered out since they differ significantly from the emission. Recent studies have shown that illuminating nan scale metallic structures by a broadband femtosecond pulsed laser such as those used in two-photon microscopy can be an effective way to study the localization of light [82, 277]. One of the key advantages with using two-photon microscopy is that with this method, the fluorophore excitation is localized to the excitation focal volume which is generally within the femtoliter regime [192, 278, 279]. This is especially useful when studying fluorescence hotspots generated within nanoscale gaps. Furthermore, due to the nonlinear quadratic dependence of the two-photon excitation process, the intensity scales to the fourth power of the EM field in the metal so a larger enhancement in the fluorescence signal is typically expected [280].

Due to the quadratic increase in the electric field, two-photon absorption has shown to provide even more significant enhancements over one-photon absorption because the fluorescence emission intensity also scales quadratically. Efforts to improve the performance of TPEF have been achieved mainly by using Au nanoplasmonic substrates to enhance the two-photon absorption (TPA) cross-sections of dyes [281-286]. The enhanced fluorescence signal observed with these plasmonic substrates has been attributed to metal enhanced fluorescence (MEF) effects.

Sanchez et. al used an Au metal tip fabricated by etching and FIB to provide an enhanced electric field at the tip for the localized excitation of a dye [287]. They calculated that theoretically their Au tip could provide an enhancement of more than a 1000 fold in the intensity of the electric field relative to the incident light. Jung et. al fabricated an Au nanopattern with different thicknesses of polymeric film to which Cy5-DNA was attached. They observed that by tuning the thickness of the polymeric film, they were able to control the enhancements in their emission[288]. Enhancements in the emission were observed best with thicknesses between 5-25 nm and dropped with increasing thickness. They also showed that with two-photon excitation of the Cy5-DNA attached to the Au nanopatterns, they were able to detect two orders of magnitude more relative to the glass surface. Cohanoschi and Hernandez demonstrated a 480 fold increase in the two photon absorption cross section of Hoechst 33 258 with activated Au colloids[289]. Fischer et. al fabricated Au elliptical nanostructures (180 nm X 240 nm) and attached a 40 nm polymer spacer to which a dye was covalently attached [290]. Two plasmon resonances at 720 nm and 1300 nm were observed due to the elliptical geometry of the structures. Adding the polymeric spacer layer to the elliptical structures forced a red-shift of the plasmon resonances by 80 nm. They detected a 16 fold enhancement in their intensity when the dye was on their

elliptical nanostructures relative to when it was far away from the structures. Wenseelers et. al fabricated Ag fractal structures that were able to enhance the TPA of chromophores by 5 orders of magnitude [284]. Similar work by Hernandez et. al showed that with their Au fractals, a 157 fold enhancement in the TPA of chromophores was achieved. Sivapalan et. al attached organic chromophores to polyelectrolyte-coated nanorods and observed enhancements up to 40 fold in their fluorescence signal[291]. Varying the thickness of polyelectrolye coated on the gold nanorods yielded different enhancements in the fluorescence signal similar to previous studies. Aouani et. al used 3 μm dielectric latex spheres to enhance the fluorescent signal from Alexa 488 molecules 10 fold by illuminating the microsphere with a tightly focused Gaussian beam [292]. These studies, in short, showed that aggregated metallic clusters had extremely strong localized electric field enhancement effects resulting in improving the TPA cross-sections of chromophores.

5.2.6. Enhanced fluorescence detection of single molecules

However, these studies were primarily interested in enhancing the fluorescence signal of a collection of chromophores and were focused on single molecules, which would be important for early disease diagnosis. Methods to enhance the intensity of a single labeled molecule have been explored by researchers. Kinkhabwala et. al used electron beam lithography (EBL) to fabricate an array of Au bowtie nanoantennas with various gaps between the bowties [293]. What they noted was that when the gaps between the bowties were smaller than 20 nm, they were able to enhance a single molecule's fluorescence by up to 1340 times. Furthermore, their electromagnetic simulations revealed that the huge enhancements were a result of increased absorption and an increased radiative emission rate. Zhang et. al created Ag particle dimers with coupled metal nanoparticles and placed single Cy5 molecules in between the nanoparticles [294].

They observed a 7 fold increase in the signal molecule fluorescence on the metal monomer and a 13 fold increase for metal dimers relative to free Cy5 without metal. For the silver monomers and dimers, the lifetimes was also noted to be shortened. Yuan et. al observed more than 1100 fold enhancements using gold nanorods to increase the fluorescence of single molecules [295]. They also noted that the best increase was observed when the dye's emission and absorption overlapped with the surface plasmon resonance of the gold nanorods. Khatua et. al used their gold nanorods to enhance the single molecule fluorescence of crystal violet by more than 1000 fold[296]. Heuke et. al positioned a single DNA molecule tagged with one fluorophore into their 150 nm nanoaperatures by using passivated metal walls and biotin-neutravidin on the bottom of their aperatures [297]. They looked at the fluorescence lifetimes to quantify their fluorescence intensities and observed shorter lifetimes of their nanoaperture substrates relative to glass slide. Zhao et. al used gold nanorods with various layers of silica shell thicknesses to enhance the fluorescence signal of their fluorescent molecule, porphyrin, by 12 fold [298]. They noted that maximum enhancement of 12 fold in the fluorescence signal of the single molecule occurred with a 20 nm silica shell thickness. They also recorded a 70% decrease in the fluorescence lifetime.

5.3 Confocal microscopy with FCS to isolate single molecules

A couple of groups have combined the advantages of FCS with confocal microscopy to monitor the sudden increase in fluctuation in the fluorescence intensity of a single molecule. Aouani et. al used FIB to create a corrugated chromium/Au nanoaperature on a coated glass slide [299]. With FCS, they were able to quantify the fluorescence enhancement by examining the average number of molecules in the observation volume. From this, they were able to calculate the fluorescence count rate per molecule. Punj et. al used a spherical gold nanoparticle to

enhance the fluorescence brightness per molecule of Alexa 647 by 60 times and reduce the detection volume to 270 zeptoliters [300]. What was interesting about their work is that they were able to enhance the fluorescence of a single molecule from a micro molar stock concentrations. FCS analysis demonstrated that approximately one molecule was enhanced in the presence of a single Au particle with a 12 times increase in signal to noise ratio. In a follow-up to their work, Punj et. al used focused ion beam to fabricate an antenna-in-box that was milled in a 50 nm gold film on glass coverslip[301]. The plasmonic nanostructures were able to restrict the light down to nanoscale volumes and trap their fluorescent dye within the smallest gap of 12 nm. They showed that more than a 1000 fold increase in the fluorescence signal of a single fluorophore and an 8000 fold reduction in the observation volume occurred when it diffused in and out of the plasmonic gap.

5.4 Two-photon microscopy with FCS

Combining the advantages of two-photon excitation fluorescence with FCS could be a useful technique for single molecule detection due to its limited background fluorescence and reduction in laser excitation scatter compared to one-photon excitation. Thus integrating the advantages of FCS with TPEF into a nanoplasmonic device could serve to be a useful method for detecting higher concentrations of weakly fluorescent biomarkers.

Recently studies have demonstrated that a ferromagnetic material such as nickel (Ni) has the optical properties to support plasmons in the near-infrared to infrared region [302, 303]. However, one of the main disadvantages with using pure ferromagnetic materials is the strong absorption losses that occur resulting in a strong damping of the surface plasmonic features [304, 305]. To overcome this damping, there has been significant interest in combining ferromagnetic

materials with noble metals to create hybrid structures for increasing the plasmonic response [304, 306, 307]. These composite structures, also referred to as magnetoplasmonic structures, have demonstrated that magneto-optical effects such as the Faraday and Kerr effect fields can be implemented to control the surface plasmon propagation along nanostructured surfaces [304, 308-314]. We present here the first demonstration of leveraging the plasmons in Ni/Au composite structures for enhanced fluorescence signal by MEF in the near-infrared wavelengths [315].

5.4.1 Two-photon excitation of FITC-IgG on composite structures

In this section, we present a roll to roll compatible manufacturing process to create large areas of nanostructured bimetallic substrates fabricated by simply depositing Ni and Au thin films onto commodity shrink wrap polyolefin (PO) film. When the shrink film retracted, the thin stiffer metal films buckle to create 'wrinkle' structures [85, 87-89, 316]. This film shrinks considerably more than previously reported and thus results in significantly smaller structures [80-82]. A thin dielectric layer of silica (SiO_2) on top of the bimetallic structures served as a spacer layer. We characterized our metallic structures by depositing goat anti-mouse immunoglobulin G (IgG) antibody conjugated to fluorescein isothiocyanate, FITC, (FITC-IgG) onto our composite structures and determined the enhancements in the fluorescence signal by a combination of two-photon microscopy, FCS, and fluorescence lifetime imaging microscopy (FLIM) to spatially and temporally map the hot spots on an MEF surface. Importantly, we were able to achieve significantly higher resolution than previously reported and show for the first time down to 33 nm resolution with FCS and correlate this with FLIM mapping [82]. FCS revealed that the hot spots observed are reduced to below the confocal volume, and FLIM shows a shorter lifetime

present on the composite structures than in solution. This increase in the fluorescence signal and shortening in the fluorescence lifetime is due to the strong EM field localized around nanoscale gaps within our metallic structures. Finally, with this, we demonstrated we could detect single biomolecules by monitoring fluctuations in the fluorescence intensity of FITC-IgG antibody.

1 μM FITC-IgG (Sigma-Aldrich, USA) prepared in phosphate buffered saline (PBS) was pipetted on top of the composite structures and sandwiched by a thin glass coverslip before being mounted on the Zeiss LSM 710 microscope. The microscope was coupled to a mode-locked two-photon titanium (Ti)-sapphire laser (Spectra-Physics, Mountain View, CA) operated at 785 nm with a 80-MHz repetition rate. Samples were imaged with a 40×/1.2NA water immersion objective lens (C-Apochromat Water Corr, Carl Zeiss, Jena, Germany) and excited at 785 nm with a laser power of 150 μW. The emitted fluorescence light was selected by a spectral detector from 495-650 nm and detected by a photomultiplier tube. Images were captured at 8.5 μm X 8.5 μm zoom.

IgG was chosen as the model protein because it is one of the most abundant classes of immunoglobulin in blood [235]. FITC, a derivative of fluorescein, is one of the simplest and prevalently used fluorescent dyes for labeling peptides, proteins, and antibodies. Thus, for biological relevance, enhancing the fluorescence signal of FITC-IgG on the composite structures was chosen. As the fluorescently tagged antibodies diffused by Brownian motion, and passed within nanometer proximity over specific regions of the composite structures, the fluorescence signal was observed to suddenly burst, becoming significantly enhanced relative to the background signal. After the sudden burst in the fluorescence signal was observed, the signal immediately dropped, indicative of a hot spot [144, 317]. To determine the width of each of the bursts in the fluorescence signal, FCS line scanning was conducted.

FCS line scanning was obtained by scanning a line of length of 256 pixels 100,000 times, with a pixel size of 33 nm and a pixel dwell time of 1.00 μs to capture the rapidly diffusing molecules. An 8.5 μm horizontal line was scanned over the region where fluctuations in the intensity were observed. A time trace of the fluorescence intensity was collected for 60 seconds. Data analysis was processed by the SimFCS software developed at the Laboratory of Fluorescence Dynamics (LFD). Intensity data are presented using a carpet representation in which the *x*-coordinate corresponds to the point along the line (pixels) and the *y*-coordinate corresponds to the time of acquisition. Using the SimFCS program, the intensity data was threshold from 2500 to 4095 which is the maximum measurable intensity to look at the counts with the higher intensities. The value of 2500 was selected as the minimum intensity threshold in order to only look at the intensities that were at least 10 fold higher than the background noise. The background noise was measured using the composite structures with PBS. The specific line with point(s) of intensity larger than 2500 counts was examined to determine the size of the hot spot and the duration of the intensity fluctuation.

Fig. 5.1(a) presents the line scan carpet image for a region where a burst in the intensity signal was observed. The high fluorescence intensities are color coded red while the background and areas of lower fluorescence are color coded blue. Fig. 5.1(b) illustrates that the sudden increases in the fluorescence intensity occur for only one pixel and are at most 1 μs before dropping to the less enhanced signal. An estimation of the enhancement in the fluorescence signal revealed that more than three orders of magnitude relative to glass was observed. The horizontal line profile also argues against the fact that the bright signals are due to aggregation effects; if such were the case, the intense fluorescence signal would last several pixels long. Furthermore, these findings are consistent with previous work that have shown that as the gaps between metallic structures

become less than 50 nm, the fluorescence signal significantly increases [125]. Since the diffusion coefficient of FITC-IgG is around 40-50 $\mu m^2/s$, the molecules are moving relatively fast and the hotspots would only be observed for a brief time. Figure 5.1(b) reveals that these short bursts in the fluorescence signal were not observed on the control samples which were the composite structures with PBS, glass coverslip with PBS, and glass coverslip with FITC-IgG. This further supports that these bursts in intensity are related to the near-field effects from interaction of FITC-IgG with the composite structures and not due to possible artificial noise effects (i.e laser) or from the analog detector. The low level fluctuations in the signal observed on the control conditions, glass coverslip with PBS and FITC-IgG and composite structures with PBS were similar; we further confirmed that at 150 µW laser power, FITC-IgG on the glass coverslip was undetectable. While slight fluctuations in the signal occurred on the control samples, they were negligible relative to the magnitude increase in the fluorescence signal observed on the composite structures. Previously, amplitude analysis was used to estimate the hot spot volume because the spatial resolution was diffraction limited to ~300 nm [82]. In this work, using FCS to analyze the line scan data significantly improved the spatial resolution and quantified the hot spots to be less than 33 nm, translating to attoliter hotspot volumes. For the 1 µM FITC-IgG stock concentration pipetted on top of the composite structures, we observed one molecule diffusing into the "hotspot" region at a time. To examine the number of times a single molecule diffused to the "hotspot" region and became significantly brighter, a position in the sample was fixed and monitored for 60 seconds. Figure 5.1(c) illustrates that for a fixed position, multiple hotspots of comparable magnitudes occur. The vertical line profile also confirms that these short bursts in the fluorescence signal are not due to the FITC-IgG molecules adhering to the metallic surface; aggregation would result in the bright signal to last for several lines or more than the

line time of 0.6 ms. The vertical line profile revealed that the enhancements in the signal achieved with these composite structures is comparable in intensity to those achieved with bimetallic nanopetals, but at a laser power that is almost 12 fold lower [82]. As expected, as the laser power was increased, an increase in the population of hot spots was noted. Since the intensity scales to the fourth power of the EM field in the metal in two-photon excitation, the enhancements achieved are significantly larger than previously demonstrated.

Figure 30(d) shows the histogram profile for the collection of line trace scans and illustrates that significantly brighter pixels are observed on the composite structures compared to the controls. The PBS on the composite structures has a slightly higher signal but does not produce a significant amount of background signal to contribute to the enhanced signals observed on the composite structures.

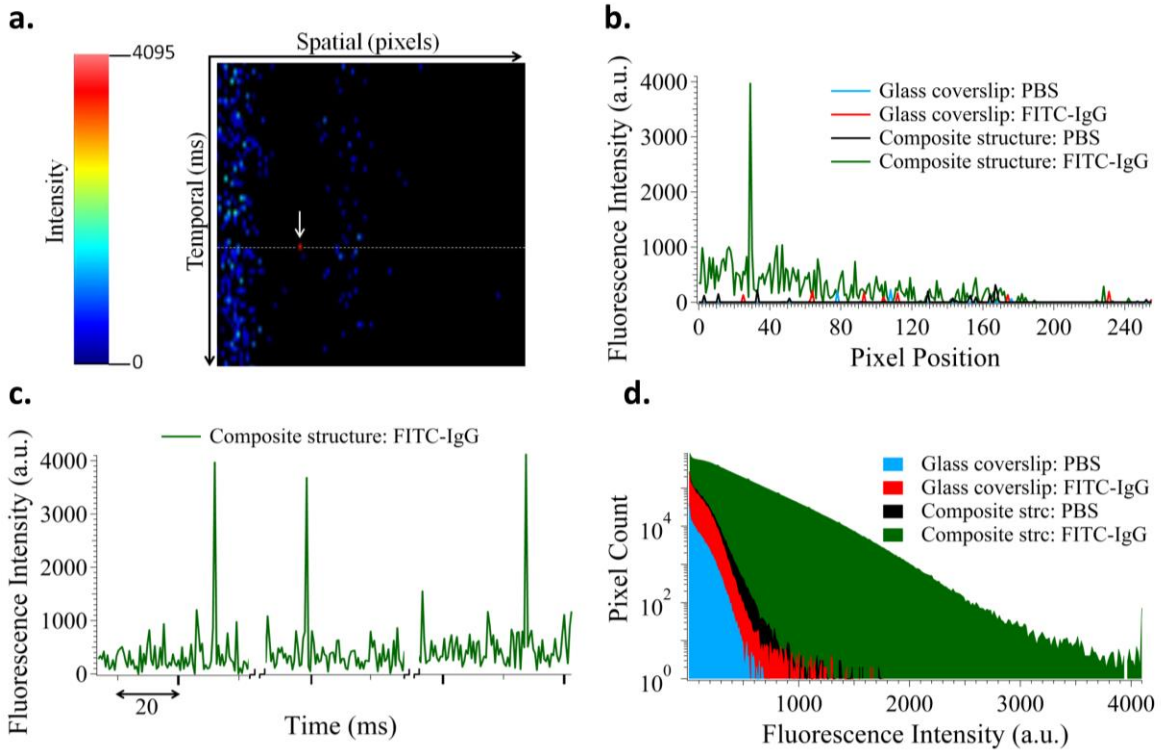

Figure 5.1 Fluorescence line scan analysis of 1 µM FITC-IgG and PBS at 785 nm excitation on glass coverslip and composite structures (a) Fluorescence image from scanning FCS of composite structure where hotspots were observed indicated by white arrow (b) Horizontal line intensity profile for fixed time point (c) Vertical line intensity profile for a fixed pixel position collected for 60 sec (d) Histogram distribution profile of the fluorescence intensities.

We also investigated if higher thicknesses of Au, 20 and 30 nm, could support such bursts in the fluorescence signal. Figure 5.2(a) reveals that for both the 20 and 30 nm Au composite structures, bursts in the fluorescence signal were also recorded. However, as the Au thickness increased, the intensity of the burst decreased. For the 20 nm composite structures, the burst in the fluorescence intensity was noted to be around 3100 while for 30 nm, the burst was around 2000. One interesting point to mention is that the bursts in the fluorescence intensity were determined to occur also within one pixel similar to what was observed with the 10 nm composite structures. However, it is possible that since 1 pixel is at the very most 30 nm in size, these fluorescence enhancements could all be occurring at different sizes less than 30 nm. We predict that the enhancement from the 10 nm Au composite structures arises from the smallest gaps in the structure compared to the 30 nm Au composite structures. The other

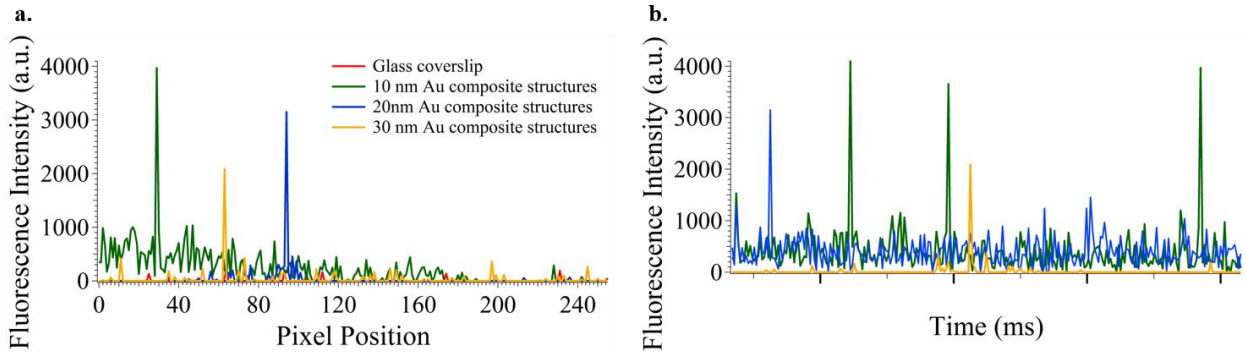

Figure 5.2. Fluorescence line scan analysis of 1 µM FITC-IgG at 785 nm excitation on glass coverslip and composite structures (a) Horizontal line intensity

profile for fixed time point (c) Vertical line intensity profile for a fixed pixel position collected for 60 sec.

The histogram profile for the collection of line trace scans presented in Figure 5.3 also illustrates a similar point that significantly brighter pixels are observed with thinner Au composite structures relative to the thick, 30 nm composite structures. In all cases, the fluorescence intensity on the composite structures is significantly brighter relative to the controls.

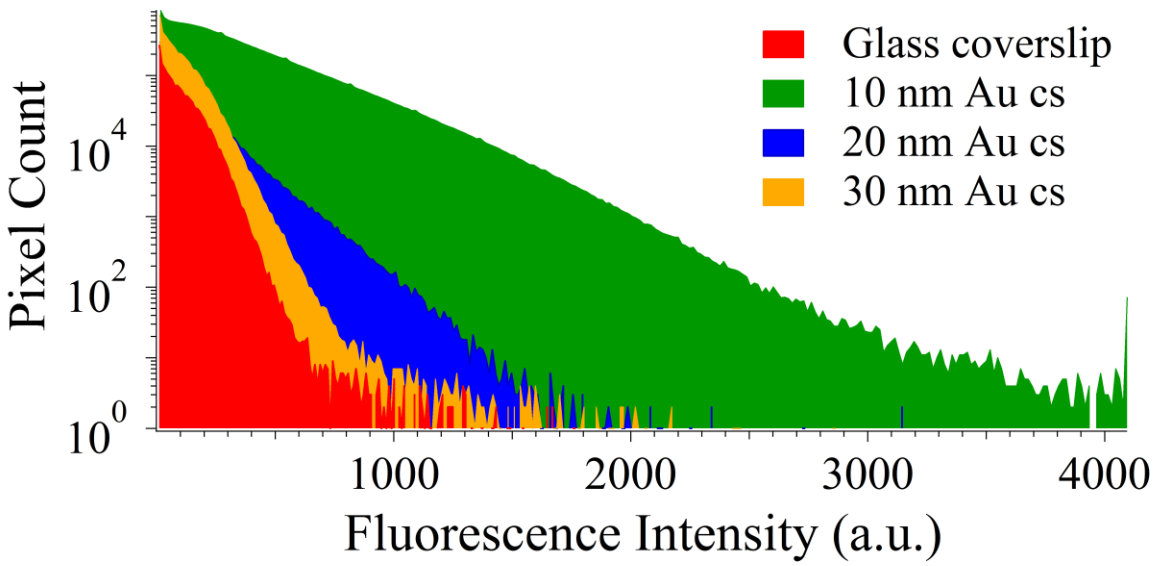

Figure 5.3. Histogram distribution profile of the fluorescence intensities for the 10 nm, 20 nm, and 30 nm composite structures.

If the increase in fluorescence signal is due to plasmonic effects, the lifetime of the fluorophore is also expected to be reduced [69, 209]. The phasor approach in the frequency

domain has the ability to visualize and distinguish multiple species present in a mixture and can filter out unwanted artifacts such as erroneous background noise (i.e. room light) [191].

Fluorescence lifetime images were acquired with a Zeiss 710 microscope coupled to a Ti:Sapphire laser system. A 40X/1.2NA water immersion objective was used for imaging. For image acquisition the following settings were used: image size of 256 X 256 pixels and scan speed of 25 μm/pixel. A dichroic filter (760 nm) was used to separate the fluorescence signal from the laser light and the fluorescence emission was collected from 515-565 nm. For the acquisition of FLIM images, fluorescence was detected by a photomultiplier (H7422P-40, Hamamatsu, Japan) and a 610 nm short pass filter was placed in front of the detector. FLIM data was acquired and processed by the SimFCS software developed at the LFD. The excitation wavelength used was 785 nm. An average power of about 150μW was used to excite the FITC-IgG on the composite structures and 800 μW for FITC-IgG in solution. The FLIM calibration of the system was performed by measuring the known lifetime of fluorescein with a single exponential of 4.04 ns at a laser power of 800 μW. The phasor transformation and data analysis of the experiments was also performed using the SimFCS software, as described in previously published papers [318]. The phasor approach to FLIM converts at each pixel in an image the fluorescence decay histogram into the sine and cosine components. These components are then represented in a two dimensional histogram also referred to as a phasor plot. Each of the pixels in the image results in a single point in the phasor plot and when used in reciprocal mode, each point of the phasor plot can be mapped to each pixel in the image. The histogram was plotted by finding the average phasor, τ_p, in the program.

Figures 5.4(a)-5.4(c) display the FLIM images of FITC -IgG on the glass coverslip and on the composite structures as well as the phasor plot to map out where the fluorescence lifetimes lie for

each pixel. Briefly, all points that are on the universal circle in the phasor plot have single exponential lifetimes which are related to one species while those inside the circle have multiple exponential lifetimes. The fluorescence lifetime of FITC-IgG on glass is observed to be uniform and centered around 2.8 ns on the universal circle as depicted by the red color shown in Figure 5.4(a) [319]. In contrast, on the composite structures with FITC-IgG, mapping the lifetimes from the FLIM image reveals a distribution of lifetime which extends from 2.8 ns to less than 50 ps. In our previous work, we performed FLIM by using the time correlated single photon counting card and were only able to present the average lifetime of the species in an image [82]. Here, using the phasor approach with FLIM, lifetime differences across the image can easily be observed and mapped. Mapping out where lifetimes shorter than 100 ps exist confirms that these lifetimes are observed in areas with high fluorescence intensity. This is also represented quantitatively by plotting out a normalized histogram of the lifetime values shown in Fig. 33(d). Similar to the FLIM map, the FITC-IgG on the glass coverslip is centered around 2.8 ns. In contrast, the histogram profile of the lifetime values for FITC-IgG on the composite structures has a range from 2.8 ns to mostly less than 50 ps, which is at the limit of the lifetime detection system. The observed decrease in lifetime on the composite structure at the points where the structures are the brightest is attributed to the enhancement of local excitation electric fields, leading to an increased excitation rate of fluorophores and radiative decay rate. This significant increase in the radiative decay rate implies an increase in the rate of emission of the fluorophore. The slight shifts in the fluorescence lifetime of FITC-IgG on the unenhanced regions on the composite structures could be due to changes in the refractive index which is known to also affect fluorescence lifetime [320].

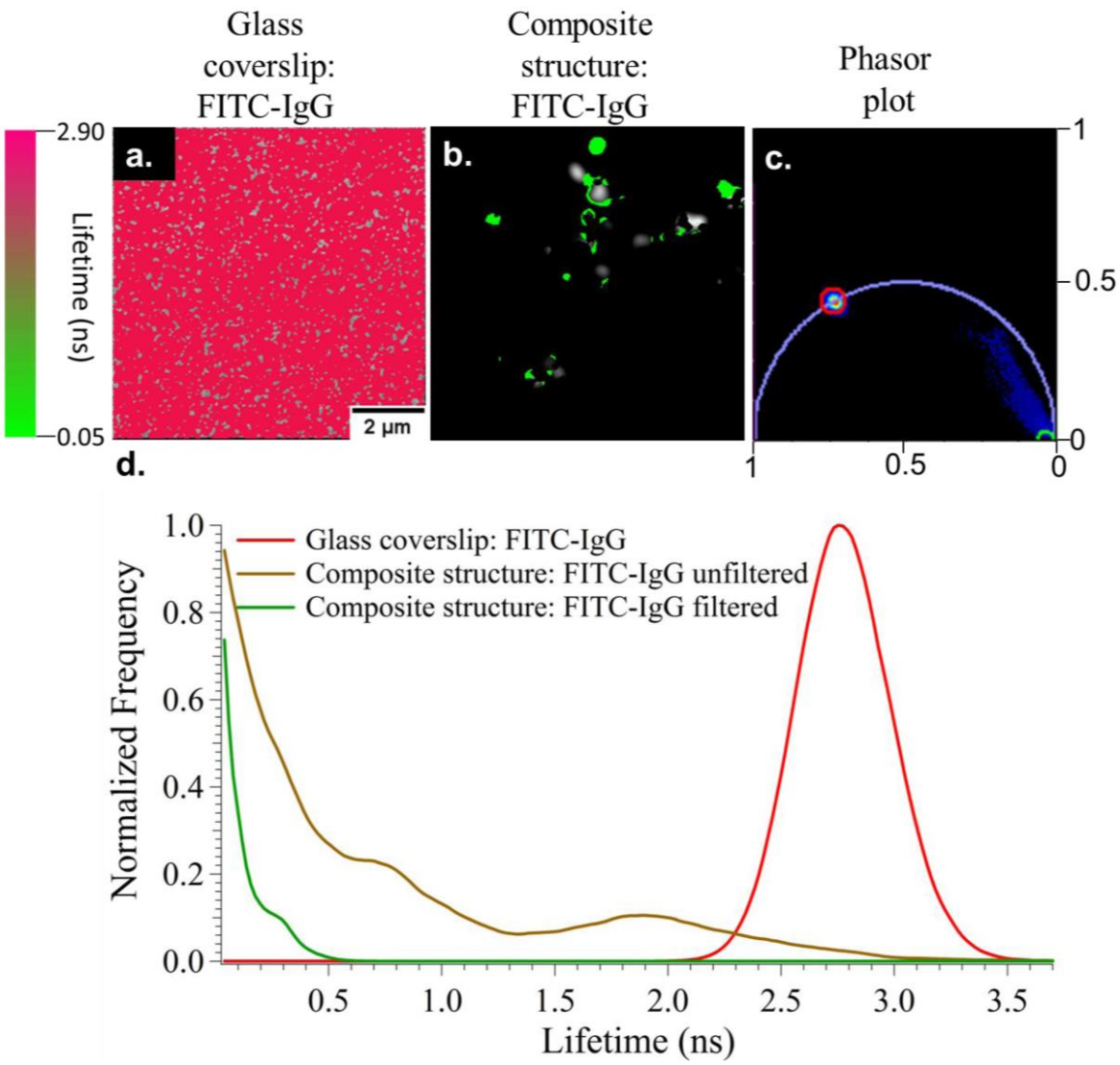

Figure 5.4 Fluorescence lifetime analysis of 1 µM FITC-IgG at 785 nm excitation. (a) FLIM image on glass (b) FLIM image on composite structures (c) Phasor plot to show lifetime distribution (d) Normalized frequency profile of lifetimes.

Figure 5.4 (a)-(c) shows the FLIM images for FITC-IgG on the 10 nm Au, 20 nm Au, and 30 nm Au composite structures. Using the phasor plot presented in Figure 5.4(d) to map out where the short lifetimes occur reveals that the in the areas where intensity is higher than the background, the lifetimes are shorter. However,

the fluorescence lifetime histogram profile presented in Figure 32(e) indicates that the as the Au thickness increase, the fluorescence lifetime extends to longer lifetimes. The average fluorescence lifetime for the bright spots on FITC-IgG were noted to be at the limit of detection of the system, while the lifetimes on the 20 nm and 30 nm Au composite structures (c.s) indicated that the lifetime was around 180 ps and 250 ps, respectively. For the 30 nm Au composite structures, the majority of lifetimes were actually revealed to be closer to the lifetime of the FITC-IgG in solution.

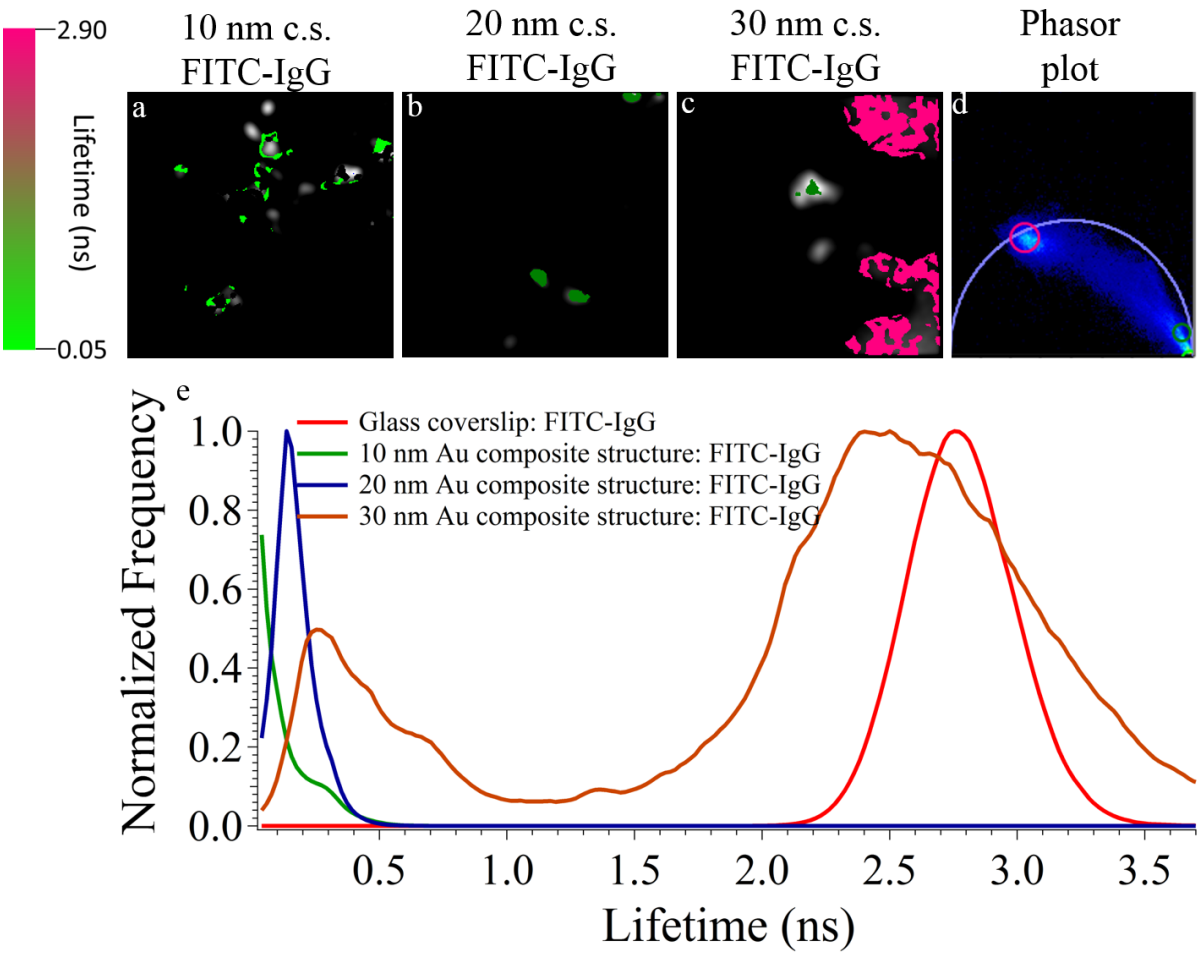

Figure 5.5. Fluorescence lifetime analysis of 1 µM FITC-IgG at 785 nm excitation. (a) FLIM image on 10 nm Au composite structures (b) FLIM image on 20 nm Au composite structures (c) FLIM image on 30 nm Au composite structures (d) Phasor plot to show lifetime distribution (e) Normalized frequency profile of lifetimes.

5.4 Summary

The 10 nm Au composite structures described in the previous section have the ability to enhance the fluorescence emission of labeled biomolecules by more than three orders of magnitude relative to a glass slide. These structures can be tuned to have a diverse range of architectures and nanogap sizes with tunable plasmon resonances. This is important to achieve large

fluorescence enhancements in other regions of the excitation wavelength spectrum. We have also recently demonstrated that our Ni structures can generate strong localized magnetic gradients to serve as effective nanotraps for capture and separation [88]. Combining this utility with the large signal enhancements demonstrated here can pave the way to create a comprehensive integrated device to readily magnetically trap and sensitively detect labeled molecules and nanoparticles.

The ability to create large areas of nanostructured substrates is also possible because the process can be compatible with roll to roll manufacturing processes We characterized our metallic structures by depositing goat anti-mouse immunoglobulin G (IgG) antibody conjugated to fluorescein isothiocyanate, FITC, (FITC-IgG) onto our composite structures and determined the enhancements in the fluorescence signal by a combination of two-photon microscopy, FCS, and fluorescence lifetime imaging microscopy (FLIM) to spatially and temporally map the hot spots on an MEF surface. Importantly, we were able to achieve significantly higher resolution than previously reported and show for the first time down to 33 nm resolution with FCS and correlate this with FLIM mapping [82]. FCS revealed that the hot spots observed are reduced to below the confocal volume, and FLIM shows a shorter lifetime present on the composite structures than in solution. This increase in the fluorescence signal and shortening in the fluorescence lifetime is due to the strong EM field localized around nanoscale gaps within our metallic structures. Finally, with this, we demonstrate we could detect single biomolecules by monitoring fluctuations in the fluorescence intensity of FITC-IgG antibody.

Chapter 6. Enhanced Fluorescence Detection with Non-Metallic Structures

6.1 Introduction

As described in the previous chapter, noble metal nanostructures and nanoparticles can significantly enhance the fluorescence signal through the concept of MEF. These techniques use surface plasmons to modify and improve the spectral and photo physical properties of fluorophores [321, 322]. However, these metallic structures typically require precise and sophisticated equipment to yield near-field metal enhanced fluorescence (MEF) effects (within nanometric lengths from the surface) in heterogeneous areas of 'hot spots'.[323-326] While fluorescence enhancements greater than 1000 fold have been observed, these plasmon-coupled effects are hindered by the fact that enhancements are heterogeneous with small areas of 'hot spots' and are the enhancements are wavelength dependent.

Fluorescent nanoparticles have emerged as a competitive method that have been applied as labels, tracers, and biosensors[327]. Examples of effective fluorescent nanoparticles are quantum dots which are basically semiconductor colloidal crystals with dimensions of a few nanometers [328]. These quantum dots are generally brighter and more photo stable than organic fluorescent dyes and fluorescent proteins [329]. They also benefit from the fact that they require less energy to be excited regardless of the size of the quantum dot. Still, the idea of using quantum dots for enhancing the emission of fluorophores is not widely accepted because of a couple of disadvantages. Some quantum dots could possibly have surface defects which could affect the quantum yield properties of quantum dots. Another disadvantage is that quantum dots have shown to pose a cytotoxic risk to biological specimens.

6.2 Enhanced fluorescence detection with SiO_2 nanoparticles, reflective surfaces

Instead, an alternative to quantum dots is to use reflective surfaces such as silica (SiO_2) on silicon (Si) as a platform for enhancing fluorescence microarrays [330-332]. These reflective substrates typically require a transparent spacer layer provided by the SiO_2 between the reflective surface (Si) and the fluorescent material. The fluorescence signal enhancement is based on the principle of optical interference [333, 334]. Redkar et. al coated borosilcate glass with alternate high to low refractive index coatings to form a multilayer stack of dielectric, thin film coatings[335]. The multilayer design facilitated with making the interference constructive so that the electric field strength could be enhanced within 60 nm to the surface and also reflects and redirect microarray fluorescence signals towards the detector. DNA microarray experiments were conducted on the optical interference slides and an 8 fold increase in the signal amplification relative to glass slide was observed. Cretich et. al coated a silicon substrate with a thermally grown layer of silicon dioxide, SiO_2, and functionalized it with a thin polymeric film[336]. Similar to Redkar et. al's study, the SiO_2 layer provides constructive interference between the incidence and reflected waves of the fluorescence radiation. Another important aspect of their substrate was the sub-nanometer surface roughness provided by the SiO_2 on the silicon aided in a reproducible coverage with biomolecules. They tested the performance of their substrates by enhancing the fluorescence signal of protein and peptide microarrays and noted a 5-10 fold increase in the fluorescence signal. Marino et. al deposited first a thin aluminum-silicon copper alloy followed by a thin SiO_2 layer onto their silicon substrate[333]. The advantage of adding the aluminum is that in the visible spectrum, it has high reflectance without autofluorescence. In other words, the metal with silicon acts as an optical reflector for the fluorescence signal by collecting a majority of the light. The SiO_2 layer contributes to the

enhanced signal by optical interference and allowing for the maximum electric field of the laser's electromagnetic wave on the surface.

In addition to their optical properties, SiO_2 surfaces have also been attractive surfaces for their high biocompatibility properties and the ease of surface functionalization. [337, 338] Recently, studies have shown that enhancements of fluorescence quantum yield of dye molecules can be achieved through covalent encapsulation of dye into SiO_2-based nanoparticles [339-343]. In particular, the use of dye-doped SiO_2 nanoparticles has presented significant interest due to its advantageous high surface to volume ratio, photochemical stability, and ability to amplify the fluorescent signal [344-346]. The mechanism of fluorescence enhancements is related to the internal SiO_2 architectures shielding the fluorescent dyes from being quenched by its surroundings, thus reducing the kinetics of the irradiative decay of the excited fluorophores [345, 347]. Furthermore, immobilization of the fluorescent dye within the SiO_2 matrix has been thought to restrict the mobility and flexibility of the molecules, which can lead to reduced nonradiative relaxation and subsequently increased photoemission brightness [343, 345, 348].

Typically, two chemical approaches have been applied to encapsulate the dyes into silica nanoparticles[349]. In the first approach, the dye is covalently bound to the silica matrix by linking the chemical groups from the dye with the silica matrix. In the second approach, the dye is entrapped within the silica matrix by electrostatic interactions through a reverse microemulsion process[350]. Gilliland et. al embedded various dyes into their silica sol-gel thin films and observed changes in the photostability depending on its surrounding environment[340]. Liang et. al investigated the effects of the nanoscale matrix on the properties of molecules that were encapsulated within[347]. The nanoscale matrix reduced the collision between the dye molecules and atmospheric oxygen preventing the dye molecules from quenching. The lower the

number of dye molecules present in the nanomatrix, the higher was the quantum yield. Furthermore, the size of the nanomatrix also played a role in the enhancement of the fluorescence quantum yield. The larger the nanomatrix, the higher was the fluorescence quantum yield when same amount of dye molecules were encapsulated within. Larson et. al covalently encapsulated multiple rhodamine dyes molecules into their 30 nm silica nanoparticles and observed a 20 times brighter signal relative to free dye[351]. They noted that the photophysical properties of the dye could be manipulated by making small changes in the internal architecture of the silica nanoparticles. They attributed the enhanced fluorescence signal to occur due to a combination of incorporating multiple dye molecules and enhancement of the quantum yield efficiency of the incorporated dye molecules.

However, typical enhancements from this approach have been modest, with increases in the fluorescence signal of 5-30 fold [352, 353]. Recently, Lin et. al reported generating SiO_2 structures from a pre-coated thermoplastic polyolefin (PO) shrink film (PO-SiO_2) to enhance the fluorescence signal of covalently bound biotin-streptavidin-Tetramethylrhodamine isothiocyanate (TRITC) biomolecules [241]. In this method, through a combination of surface concentration, light scattering, and changes in photophysical properties of the confined dye molecules, 116 times fluorescence signal enhancements and increased signal-to-noise ratio (76:1) were demonstrated using the SiO_2 structures as the platform.

6.3 Silica structures using shrink film to enhance fluorescence signal

Inspired by the fluorescence enhancements observed of the streptavidin-TRITC system using the SiO_2 nanostructures, we expanded upon this strategy and demonstrated its applicability to DNA fluorescence microarrays. The development of DNA microarrays has proven invaluable for high throughput quantification of gene expression profiling, genomic analysis, disease diagnosis, and

drug screening. [354-358] Fluorescence based DNA microarrays offer numerous advantages, such as high sensitivity and multiplexing capabilities. [359, 360] Despite these benefits, the challenge to improve the detection sensitivity persists. [361, 362] Strategies to increase the fluorescence sensitivity of DNA microarrays include increasing the amount of the capture probes or alternatively, amplifying the fluorescence signal using surface enhancements. To increase the density of DNA probes immobilized on the surface, techniques involving nanostructured substrates using three-dimensional structures, such as dendrimeric/nanopillar-like structures or grafting polyethylene glycol (PEG) layers onto silanized glass slides, have been pursued. [352, 353, 362-365] Increases in the fluorescence intensity of 2-30 fold were observed using these approaches to enhance the DNA probe density. However, oversaturation of probe density can reduce target DNA binding efficiency because of strong electrostatic repulsions, which leads to retardation of hybridization kinetics. [352, 366, 367].

In this section, we improve the limit of detection (LOD) sensitivity of the DNA hybridization assay by more than 40 fold compared to controls (a glass substrate). Our results demonstrate that our PO-SiO_2 structured substrate is an attractive approach for DNA fluorescence microarrays.

Experimental

The fabrication of these substrates is simple, inexpensive, robust, and scalable. To prepare the substrate, a laser cut tape mask with an array of 1 mm holes was applied to a clean polyolefin (PO) shrink film (955-D, Sealed Air Corporation, 1 mil) prior to sputter deposition of 20 nm SiO_2 to generate PO-SiO_2 substrate (Figure 6.1(a-b)). The PO-SiO_2 substrate was chemically activated by oxygen (O_2) plasma treatment and then functionalized with primary amine groups for DNA probe attachment (Figure 6.1(c-d)). The PO-SiO_2 surfaces were incubated with 2

mg/mL poly(L-glutamic acid) in PBS buffer for 1 hour (Figure 6.1(e)). 250 μM amine-modified single stranded (A_{30} ssDNA) solution in a PBS buffer that contained 75 mM 1-ethyl-3-(3-(dimethylamino)propyl)carbodiimide hydrochloride (EDC) and 15 mM *N*-hydroxysulfosuccinimide (NHSS) was prepared. 0.5 μL of two amine-terminated 30mer oligonucleotides A (A_{30} sequence) and B (GFP) with an A:B percentage of 80:20, 60:40, 50:50, 40:60, 30:70, 20:80, 10:90, 5:95, 1:99, 0.5:99.5, and 0:100 were incubated overnight on the PO-SiO_2 surfaces (Figure 6.1(f)). After rinsing the PO-SiO_2 substrates with PBS and water, 0.5 μL of 1 μM complementary ssDNA to A_{30} tagged with Cy3 fluorophore was allowed to react for 40 minutes (Figure 6.1(g)). After rinsing again with PBS and water, the substrates were dried with nitrogen (N_2), and then immediately imaged using a custom built upright fluorescence microscope (Olympus) with a 2x/0.55NA objective (Edmond Optics) and TRITC filter. The fluorescence intensities were analyzed using the region of interest (ROI) feature in ImageJ (National Institute of Health-NIH). PO-SiO_2 substrates were heated at around 160º C for 2 minutes, which induced retraction of the PO shrink film (Figure 6.1(h)). This caused the thinner SiO_2 film to buckle and fold into nano to micro-scale structures with high aspect ratios (Figure 6.2(a-b)). This resulted in a PO-SiO_2 structured substrate referred to here on as shrunk PO-SiO_2. The substrates were imaged again with the upright fluorescence microscope at the same conditions as previously mentioned.

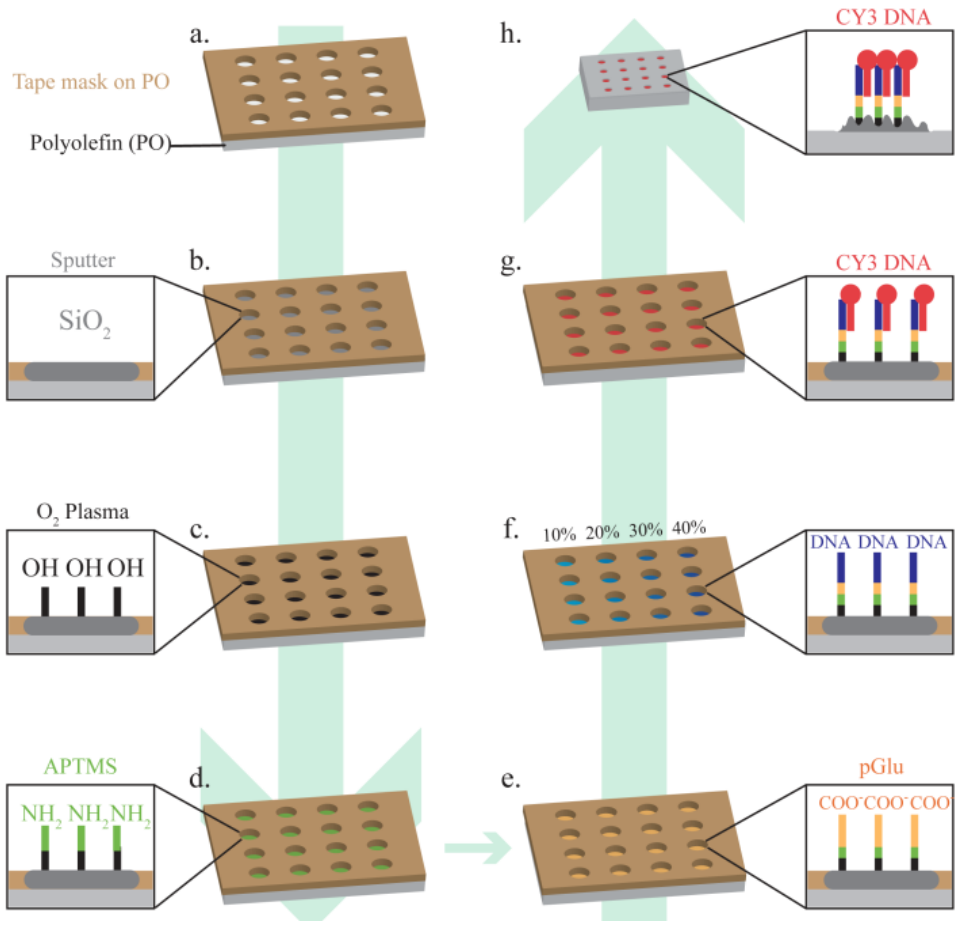

Figure 6.1 Schematic for fabrication of DNA fluorescence microarray on shrunk PO-SiO_2.

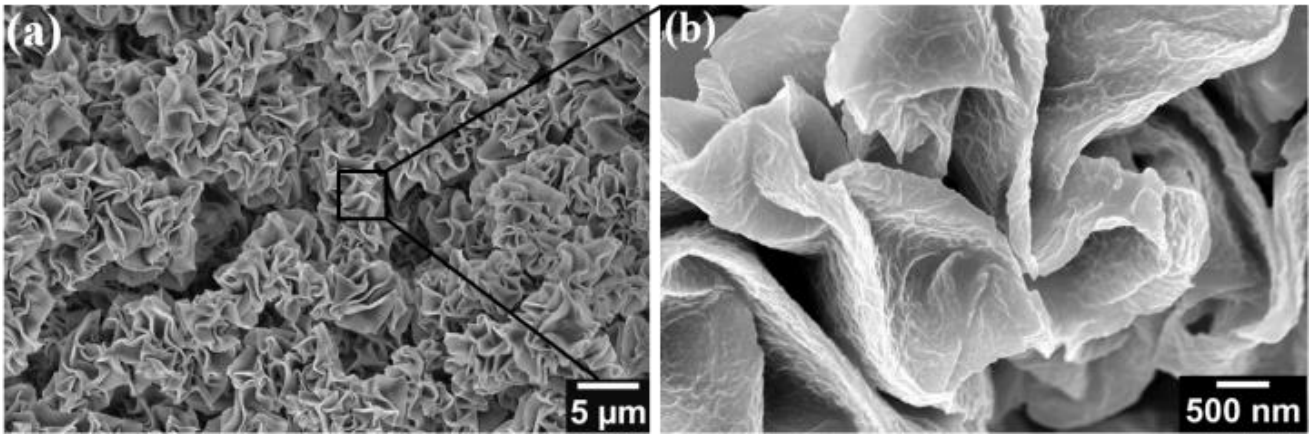

Figure 6.2. (a) Top down SEM image of the shrunk PO-SiO_2 is a representative image of the heterogeneous populations of nano and micro-scale structures observed (b) Zoomed in SEM image illustrating the micro and nano-scale features.

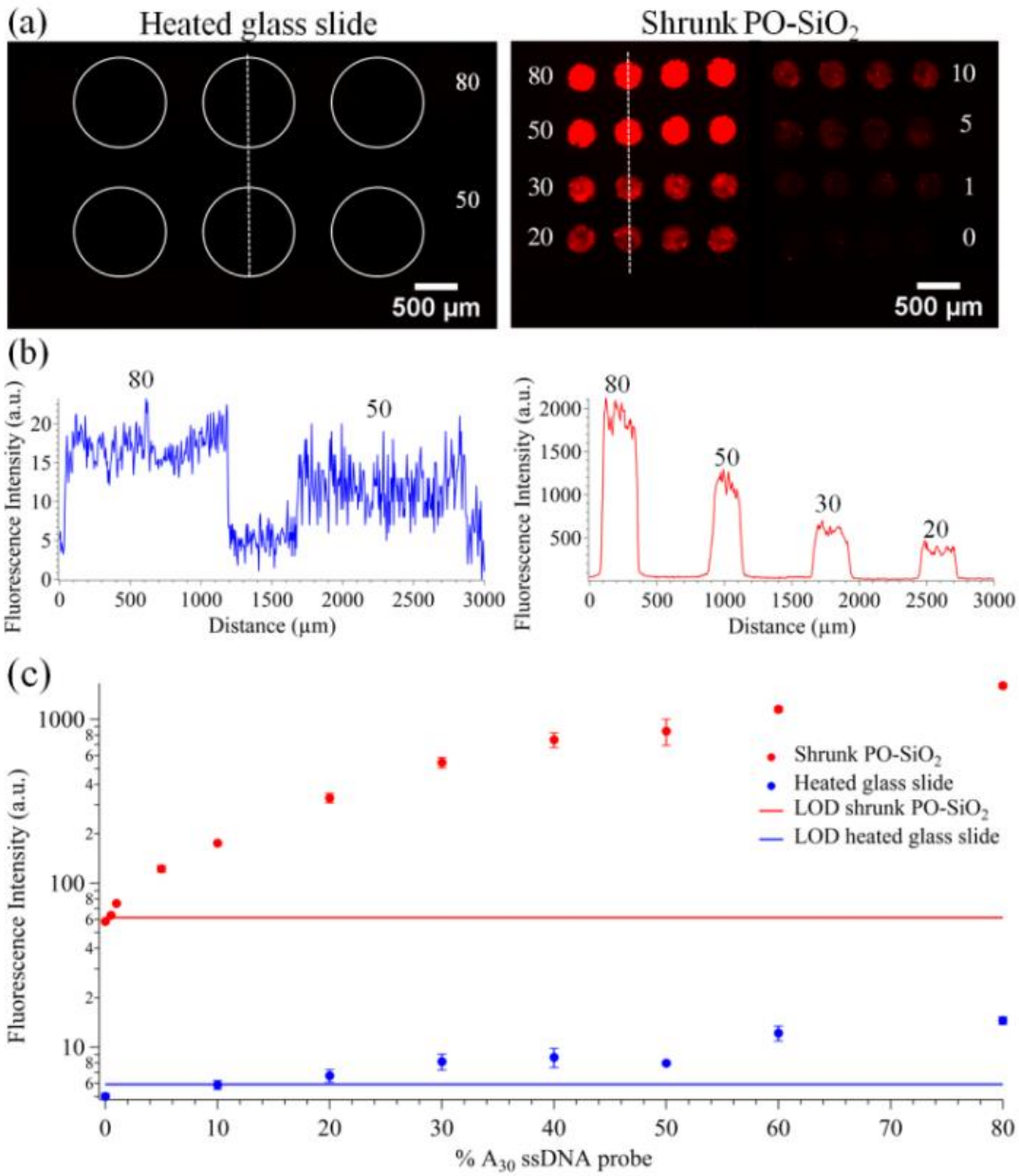

Figure 6.3. DNA fluorescence microarray of Cy3-DNA on heated glass slide and shrunk PO-SiO_2. (a) Fluorescence images of Cy3-DNA on heated glass and shrunk PO-SiO_2 and (b) their corresponding line plot profiles (c) Concentration curve of DNA fluorescence microarray on heated glass and shrunk PO-SiO_2.

Comparing the fluorescence images for the DNA microarray on the glass slide and shrunk PO-SiO_2 substrate, respectively, the dramatic fluorescence enhancements due to the substrate is apparent. As depicted in Figure 6.3(a), the fluorescence signal at 80 and 50% A_{30} ssDNA on the shrunk PO-SiO_2 substrate was detectable with the naked eye while the fluorescence signals on the glass substrate at those concentrations were not discernible. In fact, even at the lowest concentration of 1% A_{30} ssDNA, the fluorescence signal was still be observed on the shrunk PO-SiO_2 substrate. Another noticeable difference is that within the field of view selected (5 X 4 μm), 32 spots were visible on the shrunk PO-SiO_2 substrate while 6 spots were visible on the glass slide. This highlights the ability to rapidly detect multiple concentrations on the shrunk PO-SiO_2 substrate relative to a planar surface in regards to multiplexing capabilities. The dotted vertical white line represents where the plot profile was obtained for the different % of A_{30} ssDNA. The line profile shown in Figure 6.3(b) illustrates the fluorescence signal uniformity over the SiO_2 islands on the shrunk PO-SiO_2 and glass slide substrates. Furthermore, the enhanced fluorescence signal observed on the shrunk PO-SiO_2 substrates is not localized to nanoscale regions, as with plasmonic effects. The larger working range on the PO-SiO_2 substrate is apparent by the concentration curves for each substrate (Figure 6.3(c). The linear range on the shrunk PO-SiO_2 substrate was observed to be from 5-40% A_{30} ssDNA while on the glass slide, was observed to be from 10-30% A_{30} ssDNA. The detection limit (χ_{LOD}) was calculated, as shown in Equation 6.3.1, by taking three times the standard deviation of the background signal, $\bar{\sigma}_{bg}$, on glass or the shrunk PO-SiO_2 substrate and adding the mean background signal, $\bar{\chi}_{bg}$.[368] The $\bar{\chi}_{bg}$ was measured by calculating the fluorescence intensity of the nonspecific binding of the Cy3 DNA to the 0:100 sequence on glass and shrunk PO-SiO_2.

$$\chi_{LOD} = \bar{\chi}_{bg} + 3\bar{\sigma}_{bg} \quad [6.3.1]$$

The concentration curve demonstrates that a relative surface coverage of 0.5% A_{30} ssDNA can be detected on the shrunk PO-SiO_2 substrate in contrast to 20% A_{30} ssDNA observed on the glass slide.

Fluorescence signal enhancement was measured quantitatively and results were compared to that obtained from the DNA hybridized on the glass slide. The average fluorescence signal (FS) increase of the substrates is calculated according to Equation 6.3.2 as previously reported by measuring the mean FS obtained after heating (AH) ($\bar{\chi}_{ahs}$) minus the mean background FS AH ($\bar{\chi}_{ahbg}$) over the mean FS before heating (BH) ($\bar{\chi}_{bhs}$) minus the background FS BH ($\bar{\chi}_{bhbg}$).

$$\frac{\bar{\chi}_{ahs} - \bar{\chi}_{ahbg}}{\bar{\chi}_{bhs} - \bar{\chi}_{bhbg}} \quad [6.3.2]$$

As previously mentioned, the PO film shrinks by 77 % in each length post heating, which leads to an approximately 20-fold concentration of surface area. [83] Lin *et. al* showed that with the substrate alone, a 14 fold increase in the fluorescence signal of TRITC was noted to occur with the biotin-streptavidin model system relative to the planar PO substrate and a 50 fold increase with the silica structures relative to the planar PO-SiO_2 substrate. [241] This increase in enhancement was determined to be due to photophysical effects of the highly scattering PO-SiO_2 structures. Here, the fluorescence signal of the Cy3-DNA was observed to increase by 45 times (standard error (S.E.) 3.5) on the shrunk PO-SiO_2 substrates relative to the planar PO-SiO_2 substrate. This is more than 2.5 times higher than expected due to concentrating alone. The integrated intensity of the entire DNA spots was calculated before and after shrinking on the PO-SiO_2 substrate for confirmation. A concentrating effect alone would result in the same integrated intensity value. Therefore, this additional increase in intensity is attributed to the optical effects.

Interestingly, more than a 120 fold (S.E. 5.00) increase in the fluorescence signal was observed on the shrunk PO-SiO_2 substrates relative to glass for 80-10% A_{30} ssDNA presented in Figure 6.4(a). Furthermore, heating the hybridized DNA did not appear to significantly decrease the fluorescence signal. The fluorescence signal was observed to decrease by less than 15% (S.E. 2.5%) over the different percentages of A_{30} ssDNA when comparing the hybridization signal on the heated glass slides to the signal prior to heating.

An increase in the fluorescence intensity was also coupled with a significant improvement in the signal to noise ratio (SNR) which is defined as the ratio of the average fluorescence signal minus the mean background signal to the standard deviation of the background as presented in Equation 6.3.3. [369]

$$\frac{\bar{\chi}_{ahs} - \bar{\chi}_{bg}}{\bar{\sigma}_{bg}} \qquad [6.3.3]$$

For the SNR, any value higher than 3 is generally considered to be detectable. [370] The SNR shown in Figure 6.4(b) was noted to increase by more than 46 fold on the shrunk PO-SiO_2, 1455 (S.E. 35) for 80% A_{30} ssDNA relative to the glass slide, 30.87 (S.E. 0.15). For the glass slide, the limit in the SNR was 20% A_{30} ssDNA, while on the shrunk PO-SiO_2 substrate was 0.5%. The limit in the SNR results supported the LOD results.

The enhancement in the fluorescence signal also resulted in an improvement in the detection sensitivity of the DNA microarrays. To assess the analytical detection performance of the shrunk PO-SiO_2 and glass substrates, the concentration corresponding to the limit of detection, x_{LOD}, was calculated. According to the Langmuir adsorption coefficient (K_{ads}) for DNA hybridization, a single monolayer has a value of 1.8 X 10^7 M^{-1}. [371] Equation 6.3.4 is used to convert the A_{30} ssDNA percentages into concentrations using the following relation.

$$c = \frac{\theta}{K_{ads}} \qquad [6.3.4]$$

In equation 6.3.4, K_{ads} is 1.8 X $10^7 M^{-1}$ and θ is the percent coverage of A_{30} ssDNA. This corresponds to an x_{LOD} on shrunk PO-SiO_2 of 280 pM versus an x_{LOD} 11 nM on glass. Hence, an overall 40 fold improvement in the LOD relative to a glass slide.

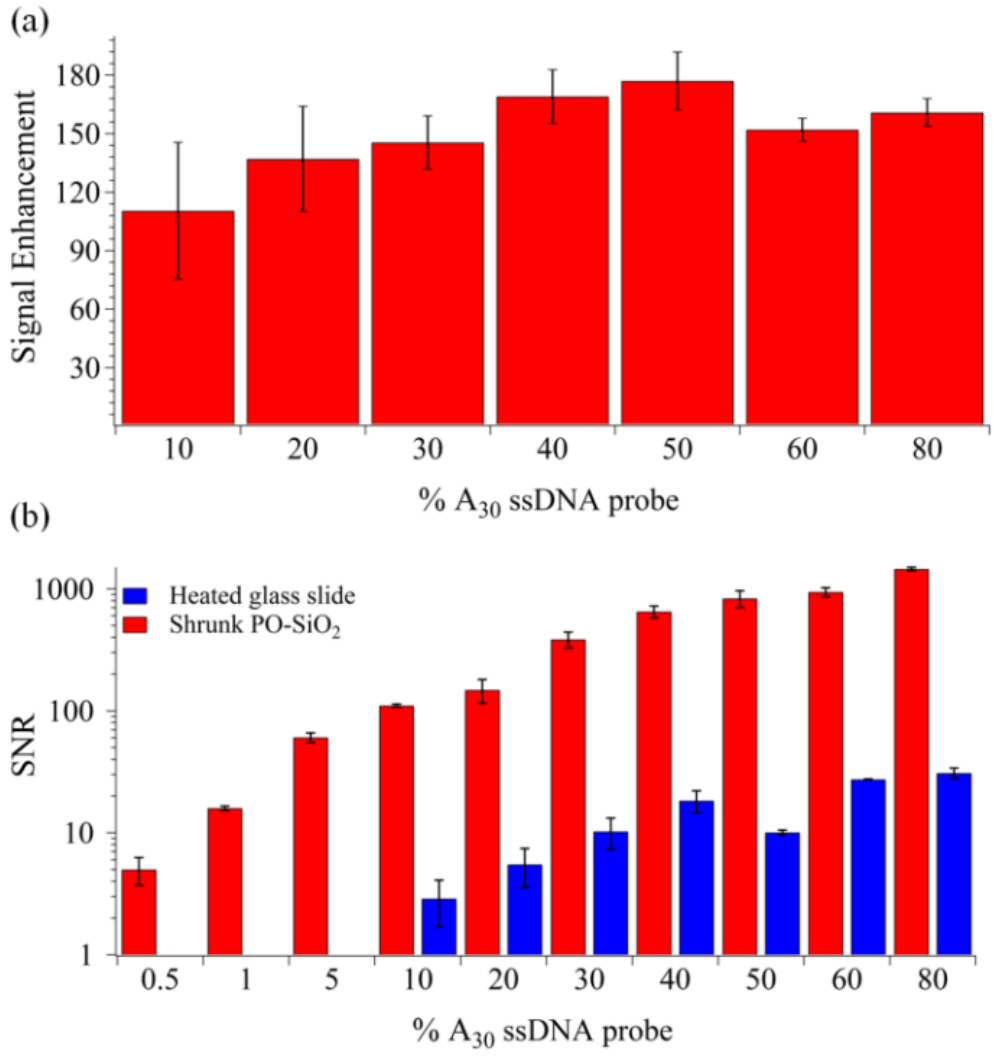

Figure 6.4. Analytical assessment of the improvement for different percentages of A_{30} ssDNA hybridized on the shrunk PO-SiO_2 substrate relative to the glass slide (a) A plot of the

fluorescence signal increase on shrunk PO-SiO_2 substrate relative to heated glass (b) SNR on heated glass slide and shrunk PO-SiO_2 substrate for the hybridized DNA at various A_{30} ssDNA percentages.

6.4 Summary

In this work, we have presented a rapid method to create DNA fluorescence microarrays using SiO_2 structures and demonstrated the ability to enhance the fluorescence signal of bound fluorophores. This demonstrates that the PO-SiO_2 substrate has higher detection sensitivity (280 pM) relative to planar glass surface (11 nM). Furthermore, a 30-45 fold improvement in the SNR was observed on the shrunk PO-SiO_2 substrate relative to a glass slide depending on the A_{30} ssDNA concentration. The fabrication of these substrates is simple, inexpensive and readily adoptable as a parallelization for microarray analysis. Furthermore, in contrast to MEF substrates, the enhanced fluorescence signals are uniform and not confined to nanometric hotspots. This ability to reach lower limits of detection suggests potential applications in DNA microarrays for earlier disease diagnostics.

Chapter 7 Summary and Future Directions

7.1 Summary

In this thesis, wrinkled structures created using three different techniques with the shrink film technology was studied. In Chapter 2, the fabrication of non-periodic (wrinkles) and periodic structures (nanopillar beads, nanotriangles) using simple top-down and bottom-up approaches were investigated. The deposition of thin metal films on heat shrink shape memory polymers achieved heterogeneous wrinkles after heating the substrate. These size of the wrinkles and gaps between them were shown to be tunable by varying the thickness of metal deposited. SEM, AFM, and EDX analysis were used to characterize the surface topology of these wrinkles. For the fabrication of the periodic structures, NSL was combined with the shrink film technology to yield periodic nanopillar bead arrays and nanotriangle arrays. The size and gaps between these particles were controlled by varying the oxygen plasma etch time and temperatures the substrates were heated to. In Chapter 3, the heterogeneous wrinkles were characterized for their optical properties in two-photon excitation. In Chapter 4, the wrinkles were evaluated for their ability to be used as biosensors by depositing fluorescently tagged antibodies onto the surface and applying methods to measure the enhancements in the fluorescence signal. In Chapter 5, the wrinkled substrates were evaluated for their ability to be used as single molecule detection sensors and characterized by combining FCS, FLIM, and two-photon microscopy. The methods presented in this section to isolate single molecules from a higher concentration of molecules would be useful to future researchers interested in similar topics. Chapter 6 introduced the idea of using highly scattering structures made by integrating SiO_2 onto shrink wrap film for applications in far-field fluorescence enhancements. The SiO_2 structures demonstrated a 40 times

improvement in the LOD relative to a glass which was accompanied by a 30-45 times improvement in the SNR.

The structures presented in this dissertation are simple to create and could serve as powerful biosensors, but require optimization before being able to leap to the next step which is to detect various types of diseases. If you just imagine for a minute, that several years from now you have a device similar to a USB stick that has our platform integrated into. The infected patient, instead of waiting for a doctor to test him can test if he has the disease at home and then record the results using a cell phone camera and if needed get the proper treatment.

7.2 Future Directions

The research presented in this dissertation has introduced the idea of using shrink wrap technology to create various structures for applications as biosensors. The results obtained from these various structures are very promising, but there are still some challenges left to overcome. The two-photon studies with the wrinkle structures yielded the highest results for the fluorescent enhancement of a single biomolecule. However, this technique is not a feasible option for developing countries because the current setup requires the use of two-photon laser microscopy which is not only bulky, but expensive. Furthermore, one of the main challenges with the wrinkled substrate is that the surfaces are hydrophobic limiting the diffusion of molecules to the surface. Recent work from our lab has shown that we can capture magnetic particles by combining ferromagnetic materials such as Ni with the shrink film technology. The composite structures presented in this dissertation are made of a combination of Ni and Au. Thus, an avenue that could be explored is to use the Ni to capture magnetic nanoparticles onto the wrinkles. The magnetic nanoparticles could be conjugated with specific bioprobes such as an antibody to bind

to antigens from the diseased patient. Then, fluorescently tagged antibodies that recognize the antigen could be added and their signal enhanced by utilizing the optical properties of the shrink film structures. This work could potentially pave the way to creating an integrated, low-cost device to trap and identify various types of biomarkers.

A slightly more cost-effective approach to the two-photon set-up would be to use the one-photon excitation setup to enhance the fluorescence signal of the labeled biomarkers. However, at this moment, the results presented are inconclusive and need extensive work done to be able to understand where the fluorescence enhancements stem from. It is unclear if the fluorescence enhancements are purely due to plasmonic effects or a collection of fluorescent molecules stuck within one area. If the former is true, then it would be important to try to determine the number of labeled molecules and apply methods such as FCS to quantify this. Recent work by Punj et. al presented some useful techniques where FCS was used to measure the autocorrelation functions and quantify the number of molecules in their system [125]. With their method, they were able to calculate the brightness per molecule and estimate the number of molecules in their system. These studies would also help elucidate better the reasons why the lifetime of the labeled biomolecules is shorter on the composite structures relative to the other substrates. Once a full understanding of the enhancements with one-photon excitation have been explored, the same magnetic capture technology proposed with two-photon microscopy can also be applied to the one-photon studies.

For the periodic structures, the nanobead pillar and nanotriangle arrays created are very interesting and hold a lot of promise for future applications as plasmonic biosensors. However, one of the main hurdles to overcome is the stiffness mismatch of the oxide layer to the shrink film which generated wrinkles during the shrinkage process. Ultimately, the wrinkles mask and

ruin any periodic structures that were initially there prior to heating. Thus, to maintain the integrity of the structures during the shrinkage process, transferring the particles over to another material that is not a shape memory polymer might be a feasible option that has not been explored. In this process, a thin coating of PVA would be applied to a glass slide and then cured to adhere the PVA. Following the curing process, PS-COOH beads would be spin coated on the glass slide and self-assembled to form the hexagonal pack. Following this process, metal can then be evaporated onto the surface. After this step, the PVA layer would be transferred over to the PO film and then dissolved in water to remove the PVA. Through this process, there should not be an extra stiffness introduced to the heat-shrink film and thus the integrity of the structures could be maintained. However, this method is suited best for the nanotriangles and not a viable option for the nanopillar bead arrays because etching into the plastic is critical for tall structures. An area that might be worth exploring for the Au nanobead pillar arrays is depositing gold nanoparticles on top and investigate if any interesting coupling effects are observed.

Perhaps the most compelling and interesting application that would be relevant for POC diagnostics is using the SiO_2 structures for far-field fluorescence enhancements. However, there are improvements that need to be made before proceeding further. Probably the most crucial one is to reduce the background of the silica substrates that limits the enhancements in the SNR. Pre-heating the noise from the unshrunk silica substrates is comparable to glass, but post-heating the noise is about 12 times higher than on glass. It is thought that the increase in the noise can be attributed to an increase in the autofluorescence of the polymer which is scattered more on the SiO_2 structures. Still, a DNA microarray can performed using the SiO_2 structures by extracting mRNA from a diseased patient and then converting the mRNA into cDNA by reverse

transcription. Following this step, the cDNA can bind to its complementary DNA strand that is fluorescently tagged and the DNA microarray can be performed.

The applications of the shrink film technology are endless and this work aimed to investigate a very small portion of them. There is strong potential for the shrink film technology to be used as way to create sensitive biosensors for disease detection.

References

1. Lanata, C.F., et al., *Global Causes of Diarrheal Disease Mortality in Children < 5 Years of Age: A Systematic Review*. PLoS One, 2013. **8**(9).
2. Fauci, A.S., N.A. Touchette, and G.K. Folkers, *Emerging infectious diseases: a 10-year perspective from the National Institute of Allergy and Infectious Diseases.* Emerging Infectious Diseases, 2005. **11**(4): p. 519-525.
3. Institute, S.L. *Diseases Go Global*. 2011; Available from: http://www.globalization101.org/diseases-go-global/.
4. Liu, L., et al., *Global, regional, and national causes of child mortality reply.* Lancet, 2012. **380**(9853): p. 1556-1557.
5. Organization, W.H. *The top 10 causes of death*. July 2013; Available from: http://www.who.int/mediacentre/factsheets/fs310/en/.
6. Folch, E., et al., *Infectious diseases, non-zero-sum thinking, and the developing world.* Am J Med Sci, 2003. **326**(2): p. 66-72.
7. Grace Wu, M.Z. (2012) *Low-cost tools for diagnosing and monitoring HIV infection in low-resource settings*. Bull World Health Organization **90**, DOI: 10.2471.
8. Sia, S.K., et al., *An integrated approach to a portable and low-cost immunoassay for resource-poor settings.* Angewandte Chemie-International Edition, 2004. **43**(4): p. 498-502.
9. Alemnji, G., J.N. Nkengasong, and B.S. Parekh, *HIV testing in developing countries: What is required?* Indian Journal of Medical Research, 2011. **134**(6): p. 779-786.
10. Lee, B.E., et al., *Use of Quantitative HIV RNA Detection for Early Diagnosis of HIV Infection in Infants and Acute HIV Infections in Alberta, Canada.* Journal of Clinical Microbiology, 2012. **50**(2): p. 502-505.
11. Rohrman, B.A., et al., *A lateral flow assay for quantitative detection of amplified HIV-1 RNA.* PLoS One, 2012. **7**(9): p. e45611.
12. Wang, J., *Electrochemical biosensors: Towards point-of-care cancer diagnostics.* Biosensors & Bioelectronics, 2006. **21**(10): p. 1887-1892.
13. Sethi, R.S., *Transducer Aspects of Biosensors (Reprinted from Gec Journal Research Vol 9, Pg 81, 1991).* Biosensors & Bioelectronics, 1994. **9**(3): p. 243-264.
14. Morgan, C.L., D.J. Newman, and C.P. Price, *Immunosensors: technology and opportunities in laboratory medicine.* Clin Chem, 1996. **42**(2): p. 193-209.
15. Pejcic, B., R.D. Marco, and G. Parkinson, *The role of biosensors in the detection of emerging infectious diseases.* Analyst, 2006. **131**(10): p. 1079-1090.
16. Scheller, F.W., et al., *Research and development in biosensors.* Curr Opin Biotechnol, 2001. **12**(1): p. 35-40.
17. Ju, H., X. Zhang, and J. Wang, *NanoBiosensing : principles, development, and application*. Biological and medical physics, biomedical engineering,. 2011, New York: Springer. xv, 586 p.
18. Reverberi, R. and L. Reverberi, *Factors affecting the antigen-antibody reaction.* Blood Transfus, 2007. **5**(4): p. 227-40.
19. Laksanasopin, T., et al., *Microfluidic Point-of-Care Diagnostics for Resource-Poor Environments.* 2009 Annual International Conference of the Ieee Engineering in Medicine and Biology Society, Vols 1-20, 2009: p. 1057-1059.

20. Grosso, P., et al., *Cancer marker detection in human serum with a point-of-care low-cost system.* Sensors and Actuators B-Chemical, 2010. **147**(2): p. 475-480.
21. Roda, A., et al., *Portable Device Based on Chemiluminescence Lensless Imaging for Personalized Diagnostics through Multiplex Bioanalysis.* Analytical Chemistry, 2011. **83**(8): p. 3178-3185.
22. Kamili, S., et al., *Laboratory Diagnostics for Hepatitis C Virus Infection.* Clinical Infectious Diseases, 2012. **55**: p. S43-S48.
23. Oh, S.W., et al., *Point-of-care fluorescence immunoassay for prostate specific antigen.* Clinica Chimica Acta, 2009. **406**(1-2): p. 18-22.
24. de la Rica, R. and M.M. Stevens, *Plasmonic ELISA for the ultrasensitive detection of disease biomarkers with the naked eye.* Nature Nanotechnology, 2012. **7**(12): p. 821-4.
25. Luch, A., *Molecular, clinical, and environmental toxicology*. Experientia supplementum. 2009, Boston: Birkhäuser. v. <1-2>.
26. Bhimji, A., et al., *Electrochemical Enzyme-Linked Immunosorbent Assay Featuring Proximal Reagent Generation: Detection of Human Immunodeficiency Virus Antibodies in Clinical Samples.* Analytical Chemistry, 2013. **85**(14): p. 6813-6819.
27. Yu, F.Y., et al., *Comparison of Enzyme-Linked Immunosorbent Assays with Chemiluminescent and Colorimetric Detection for the Determination of Ochratoxin A in Food.* Journal of Agricultural and Food Chemistry, 2011. **59**(3): p. 809-813.
28. Boucas, R.I., et al., *Development of an enzyme-linked immunosorbent assay (ELISA)-like fluorescence assay to investigate the interactions of glycosaminoglycans to cells.* Analytica Chimica Acta, 2008. **618**(2): p. 218-226.
29. Wu, X., et al., *Optofluidic laser for dual-mode sensitive biomolecular detection with a large dynamic range.* Nat Commun, 2014. **5**: p. 3779.
30. Addae, S.A., et al., *Rapid and sensitive colorimetric ELISA using silver nanoparticles, microwaves and split ring resonator structures.* Abstracts of Papers of the American Chemical Society, 2011. **241**.
31. Ricci, F., G. Adornetto, and G. Palleschi, *A review of experimental aspects of electrochemical immunosensors.* Electrochimica Acta, 2012. **84**: p. 74-83.
32. Zhong, W.W., *Nanomaterials in fluorescence-based biosensing.* Analytical and Bioanalytical Chemistry, 2009. **394**(1): p. 47-59.
33. Xie, F., et al., *Nanoscale control of Ag nanostructures for plasmonic fluorescence enhancement of near-infrared dyes.* Nano Research, 2013. **6**(7): p. 496-510.
34. Ntziachristos, V., *Fluorescence molecular imaging.* Annual review of biomedical engineering, 2006. **8**: p. 1-33.
35. Katritzky, A.R. and T. Narindoshvili, *Fluorescent amino acids: advances in protein-extrinsic fluorophores.* Organic & Biomolecular Chemistry, 2009. **7**(4): p. 627-634.
36. Wu, Z., et al., *Well-Defined Nanoclusters as Fluorescent Nanosensors: A Case Study on Au25(SG)18.* Small, 2012. **8**(13): p. 2028-2035.
37. Swierczewska, M., et al., *High-sensitivity nanosensors for biomarker detection.* Chem Soc Rev, 2012. **41**(7): p. 2641-55.
38. Resch-Genger, U., et al., *Quantum dots versus organic dyes as fluorescent labels.* Nature Methods, 2008. **5**(9): p. 763-775.

39. Feng, W., X.J. Zhu, and F.Y. Li, *Recent advances in the optimization and functionalization of upconversion nanomaterials for in vivo bioapplications.* Npg Asia Materials, 2013. **5**.
40. Sharma, P., et al., *Nanoparticles for bioimaging.* Advances in Colloid and Interface Science, 2006. **123**: p. 471-485.
41. Sokolov, I. and D.O. Volkov, *Ultrabright fluorescent mesoporous silica particles.* Journal of Materials Chemistry, 2010. **20**(21): p. 4247-4250.
42. Sauer, M., J. Hofkens, and J. Enderlein, *Handbook of fluorescence spectroscopy and imaging : from single molecules to ensembles*. 2011, Weinheim: Wiley-VCH. ix, 281 p.
43. Klonoff, D.C., *Overview of fluorescence glucose sensing: a technology with a bright future.* J Diabetes Sci Technol, 2012. **6**(6): p. 1242-50.
44. Altman, R.B., et al., *Cyanine fluorophore derivatives with enhanced photostability.* Nat Methods, 2012. **9**(1): p. 68-71.
45. Zhang, J., et al., *Metal-Enhanced Fluoroimmunoassay on a Silver Film by Vapor Deposition.* The Journal of Physical Chemistry B, 2005. **109**(16): p. 7969-7975.
46. Zhang, J. and J.R. Lakowicz, *Metal-enhanced fluorescence of an organic fluorophore using gold particles.* Opt Express, 2007. **15**(5): p. 2598-606.
47. Sokolov, K., G. Chumanov, and T.M. Cotton, *Enhancement of molecular fluorescence near the surface of colloidal metal films.* Anal Chem, 1998. **70**(18): p. 3898-905.
48. Deng, W. and E.M. Goldys, *Plasmonic approach to enhanced fluorescence for applications in biotechnology and the life sciences.* Langmuir, 2012. **28**(27): p. 10152-63.
49. Dong, J., et al., *Surface enhanced fluorescence on three dimensional silver nanostructure substrate.* Journal of Applied Physics, 2012. **111**(9): p. 093101.
50. Cui, X., et al., *Enhanced Fluorescence Microscopic Imaging by Plasmonic Nanostructures: From a 1D Grating to a 2D Nanohole Array.* Advanced Functional Materials, 2010. **20**(6): p. 945-950.
51. Choudhury, S.D., et al., *Silver-Gold Nanocomposite Substrates for Metal-Enhanced Fluorescence: Ensemble and Single-Molecule Spectroscopic Studies.* J Phys Chem C Nanomater Interfaces, 2012. **116**(8): p. 5042-5048.
52. Teng, Y., et al., *Surface plasmon-enhanced molecular fluorescence induced by gold nanostructures.* Annalen der Physik, 2012: p. n/a-n/a.
53. Pompa, P.P., et al., *Metal-enhanced fluorescence of colloidal nanocrystals with nanoscale control.* Nat Nanotechnol, 2006. **1**(2): p. 126-30.
54. Iqbal, P., J.A. Preece, and P.M. Mendes, *Nanotechnology: The "Top-Down" and "Bottom-Up" Approaches*, in *Supramolecular Chemistry*. 2012, John Wiley & Sons, Ltd.
55. Villiers, M.M.d., P. Aramwit, and G.S. Kwon, *Nanotechnology in drug delivery*. Biotechnology : pharmaceutical aspects. 2009, New York, NY: Springer : AAPS Press. xiii, 662 p., 18 p. of plates.
56. Allhoff, F., P. Lin, and D. Moore, *What is nanotechnology and why does it matter? : from science to ethics*. 2010, Chichester, UK ; Malden, MA: Wiley- Blackwell. x, 293 p.
57. Biswas, A., et al., *Advances in top-down and bottom-up surface nanofabrication: Techniques, applications & future prospects.* Advances in Colloid and Interface Science, 2012. **170**(1-2): p. 2-27.
58. Bhushan, B., *Springer handbook of nanotechnology*. 2004, Berlin ; New York: Springer. xxxvi, 1222 p.

59. Yao, N. and Z.L. Wang, *Handbook of microscopy for nanotechnology*. 2005, Boston: Kluwer Academic Publishers. xx, 731 p.
60. Thompson, L.F., et al., *Introduction to microlithography : theory, materials, and processing*. ACS symposium series,. 1983, Washington, D.C.: The Society. ix, 363 p.
61. Ratner, B.D., *Biomaterials science : an introduction to materials in medicine*. 2nd ed. 2004, Amsterdam ; Boston: Elsevier Academic Press. xii, 851 p.
62. Rahman, F., *Nanostructures in electronics and photonics*. 2008, Singapore: Pan Stanford Pub. xii, 302 p.
63. Zhou, W., *Nanoimprint lithography : an enabling process for nanofabrication*. 2012, New York: Springer.
64. Gonis, A., N. Kioussis, and M. Ciftan, *Electron correlations and materials properties 2*. 2003, New York: Kluwer Academic/Plenum Publishers. x, 418 p.
65. Mendelson, M.I., *Learning bio-micro-nanotechnology*. 2013, Boca Raton: CRC Press. xxix, 581 p.
66. Song, Y. and D. Zhu, *High density data storage : principle, technology, and materials*. 2009, Singapore ; Hackensack, NJ: World Scientific. vii, 263 p.
67. Cai, W. and V.M. Shalaev, *Optical metamaterials : fundamentals and applications*. 2010, New York: Springer. xii, 200 p.
68. Giannuzzi, L.A. and F.A. Stevie, *Introduction to focused ion beams : instrumentation, theory, techniques, and practice*. 2005, New York: Springer. xiv, 357 p.
69. Geddes, C.D., et al., *Silver fractal-like structures for metal-enhanced fluorescence: Enhanced fluorescence intensities and increased probe photostabilities.* Journal of Fluorescence, 2003. **13**(3): p. 267-276.
70. Zhang, L., et al., *Wrinkled Nanoporous Gold Films with Ultrahigh Surface-Enhanced Raman Scattering Enhancement.* Acs Nano, 2011. **5**(6): p. 4407-4413.
71. Wenger, J., et al., *Emission and excitation contributions to enhanced single molecule fluorescence by gold nanometric apertures.* Optics Express, 2008. **16**(5): p. 3008-3020.
72. Yang, B., et al., *Tuning the intensity of metal-enhanced fluorescence by engineering silver nanoparticle arrays.* Small, 2010. **6**(9): p. 1038-43.
73. Akashi, N., et al., *Application of Grating Substrate Fabricated by Nanoimprint Lithography to Surface Plasmon Field-Enhanced Fluorescence Microscopy and Study of Its Optimum Structure.* Japanese Journal of Applied Physics, 2009. **48**(6).
74. Shibata, T., et al., *Optimization of Metal Quality for Grating Coupled Surface Plasmon Resonance.* Physics Procedia, 2013. **48**(0): p. 179-183.
75. Corrigan, T.D., et al., *Enhanced fluorescence from periodic arrays of silver nanoparticles.* Journal of Fluorescence, 2005. **15**(5): p. 777-784.
76. Hu, J.L., et al., *Recent advances in shape-memory polymers: Structure, mechanism, functionality, modeling and applications.* Progress in Polymer Science, 2012. **37**(12): p. 1720-1763.
77. Shahinpoor, M. and H.-J. Schneider, *Intelligent materials*. 2008, Cambridge: RSC Publishing. xix, 532 p.
78. Sharma, H., et al., *Unconventional Low-Cost Fabrication and Patterning Techniques for Point of Care Diagnostics.* Annals of Biomedical Engineering, 2011. **39**(4): p. 1313-1327.

79. Zhao, Y., W.M. Huang, and Y.Q. Fu, *Formation of micro/nano-scale wrinkling patterns atop shape memory polymers.* Journal of Micromechanics and Microengineering, 2011. **21**(6).
80. Fu, C.C., et al., *Tunable Nanowrinkles on Shape Memory Polymer Sheets.* Advanced Materials, 2009. **21**(44): p. 4472-+.
81. Huntington, M.D., et al., *Polymer Nanowrinkles with Continuously Tunable Wavelengths.* Acs Applied Materials & Interfaces, 2013. **5**(13): p. 6438-6442.
82. Fu, C.C., et al., *Bimetallic nanopetals for thousand-fold fluorescence enhancements.* Applied Physics Letters, 2010. **97**(20).
83. Nguyen, D., et al., *Better shrinkage than Shrinky-Dinks.* Lab on a Chip, 2010. **10**(12): p. 1623-1626.
84. Gabardo, C.M., et al., *Bench-Top Fabrication of Hierarchically Structured High-Surface-Area Electrodes.* Advanced Functional Materials, 2013. **23**(24): p. 3030-3039.
85. Freschauf, L.R., et al., *Shrink-Induced Superhydrophobic and Antibacterial Surfaces in Consumer Plastics.* Plos One, 2012. **7**(8).
86. Ferri, C.G.L., et al., *Plasmon-induced enhancement of intra-ensemble FRET in quantum dots on wrinkled thin films.* Optical Materials Express, 2013. **3**(3): p. 383-389.
87. Pegan, J.D., et al., *Flexible shrink-induced high surface area electrodes for electrochemiluminescent sensing.* Lab on a Chip, 2013. **13**(21): p. 4205-4209.
88. Nawarathna, D., et al., *Shrink-induced sorting using integrated nanoscale magnetic traps.* Applied Physics Letters, 2013. **102**(6).
89. Jayadev, S., et al., *Adaptive wettability-enhanced surfaces ordered on molded etched substrates using shrink film.* Smart Materials and Structures, 2013. **22**(1).
90. Liu, H.W., et al., *Single molecule detection from a large-scale SERS-active Au79Ag21 substrate.* Scientific Reports, 2011. **1**.
91. Chen, A., et al., *Integrated platform for functional monitoring of biomimetic heart sheets derived from human pluripotent stem cells.* Biomaterials, 2014. **35**(2): p. 675-683.
92. Chen, A., et al., *Shrink-Film Configurable Multiscale Wrinkles for Functional Alignment of Human Embryonic Stem Cells and their Cardiac Derivatives.* Advanced Materials, 2011. **23**(48): p. 5785-+.
93. Li, Y.Y., et al., *Superhydrophobic Surfaces from Hierarchically Structured Wrinkled Polymers.* Acs Applied Materials & Interfaces, 2013. **5**(21): p. 11066-11073.
94. Brundle, C.R., C.A. Evans, and S. Wilson, *Encyclopedia of materials characterization : surfaces, interfaces, thin films*. Materials characterization series. 1992, Boston Greenwich, CT: Butterworth-Heinemann ;Manning. xix, 751 p.
95. De Angelis, F., et al., *Breaking the diffusion limit with super-hydrophobic delivery of molecules to plasmonic nanofocusing SERS structures.* Nat Photon, 2011. **5**(11): p. 682-687.
96. Scopelliti, P.E., et al., *The effect of surface nanometre-scale morphology on protein adsorption.* PLoS One, 2010. **5**(7): p. e11862.
97. Dolatshahi-Pirouz, A., et al., *Bovine serum albumin adsorption on nano-rough platinum surfaces studied by QCM-D.* Colloids Surf B Biointerfaces, 2008. **66**(1): p. 53-9.
98. Mahmoudi, M. and V. Serpooshan, *Large Protein Absorptions from Small Changes on the Surface of Nanoparticles.* The Journal of Physical Chemistry C, 2011. **115**(37): p. 18275-18283.

99. Shu, D., et al., *Bottom-up assembly of RNA arrays and superstructures as potential parts in nanotechnology*. Nano Letters, 2004. **4**(9): p. 1717-1723.
100. Cao, G., *Nanostructures & nanomaterials : synthesis, properties & applications*. 2004, London ; Hackensack, NJ: Imperial College Press. xiv, 433 p.
101. Jana, N.R., L. Gearheart, and C.J. Murphy, *Wet chemical synthesis of high aspect ratio cylindrical gold nanorods.* Journal of Physical Chemistry B, 2001. **105**(19): p. 4065-4067.
102. Adato, R., et al., *Radiative engineering of plasmon lifetimes in embedded nanoantenna arrays.* Optics Express, 2010. **18**(5): p. 4526-4537.
103. Pieranski, P., *Two-Dimensional Interfacial Colloidal Crystals.* Physical Review Letters, 1980. **45**(7): p. 569-572.
104. Fischer, U.C. and H.P. Zingsheim, *Submicroscopic pattern replication with visible light.* Journal of Vacuum Science & Technology, 1981. **19**(4): p. 881-885.
105. Deckman, H.W. and J.H. Dunsmuir, *Natural Lithography.* Applied Physics Letters, 1982. **41**(4): p. 377-379.
106. Hulteen, J.C. and R.P. Vanduyne, *Nanosphere Lithography - a Materials General Fabrication Process for Periodic Particle Array Surfaces.* Journal of Vacuum Science & Technology a-Vacuum Surfaces and Films, 1995. **13**(3): p. 1553-1558.
107. Ye, X.Z. and L.M. Qi, *Two-dimensionally patterned nanostructures based on monolayer colloidal crystals: Controllable fabrication, assembly, and applications.* Nano Today, 2011. **6**(6): p. 608-631.
108. Binks, B.P. and T.S. Horozov, *Colloidal particles at liquid interfaces*. 2006, Cambridge ; New York: Cambridge University Press. xiii, 503 p.
109. Yong-Hong, Y., et al., *Self-assembling three-dimensional colloidal photonic crystal structure with high crystalline quality.* Applied Physics Letters, 2001. **78**(1): p. 52-54.
110. Claire, S.S. and N. Ioan, *Combined atomic force microscopy-Raman mapping of electric field enhancement and surface-enhanced Raman scattering hot-spots for nanosphere lithography substrates.* Journal of Nanophotonics, 2011. **5**: p. 059504.
111. Kralchevsky, P.A. and N.D. Denkov, *Capillary forces and structuring in layers of colloid particles.* Current Opinion in Colloid & Interface Science, 2001. **6**(4): p. 383-401.
112. Nagao, D., et al., *Multiformity of particle arrays assembled with a simple dip-coating.* Colloids and Surfaces a-Physicochemical and Engineering Aspects, 2007. **311**(1-3): p. 26-31.
113. Colson, P., C. Henrist, and R. Cloots, *Nanosphere Lithography: A Powerful Method for the Controlled Manufacturing of Nanomaterials.* Journal of Nanomaterials, 2013.
114. Rehg, T.J. and B.G. Higgins, *Spin Coating of Colloidal Suspensions.* Aiche Journal, 1992. **38**(4): p. 489-501.
115. Dushkin, C.D., et al., *Effect of growth conditions on the structure of two-dimensional latex crystals: experiment.* Colloid and Polymer Science, 1999. **277**(10): p. 914-930.
116. Xi, J.Q., et al., *Optical thin-film materials with low refractive index for broadband elimination of Fresnel reflection.* Nature Photonics, 2007. **1**(3): p. 176-179.
117. Maier, S.A., *Plasmonics: Metal nanostructures for subwavelength photonic devices.* Ieee Journal of Selected Topics in Quantum Electronics, 2006. **12**(6): p. 1214-1220.
118. Ozbay, E., *Plasmonics: Merging photonics and electronics at nanoscale dimensions.* Science, 2006. **311**(5758): p. 189-193.

119. Anker, J.N., et al., *Biosensing with plasmonic nanosensors.* Nature Materials, 2008. **7**(6): p. 442-453.
120. Huang, X.H., S. Neretina, and M.A. El-Sayed, *Gold Nanorods: From Synthesis and Properties to Biological and Biomedical Applications.* Advanced Materials, 2009. **21**(48): p. 4880-4910.
121. Atwater, H.A. and A. Polman, *Plasmonics for improved photovoltaic devices.* Nature Materials, 2010. **9**(3): p. 205-213.
122. Lee, S.J., et al., *Surface-enhanced Raman spectroscopy and nanogeometry: The plasmonic origin of SERS.* Journal of Physical Chemistry C, 2007. **111**(49): p. 17985-17988.
123. Aslan, K., et al., *Metal-enhanced fluorescence: an emerging tool in biotechnology.* Current Opinion in Biotechnology, 2005. **16**(1): p. 55-62.
124. Lim, D.K., et al., *Nanogap-engineerable Raman-active nanodumbbells for single-molecule detection.* Nature Materials, 2010. **9**(1): p. 60-67.
125. Punj, D., et al., *A plasmonic 'antenna-in-box' platform for enhanced single-molecule analysis at micromolar concentrations.* Nature Nanotechnology, 2013. **8**(7): p. 512-516.
126. Zheng, Y.B., et al., *Chemically Tuning the Localized Surface Plasmon Resonances of Gold Nanostructure Arrays.* Journal of Physical Chemistry C, 2009. **113**(17): p. 7019-7024.
127. Caldwell, J.D., et al., *Plasmonic Nanopillar Arrays for Large-Area, High-Enhancement Surface-Enhanced Raman Scattering Sensors.* Acs Nano, 2011. **5**(5): p. 4046-4055.
128. Vieu, C., et al., *Electron beam lithography: resolution limits and applications.* Applied Surface Science, 2000. **164**: p. 111-117.
129. Deckman, H.W. and J.H. Dunsmuir, *Applications of Surface Textures Produced with Natural Lithography.* Journal of Vacuum Science & Technology B, 1983. **1**(4): p. 1109-1112.
130. Kuo, C.W., et al., *Fabrication of size-tunable large-area periodic silicon nanopillar arrays with sub-10-nm resolution.* Journal of Physical Chemistry B, 2003. **107**(37): p. 9950-9953.
131. Cheung, C., Nikolic, R., *Fabrication of nanopillars by nanosphere lithography.* Nanotechnology, 2006. **17**(5).
132. Sainiemi, L., Keskinen, H., Aromaa, M., *Rapid fabrication of high aspect ratio silicon nanopillars.* Nanotechnology, 2007. **18**(50).
133. Valsesia, A., Meziani, T., *Plasma assisted production of chemical nano-patterns by nano-sphere lithography: application to bio-interfaces* Journal of Physics D: Applied Physics, 2007. **40**(8).
134. Wu, L.Y., et al., *Bioinspired nanocorals with decoupled cellular targeting and sensing functionality.* Small, 2010. **6**(4): p. 503-7.
135. He, L., et al., *Silver nanosheet-coated inverse opal film as a highly active and uniform SERS substrate.* Journal of Materials Chemistry, 2011.
136. Caldwell, J.D., et al., *Large-area plasmonic hot-spot arrays: sub-2 nm interparticle separations with plasma-enhanced atomic layer deposition of Ag on periodic arrays of Si nanopillars.* Opt. Express, 2011. **19**(27): p. 26056-26064.
137. Knoben, W., S.H. Brongersma, and M. Crego-Calama, *Plasmonic Au islands on polymer nanopillars.* Nanotechnology, 2011. **22**(29): p. 295303.

138. Paivanranta, B., et al., *High Aspect Ratio Plasmonic Nanostructures for Sensing Applications.* Acs Nano, 2011. **5**(8): p. 6374-6382.
139. Galarreta, B.C., P.R. Norton, and F. Lagugne-Labarthet, *Hexagonal Array of Gold Nanotriangles: Modeling the Electric Field Distribution.* Journal of Physical Chemistry C, 2010. **114**(47): p. 19952-19957.
140. Kazemi-Zanjani, N., S. Vedraine, and F. Lagugne-Labarthet, *Localized enhancement of electric field in tip-enhanced Raman spectroscopy using radially and linearly polarized light.* Optics Express, 2013. **21**(21): p. 25271-25276.
141. Pan, Z.Y. and J.P. Guo, *Enhanced optical absorption and electric field resonance in diabolo metal bar optical antennas.* Optics Express, 2013. **21**(26): p. 32491-32500.
142. Fayyaz, S., et al., *Surface-Enhanced Fluorescence: Mapping Individual Hot Spots in Silica-Protected 2D Gold Nanotriangle Arrays.* Journal of Physical Chemistry C, 2012. **116**(21): p. 11665-11670.
143. Haes, A.J., et al., *Nanoscale optical biosensor: Short range distance dependence of the localized surface plasmon resonance of noble metal nanoparticles.* Journal of Physical Chemistry B, 2004. **108**(22): p. 6961-6968.
144. Lohmuller, T., et al., *Single Molecule Tracking on Supported Membranes with Arrays of Optical Nanoantennas.* Nano Letters, 2012. **12**(3): p. 1717-1721.
145. Dai, Z.G., et al., *Large-area, well-ordered, uniform-sized bowtie nanoantenna arrays for surface enhanced Raman scattering substrate with ultra-sensitive detection.* Applied Physics Letters, 2013. **103**(4).
146. Hennemann, L.E., et al., *Assessing the plasmonics of gold nano-triangles with higher order laser modes.* Beilstein Journal of Nanotechnology, 2012. **3**: p. 674-683.
147. Haynes, C.L. and R.P. Van Duyne, *Nanosphere lithography: A versatile nanofabrication tool for studies of size-dependent nanoparticle optics.* Journal of Physical Chemistry B, 2001. **105**(24): p. 5599-5611.
148. Morarescu, R., et al., *Exploiting the localized surface plasmon modes in gold triangular nanoparticles for sensing applications.* Journal of Materials Chemistry, 2012. **22**(23): p. 11537-11542.
149. Tabatabaei, M., et al., *Optical Properties of Silver and Gold Tetrahedral Nanopyramid Arrays Prepared by Nanosphere Lithography.* Journal of Physical Chemistry C, 2013. **117**(28): p. 14778-14786.
150. Cho, S.H. and S. Krishnan, *Cancer nanotechnology : principles and applications in radiation oncology*. Imaging in medical diagnosis and therapy. 2013, Boca Raton, FL: CRC Press. xviii, 254 p., 12 p. of plates.
151. Wiederrecht, G.P., *Handbook of nanoscale optics and electronics*. 1st ed. 2010, Amsterdam ; Boston: Elsevier. xi, 387 p.
152. Avrutsky, I., *Surface plasmons at nanoscale relief gratings between a metal and a dielectric medium with optical gain.* Physical Review B, 2004. **70**(15).
153. Robertson, W.M. and M.S. May, *Surface electromagnetic wave excitation on one-dimensional photonic band-gap arrays.* Applied Physics Letters, 1999. **74**(13): p. 1800-1802.
154. Parsons, J. and A. Polman, *A copper negative index metamaterial in the visible/near-infrared.* Applied Physics Letters, 2011. **99**(16).

155. *Metallic films for electronic, optical and magnetic applications : structure, processing and properties*. Woodhead publishing series in electronic and optical materials. pages cm.
156. Maity, N.P.M.a.R., *Surface Plasmon Waves on noble metals at Optical Wavelengths* International Journal of Computer Science Issues, 2011. **8**(3): p. 1694-0814.
157. Novotny, L. and B. Hecht, *Principles of nano-optics*. 2006, Cambridge ; New York: Cambridge University Press. xvii, 539 p.
158. Nalwa, H.S., *Handbook of advanced electronic and photonic materials and devices*. 2001, San Diego, CA: Academic Press.
159. Wang, H.F., et al., *In vitro and in vivo two-photon luminescence imaging of single gold nanorods.* Proceedings of the National Academy of Sciences of the United States of America, 2005. **102**(44): p. 15752-15756.
160. Bouhelier, A., M.R. Beversluis, and L. Novotny, *Characterization of nanoplasmonic structures by locally excited photoluminescence.* Applied Physics Letters, 2003. **83**(24): p. 5041-5043.
161. Beversluis, M.R., A. Bouhelier, and L. Novotny, *Continuum generation from single gold nanostructures through near-field mediated intraband transitions.* Physical Review B, 2003. **68**(11).
162. Campion, A. and P. Kambhampati, *Surface-enhanced Raman scattering.* Chemical Society Reviews, 1998. **27**(4): p. 241-250.
163. Sarid, D. and W.A. Challener, *Modern introduction to surface plasmons : theory, Mathematica modeling, and applications*. 2010, Cambridge ; New York: Cambridge University Press. xiv, 371 p.
164. Zayats, A.V. and I.I. Smolyaninov, *Near-field photonics: surface plasmon polaritons and localized surface plasmons* Journal of Optics A: Pure and Applied Optics, 2003. **5**(4).
165. Willets, K.A. and R.P. Van Duyne, *Localized surface plasmon resonance spectroscopy and sensing.* Annual Review of Physical Chemistry, 2007. **58**: p. 267-297.
166. Grubisic, A., et al., *Plasmonic Near-Electric Field Enhancement Effects in Ultrafast Photoelectron Emission: Correlated Spatial and Laser Polarization Microscopy Studies of Individual Ag Nanocubes.* Nano Letters, 2012. **12**(9): p. 4823-4829.
167. Hu, M., et al., *Gold nanostructures: engineering their plasmonic properties for biomedical applications.* Chemical Society Reviews, 2006. **35**(11): p. 1084-1094.
168. Ghosh, S.K. and T. Pal, *Interparticle coupling effect on the surface plasmon resonance of gold nanoparticles: From theory to applications.* Chemical Reviews, 2007. **107**(11): p. 4797-4862.
169. Catchpole, K.R. and A. Polman, *Plasmonic solar cells.* Opt Express, 2008. **16**(26): p. 21793-800.
170. Katrin, K., *Surface-Enhanced Raman Scattering.* Physics Today, 2007. **60**(11): p. 40-46.
171. Burrows, C.P. and W.L. Barnes, *Large spectral extinction due to overlap of dipolar and quadrupolar plasmonic modes of metallic nanoparticles in arrays.* Opt. Express, 2010. **18**(3): p. 3187-3198.
172. Meier, M. and A. Wokaun, *Enhanced fields on large metal particles: dynamic depolarization.* Opt Lett, 1983. **8**(11): p. 581-3.
173. Stiles, P.L., et al., *Surface-enhanced Raman spectroscopy.* Annu Rev Anal Chem (Palo Alto Calif), 2008. **1**: p. 601-26.

174. Ghosh, S.K. and T. Pal, *Interparticle coupling effect on the surface plasmon resonance of gold nanoparticles: from theory to applications.* Chem Rev, 2007. **107**(11): p. 4797-862.
175. Guo, H., et al., *Correlating the Shape, Surface Plasmon Resonance, and Surface-Enhanced Raman Scattering of Gold Nanorods.* The Journal of Physical Chemistry C, 2009. **113**(24): p. 10459-10464.
176. Zijlstra, P., J.W. Chon, and M. Gu, *Five-dimensional optical recording mediated by surface plasmons in gold nanorods.* Nature, 2009. **459**(7245): p. 410-3.
177. Park, S., et al., *Ultrafast Resonant Dynamics of Surface Plasmons in Gold Nanorods.* The Journal of Physical Chemistry C, 2006. **111**(1): p. 116-123.
178. McLellan, J.M., et al., *The SERS activity of a supported Ag nanocube strongly depends on its orientation relative to laser polarization.* Nano Lett, 2007. **7**(4): p. 1013-7.
179. Nau, D., et al., *Hydrogen sensor based on metallic photonic crystal slabs.* Opt Lett, 2010. **35**(18): p. 3150-2.
180. Novo, C., et al., *Influence of the Medium Refractive Index on the Optical Properties of Single Gold Triangular Prisms on a Substrate.* The Journal of Physical Chemistry C, 2007. **112**(1): p. 3-7.
181. Millstone, J.E., et al., *Observation of a quadrupole plasmon mode for a colloidal solution of gold nanoprisms.* J Am Chem Soc, 2005. **127**(15): p. 5312-3.
182. Sau, T.K., et al., *Properties and applications of colloidal nonspherical noble metal nanoparticles.* Adv Mater, 2010. **22**(16): p. 1805-25.
183. Jameson, D.M., *Introduction to fluorescence*. xvii, 295 pages.
184. Mason, W.T., *Fluorescent and luminescent probes for biological activity : a practical guide to technology for quantitative real-time analysis*. 2nd ed. Biological techniques. 1999, San Diego, Calif.: Academic Press. xxv, 647 p.
185. Luo, Q., China. Jiao yu bu. Key Laboratory of Biomedical Photonics., and Society of Photo-optical Instrumentation Engineers., *Third International Conference on Photonics and Imaging in Biology and Medicine : 8-11 June 2003, Wuhan, China*. Progress in biomedical optics and imaging,. 2003, Bellingham, Wash., USA: SPIE. xii, 596 p.
186. Geddes, C.D., et al., *Metal-enhanced fluorescence: potential applications in HTS.* Comb Chem High Throughput Screen, 2003. **6**(2): p. 109-17.
187. Prasad, P.N., *Introduction to biophotonics*. 2003, Hoboken, NJ: Wiley-Interscience. xvii, 593 p., 8 p. of plates.
188. Elder, A., S. Schlachter, and C.F. Kaminski, *Theoretical investigation of the photon efficiency in frequency-domain fluorescence lifetime imaging microscopy.* J Opt Soc Am A Opt Image Sci Vis, 2008. **25**(2): p. 452-62.
189. Boens, N., et al., *Fluorescence lifetime standards for time and frequency domain fluorescence spectroscopy.* Anal Chem, 2007. **79**(5): p. 2137-49.
190. Colyer, R.A., C. Lee, and E. Gratton, *A novel fluorescence lifetime imaging system that optimizes photon efficiency.* Microscopy Research and Technique, 2008. **71**(3): p. 201-213.
191. Digman, M.A., et al., *The phasor approach to fluorescence lifetime imaging analysis.* Biophys J, 2008. **94**(2): p. L14-6.
192. Rubart, M., *Two-Photon Microscopy of Cells and Tissue.* Circulation Research, 2004. **95**(12): p. 1154-1166.
193. Australia, U.o.W. *Two photo microscopy*. OBEL 2012.

194. Masters, B.R., *Confocal microscopy and multiphoton excitation microscopy : the genesis of live cell imaging*. 2006, Bellingham, Wash.: SPIE Press. xix, 208 p.
195. Vo-Dinh, T., *Biomedical photonics handbook*. 2003, Boca Raton, Fla.: CRC Press.
196. Grzybowski, A. and K. Pietrzak, *Maria Goeppert-Mayer (1906-1972): two-photon effect on dermatology.* Clin Dermatol, 2013. **31**(2): p. 221-5.
197. Göppert-Mayer, M., *Über Elementarakte mit zwei Quantensprüngen.* Annalen der Physik, 1931. **401**(3): p. 273-294.
198. Kaiser, W. and C.G.B. Garrett, *Two-Photon Excitation in CaF_{2}: Eu^{2+}.* Physical Review Letters, 1961. **7**(6): p. 229-231.
199. Denk, W., J.H. Strickler, and W.W. Webb, *Two-photon laser scanning fluorescence microscopy.* Science, 1990. **248**(4951): p. 73-6.
200. Hopt, A. and E. Neher, *Highly nonlinear photodamage in two-photon fluorescence microscopy.* Biophys J, 2001. **80**(4): p. 2029-36.
201. Soeller, C. and M.B. Cannell, *Two-photon microscopy: imaging in scattering samples and three-dimensionally resolved flash photolysis.* Microsc Res Tech, 1999. **47**(3): p. 182-95.
202. Dittrich, P.S. and P. Schwille, *Photobleaching and stabilization of. fluorophores used for single-molecule analysis. with one- and two-photon excitation.* Applied Physics B: Lasers and Optics, 2001. **73**(8): p. 829-837.
203. Deng, W., et al., *Metal-enhanced fluorescence in the life sciences: here, now and beyond.* Physical Chemistry Chemical Physics, 2013. **15**(38): p. 15695-15708.
204. Purcell, E.M., *Spontaneous Emission Probabilities at Radio Frequencies.* Physical Review, 1946. **69**(11-1): p. 681-681.
205. Drexhage, K.H., *Influence of a Dielectric Interface on Fluorescence Decay Time.* Bulletin of the American Physical Society, 1969. **14**(8): p. 873-&.
206. Demartini, F., et al., *Anomalous Spontaneous Emission Time in a Microscopic Optical Cavity.* Physical Review Letters, 1987. **59**(26): p. 2955-2958.
207. Yokoyama, H., et al., *Controlling Spontaneous Emission and Threshold-Less Laser Oscillation with Optical Microcavities.* Optical and Quantum Electronics, 1992. **24**(2): p. S245-S272.
208. Lakowicz, J.R., et al., *Radiative decay engineering 2. Effects of silver island films on fluorescence intensity, lifetimes, and resonance energy transfer.* Analytical Biochemistry, 2002. **301**(2): p. 261-277.
209. Fu, Y., J. Zhang, and J.R. Lakowicz, *Plasmonic enhancement of single-molecule fluorescence near a silver nanoparticle.* J Fluoresc, 2007. **17**(6): p. 811-6.
210. Ruppin, R., *Decay of an Excited Molecule near a Small Metal Sphere.* Journal of Chemical Physics, 1982. **76**(4): p. 1681-1684.
211. Estrada, L.C., et al., *Detection of low quantum yield fluorophores and improved imaging times using metallic nanoparticles.* J Phys Chem B, 2012. **116**(7): p. 2306-13.
212. Barnes, W.L., *Surface plasmon-polariton length scales: a route to sub-wavelength optics.* Journal of Optics a-Pure and Applied Optics, 2006. **8**(4): p. S87-S93.
213. Barnes, W.L., *Fluorescence near interfaces: the role of photonic mode density.* Journal of Modern Optics, 1998. **45**(4): p. 661-699.
214. Novotny, L., R.X. Bian, and X.S. Xie, *Theory of nanometric optical tweezers.* Physical Review Letters, 1997. **79**(4): p. 645-648.

215. Uetsuki, K., et al., *Tunable plasmon resonances in a metallic nanotip-film system.* Nanoscale, 2012. **4**(19): p. 5931-5.
216. Lindquist, N.C., et al., *Plasmonic nanofocusing with a metallic pyramid and an integrated C-shaped aperture.* Sci Rep, 2013. **3**: p. 1857.
217. Ray, K., R. Badugu, and J.R. Lakowicz, *Distance-dependent metal-enhanced fluorescence from Langmuir-Blodgett monolayers of alkyl-NBD derivatives on silver island films.* Langmuir, 2006. **22**(20): p. 8374-8.
218. Ray, K., R. Badugu, and J.R. Lakowicz, *Polyelectrolyte Layer-by-Layer Assembly To Control the Distance between Fluorophores and Plasmonic Nanostructures.* Chemistry of Materials, 2007. **19**(24): p. 5902-5909.
219. Aslan, K., et al., *Metal-enhanced fluorescence: an emerging tool in biotechnology.* Curr Opin Biotechnol, 2005. **16**(1): p. 55-62.
220. Chen, Y., K. Munechika, and D.S. Ginger, *Dependence of Fluorescence Intensity on the Spectral Overlap between Fluorophores and Plasmon Resonant Single Silver Nanoparticles.* Nano Letters, 2007. **7**(3): p. 690-696.
221. Yongxia, Z., D. Anatoliy, and D.G. Chris, *Metal-enhanced fluorescence from tin nanostructured surfaces.* Journal of Applied Physics, 2010. **107**(2): p. 024302.
222. Aslan, K. and C.D. Geddes, *Microwave-Accelerated and Metal-Enhanced Fluorescence Myoglobin Detection on Silvered Surfaces: Potential Application to Myocardial Infarction Diagnosis.* Plasmonics, 2006. **1**(1): p. 53-59.
223. Parfenov, A., et al., *Enhanced Fluorescence from Fluorophores on Fractal Silver Surfaces.* J Phys Chem B, 2003. **107**(34): p. 8829-8833.
224. Matveeva, E., et al., *Metal-enhanced fluorescence immunoassays using total internal reflection and silver island-coated surfaces.* Anal Biochem, 2004. **334**(2): p. 303-11.
225. Lukomska, J., et al., *Fluorescence enhancements on silver colloid coated surfaces.* J Fluoresc, 2004. **14**(4): p. 417-23.
226. Zhang, J., et al., *Metal-enhanced fluoroimmunoassay on a silver film by vapor deposition.* J Phys Chem B, 2005. **109**(16): p. 7969-75.
227. Yongxia, Z., et al., *Metal-enhanced fluorescence from copper substrates.* Applied Physics Letters, 2007. **90**(17): p. 173116.
228. Xie, F., M.S. Baker, and E.M. Goldys, *Homogeneous silver-coated nanoparticle substrates for enhanced fluorescence detection.* J Phys Chem B, 2006. **110**(46): p. 23085-91.
229. Goldys, E.M., et al., *Fluorescence amplification by electrochemically deposited silver nanowires with fractal architecture.* J Am Chem Soc, 2007. **129**(40): p. 12117-22.
230. Fu, C.-C., et al., *Tunable Nanowrinkles on Shape Memory Polymer Sheets.* Advanced Materials, 2009. **21**(44): p. 4472-4476.
231. Szmacinski, H., et al., *Large Fluorescence Enhancements of Fluorophore Ensembles with Multilayer Plasmonic Substrates: Comparison of Theory and Experimental Results.* The Journal of Physical Chemistry C, 2012.
232. Bek, A., et al., *Fluorescence enhancement in hot spots of AFM-designed gold nanoparticle sandwiches.* Nano Lett, 2008. **8**(2): p. 485-90.
233. Luchowski, R., et al., *Plasmonic platforms of self-assembled silver nanostructures in application to fluorescence.* J Nanophotonics, 2010. **4**.

234. Berezin, M.Y. and S. Achilefu, *Fluorescence lifetime measurements and biological imaging.* Chem Rev, 2010. **110**(5): p. 2641-84.
235. Valverde, J.L., *Blood, plasma, and plasma proteins : a unique contribution to modern healthcare*. Pharmaceuticals policy and law,. 2006, Amsterdam ; Washington, DC: IOS Press. vi, 330 p.
236. Chen, Y., et al., *Atomic force bio-analytics of polymerization and aggregation of phycoerythrin-conjugated immunoglobulin G molecules.* Mol Immunol, 2004. **41**(12): p. 1247-52.
237. Englade-Franklin, L.E., C.K. Saner, and J.C. Garno, *Spatially selective surface platforms for binding fibrinogen prepared by particle lithography with organosilanes.* Interface Focus, 2013. **3**(3).
238. Iqbal, A., et al., *Orientation dependence in fluorescent energy transfer between Cy3 and Cy5 terminally attached to double-stranded nucleic acids.* Proc Natl Acad Sci U S A, 2008. **105**(32): p. 11176-81.
239. Hovgaard, L., S. Frøkjær, and M.v.d. Weert, *Pharmaceutical formulation development of peptides and proteins*. 2nd ed. 2013, Boca Raton, FL: CRC Press. xii, 376 p.
240. Zhang, Y., et al., *Metal-Enhanced Fluorescence from Silver−SiO2−Silver Nanoburger Structures.* Langmuir, 2010. **26**(14): p. 12371-12376.
241. Lin, S., H. Sharma, and M. Khine, *Shrink-Induced Silica Structures for Far-field Fluorescence Enhancements.* Advanced Optical Materials, 2013. **1**(8): p. 568-572.
242. Nawarathna, D., et al., *Shrink-induced sorting using integrated nanoscale magnetic traps.* Applied Physics Letters, 2013. **102**(6): p. 063504.
243. Muldrew, K.L., *Molecular diagnostics of infectious diseases.* Curr Opin Pediatr, 2009. **21**(1): p. 102-11.
244. Ma, Y.F., et al., *Single-molecule immunoassay and DNA diagnosis.* Electrophoresis, 2001. **22**(3): p. 421-426.
245. Fu, Y., et al., *Enhanced single molecule fluorescence and reduced observation volumes on nanoporous gold (NPG) films.* Chemical Communications, 2013. **49**(92): p. 10874-10876.
246. Tinnefeld, P., *Breaking the concentration barrier.* Nature Nanotechnology, 2013. **8**(7): p. 480-482.
247. Holzmeister, P., et al., *Breaking the concentration limit of optical single-molecule detection.* Chemical Society Reviews, 2014. **43**(4): p. 1014-1028.
248. Deniz, A.A., S. Mukhopadhyay, and E.A. Lemke, *Single-molecule biophysics: at the interface of biology, physics and chemistry.* Journal of the Royal Society Interface, 2008. **5**(18): p. 15-45.
249. Baba, K. and K. Nishida, *Single-Molecule Tracking in Living Cells Using Single Quantum Dot Applications.* Theranostics, 2012. **2**(7): p. 655-667.
250. Rotman, B., *Measurement of activity of single molecules of beta-D-galactosidase.* Proc Natl Acad Sci U S A, 1961. **47**: p. 1981-91.
251. Hirschfeld, T., *Optical Microscopic Observation of Single Small Molecules.* Applied Optics, 1976. **15**(12): p. 2965-2966.
252. Gratton, E., et al., *Fluctuation correlation spectroscopy in cells: Determination of molecular aggregation.* Biophotonics: Optical Science and Engineering for the 21st Century, 2005: p. 1-14.

253. Berglund, A.J. and H. Mabuchi, *Tracking-FCS: Fluorescence correlation spectroscopy of individual particles.* Optics Express, 2005. **13**(20): p. 8069-8082.
254. Mély, Y., G. Duportail, and L.A. Bagatolli, *Fluorescent methods to study biological membranes*. Springer series on fluorescence,. 2013, Heidelberg ; New York: Springer. xiii, 485 p.
255. Bonne, O.K.a.G., *Fluorescence correlation spectroscopy: the technique and its applications.* Reports on Progress in Physics
2002. **65**(251).
256. Digman, M.A. and E. Gratton, *Lessons in fluctuation correlation spectroscopy.* Annual Review of Physical Chemistry, Vol 62, 2011. **62**: p. 645-68.
257. Lakowicz, J.R., *Principles of fluorescence spectroscopy*. 3rd ed. 2006, New York: Springer. xxvi, 954 p.
258. Hof, M., R. Hutterer, and V. Fidler, *Fluorescence spectroscopy in biology : advanced methods and their applications to membranes, proteins, DNA, and cells*. Springer series on fluorescence. 2005, Berlin ; New York: Springer. xix, 305 p.
259. Berland, K.M., et al., *Scanning two-photon fluctuation correlation spectroscopy: particle counting measurements for detection of molecular aggregation.* Biophys J, 1996. **71**(1): p. 410-20.
260. Axelrod, D., *Cell-Substrate Contacts Illuminated by Total Internal-Reflection Fluorescence.* Biophysical Journal, 1981. **33**(2): p. A200-A200.
261. Ruckstuhl, T. and S. Seeger, *Attoliter detection volumes by confocal total-internal-reflection fluorescence microscopy.* Optics Letters, 2004. **29**(6): p. 569-571.
262. Hassler, K., et al., *Total internal reflection fluorescence correlation spectroscopy (TIR-FCS) with low background and high count-rate per molecule.* Opt Express, 2005. **13**(19): p. 7415-23.
263. Wenger, J. and H. Rigneault, *Photonic Methods to Enhance Fluorescence Correlation Spectroscopy and Single Molecule Fluorescence Detection.* International Journal of Molecular Sciences, 2010. **11**(1): p. 206-221.
264. Dulin, D., et al., *Studying genomic processes at the single-molecule level: introducing the tools and applications.* Nature Reviews Genetics, 2013. **14**(1): p. 9-22.
265. Levene, M.J., et al., *Zero-mode waveguides for single-molecule analysis at high concentrations.* Science, 2003. **299**(5607): p. 682-686.
266. Rigneault, H., et al., *Enhancement of single-molecule fluorescence detection in subwavelength apertures.* Physical Review Letters, 2005. **95**(11).
267. Pohl, D.W., W. Denk, and M. Lanz, *Optical Stethoscopy - Image Recording with Resolution Lambda/20.* Applied Physics Letters, 1984. **44**(7): p. 651-653.
268. Waters, J.C., *Accuracy and precision in quantitative fluorescence microscopy.* Journal of Cell Biology, 2009. **185**(7): p. 1135-1148.
269. Dorfman, A., N. Kumar, and J.I. Hahm, *Highly sensitive biomolecular fluorescence detection using nanoscale ZnO platforms.* Langmuir, 2006. **22**(11): p. 4890-4895.
270. Liu, G.L., et al., *Fluorescence enhancement of quantum dots enclosed in Au nanopockets with subwavelength aperture.* Applied Physics Letters, 2006. **89**(24).
271. Kinkhabwala, A., et al., *Large single-molecule fluorescence enhancements produced by a bowtie nanoantenna.* Nature Photonics, 2009. **3**(11): p. 654-657.

272. Zhu, P. and H.G. Craighead, *Zero-Mode Waveguides for Single-Molecule Analysis.* Annual Review of Biophysics, Vol 41, 2012. **41**: p. 269-293.
273. Bakker, R.M., et al., *Enhanced localized fluorescence in plasmonic nanoantennae.* Applied Physics Letters, 2008. **92**(4).
274. Balaa, K., E. Fort, and I. Nikon, *Surface Plasmon Enhanced TIRF Imaging.* Imaging & Microscopy, 2009. **11**(4): p. 55-56.
275. Schuck, P.J., et al., *A novel fluorophore for two-photon-excited single-molecule fluorescence.* Chemical Physics, 2005. **318**(1-2): p. 7-11.
276. Ntziachristos, V., *Going deeper than microscopy: the optical imaging frontier in biology.* Nature Methods, 2010. **7**(8): p. 603-614.
277. Trofimov, V.A. and E.B. Tereshin, *Localization of light energy of a femtosecond laser pulse upon generation of the second harmonic in a one-dimensional nonlinear photonic crystal with alternating nonlinear response.* Optics and Spectroscopy, 2008. **104**(5): p. 737-743.
278. So, P.T.C., et al., *Two-photon excitation fluorescence microscopy.* Annual Review of Biomedical Engineering, 2000. **2**: p. 399-429.
279. Takasaki, K.T., J.B. Ding, and B.L. Sabatini, *Live-Cell Superresolution Imaging by Pulsed STED Two-Photon Excitation Microscopy.* Biophysical Journal, 2013. **104**(4): p. 770-777.
280. Sivapalan, S.T., et al., *Off-Resonant Two-Photon Absorption Cross-Section Enhancement of an Organic Chromophore on Gold Nanorods.* Journal of Physical Chemistry Letters, 2013. **4**(5): p. 749-752.
281. Albota, M.A., C. Xu, and W.W. Webb, *Two-photon fluorescence excitation cross sections of biomolecular probes from 690 to 960 nm.* Applied Optics, 1998. **37**(31): p. 7352-7356.
282. Zhang, Y., et al., *Controlled aggregation and enhanced two-photon absorption of a water-soluble squaraine dye with a poly(acrylic acid) template.* Langmuir, 2013. **29**(35): p. 11005-12.
283. Vella, J.H. and A.M. Urbas, *Nanoplasmonic Array Enhancement of Two-Photon Absorption in a Dye Film.* Journal of Physical Chemistry C, 2012. **116**(32): p. 17169-17173.
284. Wenseleers, W., et al., *Five orders-of-magnitude enhancement of two-photon absorption for dyes on silver nanoparticle fractal clusters.* Journal of Physical Chemistry B, 2002. **106**(27): p. 6853-6863.
285. Kano, H. and S. Kawata, *Two-photon-excited fluorescence enhanced by a surface plasmon.* Optics Letters, 1996. **21**(22): p. 1848-1850.
286. Cohanoschi, I., et al., *Effect of the concentration of organic dyes on their surface plasmon enhanced two-photon absorption cross section using activated Au nanoparticles.* Journal of Applied Physics, 2007. **101**(8).
287. Sanchez, E.J., L. Novotny, and X.S. Xie, *Near-field fluorescence microscopy based on two-photon excitation with metal tips.* Physical Review Letters, 1999. **82**(20): p. 4014-4017.
288. Jung, J.M., et al., *Two-Photon Excited Fluorescence Enhancement for Ultrasensitive DNA Detection on Large-Area Gold Nanopatterns.* Advanced Materials, 2010. **22**(23): p. 2542-2546.

289. Cohanoschi, I. and F.E. Hernandez, *Surface plasmon enhancement of two- and three-photon absorption of Hoechst 33 258 dye in activated gold colloid solution.* J Phys Chem B, 2005. **109**(30): p. 14506-12.
290. Fischer, J., et al., *Near-Field-Mediated Enhancement of Two-Photon-Induced Fluorescence on Plasmonic Nanostructures.* The Journal of Physical Chemistry C, 2010. **114**(49): p. 20968-20973.
291. Sivapalan, S.T., et al., *Plasmonic Enhancement of the Two Photon Absorption Cross Section of an Organic Chromophore Using Polyelectrolyte-Coated Gold Nanorods.* Langmuir, 2012. **28**(24): p. 9147-9154.
292. Aouani, H., et al., *Two-photon fluorescence correlation spectroscopy with high count rates and low background using dielectric microspheres.* Biomed Opt Express, 2010. **1**(4): p. 1075-1083.
293. Kinkhabwala, A., et al., *Large single-molecule fluorescence enhancements produced by a bowtie nanoantenna.* Nat Photon, 2009. **3**(11): p. 654-657.
294. Zhang, J., et al., *Metal-enhanced single-molecule fluorescence on silver particle monomer and dimer: Coupling effect between metal particles.* Nano Letters, 2007. **7**(7): p. 2101-2107.
295. Yuan, H., et al., *Thousand-fold enhancement of single-molecule fluorescence near a single gold nanorod.* Angew Chem Int Ed Engl, 2013. **52**(4): p. 1217-21.
296. Khatua, S., et al., *Resonant Plasmonic Enhancement of Single-Molecule Fluorescence by Individual Gold Nanorods.* ACS Nano, 2014.
297. Heucke, S.F., et al., *Placing individual molecules in the center of nanoapertures.* Nano Letters, 2014. **14**(2): p. 391-5.
298. Zhao, T.T., et al., *Gold Nanorod Enhanced Two-Photon Excitation Fluorescence of Photosensitizers for Two-Photon Imaging and Photodynamic Therapy.* Acs Applied Materials & Interfaces, 2014. **6**(4): p. 2699-2707.
299. Aouani, H., et al., *Large molecular fluorescence enhancement by a nanoaperture with plasmonic corrugations.* Optics Express, 2011. **19**(14): p. 13056-13062.
300. Punj, D., et al., *Gold nanoparticles for enhanced single molecule fluorescence analysis at micromolar concentration.* Optics Express, 2013. **21**(22): p. 27338-27343.
301. Punj, D., et al., *A plasmonic 'antenna-in-box' platform for enhanced single-molecule analysis at micromolar concentrations.* Nat Nanotechnol, 2013. **8**(7): p. 512-6.
302. Zhang, Y.X., A. Dragan, and C.D. Geddes, *Broad Wavelength Range Metal-Enhanced Fluorescence Using Nickel Nanodeposits.* Journal of Physical Chemistry C, 2009. **113**(36): p. 15811-15816.
303. Williams, S.M., et al., *Accessing surface plasmons with Ni microarrays for enhanced IR absorption by monolayers.* Journal of Physical Chemistry B, 2003. **107**(43): p. 11871-11879.
304. Chen, J., et al., *Plasmonic nickel nanoantennas.* Small, 2011. **7**(16): p. 2341-7.
305. Pohl, M., et al., *Tuning of the transverse magneto-optical Kerr effect in magneto-plasmonic crystals.* New Journal of Physics, 2013. **15**.
306. Lim, J. and S.A. Majetich, *Composite magnetic-plasmonic nanoparticles for biomedicine: Manipulation and imaging.* Nano Today, 2013. **8**(1): p. 98-113.
307. Torrado, J.F., et al., *Magneto-optical effects in interacting localized and propagating surface plasmon modes.* Optics Express, 2010. **18**(15): p. 15635-15642.

308. Halpern, A.R. and R.M. Corn, *Lithographically patterned electrodeposition of gold, silver, and nickel nanoring arrays with widely tunable near-infrared plasmonic resonances.* ACS Nano, 2013. **7**(2): p. 1755-62.
309. Belotelov, V.I., et al., *Enhanced magneto-optical effects in magnetoplasmonic crystals.* Nature Nanotechnology, 2011. **6**(6): p. 370-376.
310. Regatos, D., et al., *Suitable combination of noble/ferromagnetic metal multilayers for enhanced magneto-plasmonic biosensing.* Optics Express, 2011. **19**(9): p. 8336-8346.
311. Armelles, G., et al., *Magnetoplasmonics: Combining Magnetic and Plasmonic Functionalities.* Advanced Optical Materials, 2013. **1**(1): p. 10-35.
312. Temnov, V.V., et al., *Active magneto-plasmonics in hybrid metal-ferromagnet structures.* Nature Photonics, 2010. **4**(2): p. 107-111.
313. Chin, J.Y., et al., *Nonreciprocal plasmonics enables giant enhancement of thin-film Faraday rotation.* Nature Communications, 2013. **4**.
314. Banthi, J.C., et al., *High Magneto-Optical Activity and Low Optical Losses in Metal-Dielectric Au/Co/Au-SiO2 Magnetoplasmonic Nanodisks.* Advanced Materials, 2012. **24**(10): p. Op36-Op41.
315. Sharma, H., et al., *Enhanced emission of fluorophores on shrink-induced wrinkled composite structures.* Optical Materials Express, 2014. **4**(4): p. 753-763.
316. Zhang, B. and T. Cui, *Tunable Shrink Induced Graphene Composites for Chemical Sensors and Microfluidics.* 2012 Ieee 25th International Conference on Micro Electro Mechanical Systems (Mems), 2012.
317. Zhang, W.H., et al., *Giant and uniform fluorescence enhancement over large areas using plasmonic nanodots in 3D resonant cavity nanoantenna by nanoimprinting.* Nanotechnology, 2012. **23**(22).
318. Stringari, C., et al., *Phasor approach to fluorescence lifetime microscopy distinguishes different metabolic states of germ cells in a live tissue.* Proceedings of the National Academy of Sciences of the United States of America, 2011. **108**(33): p. 13582-13587.
319. Lakowicz, J.R., et al., *Ultrabright fluorescein-labeled antibodies near silver metallic surfaces.* Biopolymers, 2004. **74**(6): p. 467-75.
320. Tregidgo, C., J.A. Levitt, and K. Suhling, *Effect of refractive index on the fluorescence lifetime of green fluorescent protein.* Journal of Biomedical Optics, 2008. **13**(3).
321. Sabanayagam, C.R. and J.R. Lakowicz, *Increasing the sensitivity of DNA microarrays by metal-enhanced fluorescence using surface-bound silver nanoparticles.* Nucleic Acids Res, 2007. **35**(2): p. e13.
322. Malicka, J., I. Gryczynski, and J.R. Lakowicz, *DNA hybridization assays using metal-enhanced fluorescence.* Biochemical and Biophysical Research Communications, 2003. **306**(1): p. 213-218.
323. Dragan, A.I., et al., *Two-color, 30 second microwave-accelerated Metal-Enhanced Fluorescence DNA assays: A new Rapid Catch and Signal (RCS) technology.* Journal of Immunological Methods, 2011. **366**(1-2): p. 1-7.
324. Qiang, W.B., H. Li, and D.K. Xu, *Metal enhanced fluorescent biosensing assays for DNA through the coupling of silver nanoparticles.* Analytical Methods, 2013. **5**(3): p. 629-635.
325. Lim, T.S., et al., *Fluorescence enhancement and lifetime modification of single nanodiamonds near a nanocrystalline silver surface.* Physical Chemistry Chemical Physics, 2009. **11**(10): p. 1508-1514.

326. Le Moal, E., et al., *Nanoroughened plasmonic films for enhanced biosensing detection.* Nanotechnology, 2009. **20**(22): p. 225502.
327. Sokolov, I. and S. Naik, *Novel fluorescent silica nanoparticles: towards ultrabright silica nanoparticles.* Small, 2008. **4**(7): p. 934-9.
328. Ganesh, N., et al., *Enhanced fluorescence emission from quantum dots on a photonic crystal surface.* Nature Nanotechnology, 2007. **2**(8): p. 515-520.
329. Kairdolf, B.A., et al., *Semiconductor Quantum Dots for Bioimaging and Biodiagnostic Applications.* Annual Review of Analytical Chemistry, Vol 6, 2013. **6**: p. 143-162.
330. Bras, M., et al., *Optimisation of a silicon/silicon dioxide substrate for a fluorescence DNA microarray.* Biosensors & Bioelectronics, 2004. **20**(4): p. 797-806.
331. Oillic, C., et al., *Silicon nanostructures for DNA biochip applications.* Materials Science & Engineering C-Biomimetic and Supramolecular Systems, 2007. **27**(5-8): p. 1500-1503.
332. Yalcin, A., et al. *Fluorescence enhancement on reflecting substrates for microarray applications*. in *LEOS Annual Meeting Conference Proceedings, 2009. LEOS '09. IEEE*. 2009.
333. Marino, V., C. Galati, and C. Arnone, *Optimization of fluorescence enhancement for silicon-based microarrays.* Journal of Biomedical Optics, 2008. **13**(5).
334. Cretich, M., et al., *Allergen microarrays on high-sensitivity silicon slides.* Anal Bioanal Chem, 2010. **398**(4): p. 1723-33.
335. Redkar, R.J., et al., *Signal and sensitivity enhancement through optical interference coating for DNA and protein microarray applications.* Journal of biomolecular techniques : JBT, 2006. **17**(2): p. 122-130.
336. Cretich, M., et al., *High Sensitivity Protein Assays on Microarray Silicon Slides.* Analytical Chemistry, 2009. **81**(13): p. 5197-5203.
337. Terracciano, M., et al., *Optical characterization of aminosilane-modified silicon dioxide surface for biosensing*. 2013. Vol. 8. 2013.
338. Tarn, D., et al., *Mesoporous silica nanoparticle nanocarriers: biofunctionality and biocompatibility.* Acc Chem Res, 2013. **46**(3): p. 792-801.
339. Graf, C., et al., *Dye-labeled poly(organosiloxane) microgels with core-shell architecture.* Langmuir, 1999. **15**(19): p. 6170-6180.
340. Gilliland, J.W., K. Yokoyama, and W.T. Yip, *Solvent effect on mobility and photostability of organic dyes embedded inside silica sol-gel thin films.* Chemistry of Materials, 2005. **17**(26): p. 6702-6712.
341. Casalboni, M., et al., *Rigid-cage effects on the optical properties of the dye 3,3'-diethyloxadicarbocyanine incorporated in silica-gel glasses.* Applied Physics Letters, 1997. **70**(22): p. 2969-2971.
342. Herz, E., et al., *Dye structure-optical property correlations in near-infrared fluorescent core-shell silica nanoparticles.* Journal of Materials Chemistry, 2009. **19**(35): p. 6341-6347.
343. Pedone, A., et al., *Realistic Modeling of Fluorescent Dye-Doped Silica Nanoparticles: A Step Toward the Understanding of their Enhanced Photophysical Properties.* Chemistry of Materials, 2011. **23**(22): p. 5016-5023.
344. Chen, G.W., et al., *Bright and stable Cy3-encapsulated fluorescent silica nanoparticles with a large Stokes shift.* Dyes and Pigments, 2012. **93**(1-3): p. 1532-1537.

345. Miletto, I., et al., *Highly bright and photostable cyanine dye-doped silica nanoparticles for optical imaging: Photophysical characterization and cell tests.* Dyes and Pigments, 2010. **84**(1): p. 121-127.
346. Schulz, A. and C. McDonagh, *Intracellular sensing and cell diagnostics using fluorescent silica nanoparticles.* Soft Matter, 2012. **8**(9): p. 2579-2585.
347. Liang, S., et al., *Effects of a nanoscale silica matrix on the fluorescence quantum yield of encapsulated dye molecules.* Nanoscale, 2013. **5**(19): p. 9365-73.
348. Titos-Padilla, S., et al., *Photophysical properties of [Ir(tpy)(2)](3+)-doped silica nanoparticles and synthesis of a colour-tunable material based on an Ir(core)-Eu(shell) derivative.* Journal of Materials Chemistry C, 2013. **1**(24): p. 3808-3815.
349. Auger, A., et al., *A comparative study of non-covalent encapsulation methods for organic dyes into silica nanoparticles.* Nanoscale Research Letters, 2011. **6**.
350. Hai, X.D., et al., *Preparation and a time-resolved fluoroimmunoassay application of new europium fluorescent nanoparticles.* Analytical Sciences, 2004. **20**(2): p. 245-246.
351. Larson, D.R., et al., *Silica nanoparticle architecture determines radiative properties of encapsulated fluorophores.* Chemistry of Materials, 2008. **20**(8): p. 2677-2684.
352. Murthy, B.R., et al., *Silicon nanopillar substrates for enhancing signal intensity in DNA microarrays.* Biosensors & Bioelectronics, 2008. **24**(4): p. 723-728.
353. Tsougeni, K., et al., *High-capacity and high-intensity DNA microarray spots using oxygen-plasma nanotextured polystyrene slides.* Analytical and Bioanalytical Chemistry, 2012. **403**(9): p. 2757-2764.
354. Asanov, A., A. Zepeda, and L. Vaca, *A platform for combined DNA and protein microarrays based on total internal reflection fluorescence.* Sensors (Basel), 2012. **12**(2): p. 1800-15.
355. Rhee, J.K., et al., *Integrated analysis of genome-wide DNA methylation and gene expression profiles in molecular subtypes of breast cancer.* Nucleic Acids Res, 2013. **41**(18): p. 8464-74.
356. Ménard, R., *Malaria : methods and protocols*. 2nd ed. Methods in molecular biology,. 2013, New York London: Humana Press ; Springer distributor. xv, 626 p.
357. Parish, T. and A.C. Brown, *Mycobacteria protocols*. 2nd ed. Methods in molecular biology. 2008, New York, NY: Humana Press. xix, 456 p.
358. Ma, L., et al., *Microarray-based fluorescence assay of endonuclease functionality and inhibition.* Analyst, 2013. **138**(4): p. 1048-1052.
359. Park, H.G., et al., *Fluorescence-based assay formats and signal amplification strategies for DNA microarray analysis.* Chemical Engineering Science, 2006. **61**(3): p. 954-965.
360. Li, X., et al., *Aluminum oxide nanostructure-based substrates for fluorescence enhancement.* Optics Express, 2012. **20**(19): p. 21272-7.
361. DeLouise, L.A., P.M. Kou, and B.L. Miller, *Cross-Correlation of Optical Microcavity Biosensor Response with Immobilized Enzyme Activity. Insights into Biosensor Sensitivity.* Analytical Chemistry, 2005. **77**(10): p. 3222-3230.
362. Oillic, C., et al., *DNA microarrays on silicon nanostructures: Optimization of the multilayer stack for fluorescence detection.* Biosensors & Bioelectronics, 2007. **22**(9-10): p. 2086-2092.
363. Le Berre, V., et al., *Dendrimeric coating of glass slides for sensitive DNA microarrays analysis.* Nucleic Acids Res, 2003. **31**(16): p. e88.

364. Schlapak, R., et al., *Glass surfaces grafted with high-density poly(ethylene glycol) as substrates for DNA oligonucleotide microarrays.* Langmuir, 2006. **22**(1): p. 277-85.
365. Kim, J.S., et al., *Size-controllable quartz nanostructure for signal enhancement of DNA chip.* Biosensors and Bioelectronics, 2011. **26**(5): p. 2085-2089.
366. Wong, I.Y. and N.A. Melosh, *An electrostatic model for DNA surface hybridization.* Biophys J, 2010. **98**(12): p. 2954-63.
367. Lai, S.L., C.H. Chen, and K.L. Yang, *Enhancing the Fluorescence Intensity of DNA Microarrays by Using Cationic Surfactants.* Langmuir, 2011. **27**(9): p. 5659-5664.
368. *Nomenclature, Symbols, Units and Their Usage in Spectrochemical Analysis .3. Analytical Flame Spectroscopy and Associated Non-Flame Procedures.* Spectrochimica Acta Part B-Atomic Spectroscopy, 1978. **33**(6): p. 248-269.
369. He, Z.L. and J.Z. Zhou, *Empirical evaluation of a new method for calculating signal-to-noise ratio for microarray data analysis.* Applied and Environmental Microbiology, 2008. **74**(10): p. 2957-2966.
370. Lee, J.S., et al., *Assessing the Detection Capacity of Microarrays as Bio/Nanosensing Platforms.* BioMed Research International, 2013. **2013**: p. 8.
371. Chen, Y., et al., *Fabrication of DNA microarrays with poly(L-glutamic acid) monolayers on gold substrates for SPR imaging measurements.* Langmuir, 2009. **25**(9): p. 5054-60.
